TURBULENT HEAT TRANSFER ASSOCIATED WITH COHERENT STRUCTURES IN A WALL TURBULENT SHEAR FLOW

1988

MASATO TAGAWA

TURBULENT HEAT TRANSFER ASSOCIATED WITH COHERENT STRUCTURES IN A WALL TURBULENT SHEAR FLOW

By

Masato Tagawa

B.S., Nagoya Institute of Technology, 1981

M.S., Nagoya Institute of Technology, 1983

DOCTORAL DISSERTATION

Submitted to

Nagoya Institute of Technology

in partial fulfillment of

the requirements for the degree of

Doctor of Philosophy

in

Engineering

April 1988

ACKNOWLEDGMENTS

I would like to express my sincere gratitude to Professor Y. Nagano, my advisor, who provided me many helpful suggestions, fruitful discussions and encouragement in the course of preparation of the dissertation.

I am deeply grateful to Professors S. Yamaguchi, I. Yamada and K. Nakabayashi for careful reading and appropriate suggestions for this thesis.

I am also grateful for the useful discussions and advice I received from Dr. M. Hishida (the professor emeritus of Nagoya Institute of Technology). The faculty of the Mechanical Engineering Department (Nagoya Institute of Technology) are to be acknowledged for providing an atmosphere conducive to research, including a situation which facilitated frequent exchanges of ideas with colleagues, particularly graduate students and Professor T. Tsuji.

Mr. S. Iwai has helped me in preparing the typescript and figures. I would like to acknowledge his great help.

This research was partially supported by a Grant-in-Aid for Scientific Research from the Ministry of Education, Science and Culture of Japan (No. 60550153 and No. 61550156).

ABSTRACT

Various types of moments of velocity and temperature fluctuations of the first to the fourth order have been measured and analyzed in a wall-bounded shear flow. First, an orthogonal series expansion for the three-dimensional joint probability density function (pdf) is developed using the cumulants and Hermite polynomials. This pdf is found to provide satisfactory predictions for the statistical characteristics, including triple products, of turbulent momentum and heat transfer.

Next, to identify the role of coherent motions in the turbulent heat transport processes, an objective method for the recognition and description of coherent structures has been developed. Four distinct patterns are recognized in the sequence of coherent motions near the wall. These four basic flow patterns have their own characteristic vortex structures and reflect the succession of stages that might occur in the evolution of coherent motions. Also, these recognized patterns can delineate the mechanistic picture of turbulent heat transport in the wall region. Among other things, the important finding is that the outflowing low-momentum wall-region fluid organizing strong vortical motions with the incoming higher-momentum fluid from regions away from the wall is the principal contributor to the turbulent exchange process of heat.

Finally, the conditional sampling and averaging technique is employed to investigate the statistical characteristics of coherent turbulent transport processes of momentum and heat. Conditional pdfs are developed for various moments of velocity and temperature up to the third order. It is shown that the present pdfs can represent the detailed role of coherent

motions in the dynamics of wall turbulent shear flows and in the relevant process of heat transport by turbulence. In particular, the importance of coherent motions in the turbulent diffusion process of Reynolds stress components and heat fluxes is demonstrated for the first time by the present study.

TABLE OF CONTENTS

Page

LIST OF FIGURES

LIST OF TABLES

NOMENCLATURE

c_p	Specific heat at constant pressure.
C_{pqr}	Coefficient in the power-series expansion for ψ (Eq.(3-10)).
C_{R1}, C_{R2}, a_1, a_2, a_3, a_4, cs_1, cs_2, cs_3	Model constants for triple products.
D_{pqr}	Coefficient in the power-series expansion for ψ (Eq.(3-11)).
$F(\chi)$	Flatness factor of χ : $F(\chi)= \overline{\hat{\chi}^4}$.
H	Threshold.
$H_n(x)$	One-dimensional Hermite polynomial (Eq.(3-13)).
$\vec{i}$, $\vec{j}$	Unit vectors (streamwise and normal to the wall).
$I_i(\tau, H)$	Detection function (Eq.(5-2)).
K	Sum of the orders of ξ, η and ζ : K= p+q+r.
k	Turbulence kinetic energy: $k= \overline{u_i u_i}/2$.
k_{pqr}	Cumulant (Eq.(3-5)).
m_{pqr}	Moment (Eq.(3-2)).
P	Three-dimensional joint pdf (Eq.(3-12)).
P_i	Conditional pdf in the ith-quadrant of the (u, v)-plane.
p, q, r	Orders of ξ, η and ζ in the power-series expansion for ψ.
P_{II}, P_{III}	Pdfs of second- and third-order moments.
Pr	Prandtl number.
Q	Turbulence quantity.
$\vec{q}'$	Turbulent heat-flux vector (Eq.(5-8)).
q_w	Wall heat flux.
r, r_o	Coordinate in radial direction, and pipe radius.
R_{uv}, R_{ut}, R_{vt}	Cross-correlation coefficients between u and v, u and t, and v and t.
$S(\chi)$	Skewness factor of χ : $S(\chi)= \overline{\hat{\chi}^3}$.
$\overline{T}$	Time averaged temperature.
T	Averaging time (Eq.(5-1)).
$\overline{T}_i$, $\overline{\Delta T_i}$	Mean period, and mean duration of the ith-quadrant motion.
$\overline{T}_c$	Centerline temperature.
$\overline{T}_w$	Wall temperature: $\overline{T}_w$= 100 ℃.
$\overline{T}^+$	Dimensionless temperature: $\overline{T}^+= (\overline{T}_w - \overline{T})/t_\tau$.
t	Fluctuating temperature.
t_τ	Friction temperature: $t_\tau= q_w/\rho c_p u_\tau$.
$\overline{U}$	Time averaged streamwise velocity.
$\overline{U}_c$	Centerline velocity.
U_v	Convection velocity of an observer.
$\overline{U}^+$	Dimensionless velocity: $\overline{U}^+= \overline{U}/u_\tau$.
u, v, w	Streamwise, normal to the wall and circumferential velocity fluctuations.
u_τ	Friction velocity: $u_\tau= \sqrt{\tau_w/\rho}$.

$\tilde{u}_i$	Velocity vector relative to an observer moving at U_v (Eq.(5-6)).
u_i'	Velocity vector for coherent motions (Eq.(5-7)).
W_x	Weighted function for moment x.
x	Moment, or streamwise coordinate.
x^+	Dimensionless streamwise coordinate: $x^+ = u_\tau x / \nu$.
y	Coordinate normal to the wall: $y = r_o - r$.
y^+	Dimensionless distance from the wall: $y^+ = u_\tau y / \nu$.

Abbreviation

pdf	Probability density function.

Greek Letters

γ_+, γ_-	Fraction of time during which a random variable χ is positive (γ_+) or negative (γ_-).
δ^*	Displacement thickness.
ε , ε_t	Dissipation rates of k and $\overline{t^2}/2$.
θ	Momentum thickness.
ν	Kinematic viscosity.
ξ , η , ζ	Parameters of ψ .
ρ	Density.
$\sigma_{u,i}$, $\sigma_{v,i}$	Sign functions defined in the (u, v)-plane (Eq.(6-2)).
τ , τ'	Time.
τ_w	Wall shear stress.
χ	Random variable.
ψ	Characteristic function of the joint pdf P (Eq.(3-1)).

Special Symbols

$\overline{(\ )}$	Expected value or time average.
$(\hat{\ })$	Normalization by the respective r.m.s. value.
$(\ )'$	Normalization of velocity and temperature by u_τ and t_τ, or localized fluctuating part of a turbulence quantity about a moving-average (Eq.(5-1)).
$\overline{(\ )}_i$	Conditional average in the ith-quadrant of the (u, v)-plane.
$\langle\ \rangle$	Ensemble average (Eq.(5-3)).
$(\dot{\ })$	Differentiation by time.
$\|\ \|$	Absolute value.

Subscripts

i, j, k	Tensor notation.
G	Gaussian.

CHAPTER I

INTRODUCTION

1.1. Background

Transfer problems of momentum and heat have begun to be analyzed with a strategy of recent advanced turbulence modelling such as those based on Reynolds stress and heat flux closures (e.g., Elghobashi & Launder 1981). Results, however, are not as satisfactory as initially expected, mainly due to a few unreasonable hypotheses involved in modelling (Lumley 1978). In order to resolve pertinent problems radically, we need a correct knowledge of the statistical characteristics of the first- and second-order moments of velocity and temperature fluctuations, and the relevant processes of turbulent diffusions (i.e., third-order moments), all of which are basic parameters in the stress and heat flux equations modelling.

Antonia & Atkinson (1973) first investigated statistical characteristics of Reynolds shear stress without the aid of the assumption of Gaussian behaviour. Their approaches, however, cannot be applied to the analysis of turbulent heat transfer and third-order moments of velocity and temperature, since the derived pdf is only valid for second-order moments in a velocity field without passive contaminants. Furthermore, in the analysis of third-order moments, we cannot generally use the conventional assumption of Gaussian behaviour because of the essential unreality according to which a mean value is consistently zero.

On the other hand, it is now widely recognized that many of the attributes of wall-turbulent shear flows can be ascribed to well-ordered

fluid motions, i.e., coherent structures, near the wall (Kline et al. 1967; Corino & Brodkey 1969). So far, various flow-visualization studies have provided useful qualitative knowledge of these organized structures (e.g., Kim, Kline & Reynolds 1971; Grass 1971; Nychas, Hershey & Brodkey 1973; Offen & Kline 1974, 1975; Praturi & Brodkey 1978; Head & Bandyopadhyay 1981; Falco 1982). However, quantitative treatment of information obtained by flow-visualization techniques is not so easy. Thus, accumulation of relevant quantitative knowledge is now required. In principle, it is possible to investigate the characteristics of coherent structures quantitatively by a hot-wire anemometry technique. In this technique, the sampling criterion is the key to accurate extraction of coherent structures from seemingly chaotic hot-wire traces. Many detection methods for coherent structures have been proposed and evaluated. The most familiar detection methods are as follows:

(1) uv-quadrant method (Lu & Willmarth 1973; Brodkey, Wallace & Eckelmann 1974; Sabot & Comte-Bellot 1976; Nakagawa & Nezu 1981).
(2) VITA sampling technique (Blackwelder & Kaplan 1976).
(3) VITA with slope (Chen & Blackwelder 1978; Johansson & Alfredsson 1982).
(4) Pattern-recognition technique (Wallace, Brodkey & Eckelmann 1977).
(5) Band-pass filter technique (Rao, Narasimha & Narayanan 1971; Ueda & Hinze 1975).
(6) Short-time averaged autocorrelation technique (Kim, Kline & Reynolds 1971; Strickland & Simpson 1975; Hishida & Nagano 1979).
(7) u-level (Lu & Willmarth 1973) and modified u-level techniques (Luchik & Tiederman 1987).

These methods have their own features in treatable physical quantities

(e.g., bursting period, duration of bursts, etc.), detection algorithms, and information-sources necessary for detection (e.g., streamwise velocity, normal velocity, temperature, wall shear stress, etc.). Although we cannot generally rank these detection methods, the uv-quadrant method and the VITA sampling technique are often used because of accurate depiction of the essential characteristics of coherent structures and the practical ease of the detection algorithms. Recently, careful appraisal of the effectiveness of these two methods has been performed. Alfredsson & Johansson (1984) pointed out that the phenomena detected by the VITA technique corresponded principally with ejection-type motions identified by the uv-quadrant method, while the ensemble-averaged waveforms obtained by the VITA technique depicted a more realistic change in streamwise fluid velocity. On the other hand, employing flow-visualization and hot-wire anemometer techniques simultaneously, Bogard & Tiederman (1986) evaluated the detection algorithms from the standpoint of capability of detecting ejection-type motions recognized by flow visualization, and concluded that the uv-quadrant method had the greatest reliability with a high probability of detecting the ejections and a low probability of false detections. However, all of these methods possess inherent ambiguity in setting a threshold level. In reality, it is no easy matter to establish a rational basis for determination of the threshold level. Accordingly, further modifications and improvements of the existing detection methods or the development of new ones are still needed.

In general, turbulent heat transfer is dominated essentially by the flow near a heat-transfer surface. Therefore, the basic mechanism of heat transfer is expected to be strongly associated with the coherent turbulent

motions near the wall. The mechanistic picture of turbulent heat transfer, however, is not yet made sufficiently clear, even for the most fundamental flows such as those in a pipe or a boundary layer. So much is still unknown about the relationship between the coherent structures near the wall and heat transport processes. Research pertaining to this problem is now accumulating experimental evidences.

Antonia et al. (1982) and Subramanian et al. (1982) directed their attention to large-scale temperature fronts noted by Chen & Blackwelder (1978), and investigated the relationship between the coherent structures and heat transport processes in a boundary layer. In their experiment, eleven cold-wires were arrayed normal to the wall like a "rake," and the temperature front was detected by the visual observation of temperature-fluctuation signals. The main purposes of their studies were to examine the Reynolds-number dependence of the structure characterized by the temperature front and to investigate the diversity of conditionally averaged patterns of coherent motions obtained by various existing detection-methods with reference to those decided with the "rake" method. However, flow structures and associated turbulent heat transfer in the wall region were not studied in detail. Recently, Iritani et al. (1985) turned their attention to low-speed streaks in the viscous sublayer and investigated unsteady wall-temperature fluctuations by using a temperature-sensitive liquid crystal. A close correlation was found between turbulent heat transfer and counter-rotating streamwise vortices recognized as one of the fundamental elements of the coherent structures (Bakewell & Lumley 1967; Lee, Eckelman & Hanratty 1974; Blackwelder & Eckelmann 1979; Kim 1985).

Perry & Hoffmann (1976) examined the similarity between the Reynolds shear stress uv and turbulent heat flux vt from the results of a conditional analysis for a heated flat-plate boundary layer flow. In their experimental study with the help of the quadrant analysis, however, the Reynolds shear stress uv was analyzed in the (u, v)-plane and the turbulent heat flux vt in the (v, t)-plane. Hence, the correspondence between heat transport and fluid motions was not strictly specified.

In the series of investigations on turbulent heat transfer at Nagoya Institute of Technology, two unique measurement techniques have been developed: one for simultaneous measurements of velocity and temperature in nonisothermal flows (Hishida & Nagano 1978a), and the other for turbulence measurements near the wall with specially devised, symmetrically bent 'V'-shaped hot wires (Hishida & Nagano 1988a, b). Employing these techniques, the relation between turbulent heat and momentum transfer in the immediate neighborhood of the wall has been investigated from various points of view (Hishida & Nagano 1979, Nagano & Hishida 1985). However, one cannot yet give full explanation to the problems of how or how strongly these organized fluid motions dominate the statistical characteristics of scalar turbulence, e.g., temperature-fluctuation variance, turbulent heat fluxes and triple correlations between velocity and temperature.

1.2. Objectives

In view of the present state of the art described in the previous section, this study has the following five main objectives:

(1) To develop a theory by which the principal statistical aspects of high-order moments related to turbulent momentum and heat transfer can be predicted;

(2) To obtain detailed experimental evidence of these moments in a wall turbulent shear flow;

(3) To extract fundamental flow patterns (i.e., organized motions) responsible for heat and momentum transfer in the wall region;

(4) To investigate the mechanism of transmission and destruction of heat in connection with identified well-ordered motions;

(5) To identify the role of coherent structures in transport phenomena from statistical viewpoints.

1.3. Organization of the Presentation

The details of the theory, experimental program and procedures, results and conclusions are described in the remainder of this thesis.

Chapter II contains the experimental arrangement, the measuring techniques, and the methods of data acquisition and reduction.

Chapter III presents the basic theory of the statistics of turbulent heat transfer. In the theory, the cumulant-discard method (Monin & Yaglom 1971) has been used so as to take into account a departure from Gaussian behaviour (Kampé de Fériet 1966; Frenkiel & Klebanoff 1967). Then, multi-dimensional joint pdfs for quantities controlling transport phenomena have been developed (Nagano & Tagawa 1987a; Nagano, Tagawa & Tokoro 1988). The present theory covers completely the reported two-dimensional probability theory (Antonia & Atkinson 1973; Nakagawa & Nezu 1977).

In Chapter IV, the theory has been applied to the analysis of the statistical characteristics, including triple products, of turbulent heat and momentum transfer (Nagano & Tagawa 1987a; Nagano, Tagawa & Tokoro 1988). In the present study, employing the two unique techniques for simultaneous measurements of velocity and temperature and measurements of turbulence near the wall with V-shaped hot wires, turbulence quantities in the immediate neighborhood of the wall have been measured. The global analogy between heat and momentum transfer (Hishida, Nagano & Tagawa 1986) has been discussed in this chapter. Validity of the present theory has also been verified in this chapter by application to the prediction of

experimental results of pdf distributions of high-order moments. Particular attention is directed to the study of statistical characteristics of third-order moments, because measurements of their pdf distributions are few and the current modelling is quite ad hoc.

Chapter V deals with the coherent structures near the wall and their role in the heat transport process. With a new idea for the recognition and description of coherent structures, an effective sampling technique for well-ordered motions has been developed. This chapter reveals that the outflowing low-momentum wall-region fluid organizing strong vortical motions with the incoming higher-momentum fluid from regions away from the wall is the principal contributor to the turbulent exchange process of heat (Hishida, Nagano, Tagawa & Miyakawa 1984; Nagano, Hishida & Tagawa 1987; Nagano & Tagawa 1987b).

Furthermore, the foregoing information of turbulent heat and momentum transfer has been reflected in the statistical investigation (Nagano & Tagawa 1988; Tagawa & Nagano 1988). Namely in Chapter VI, theoretical treatment for the three-dimensional joint pdf has been expanded by combining a conditional sampling technique and investigated the internal structures of velocity and temperature fluctuations, Reynolds shear stress, turbulent heat fluxes, and turbulent diffusion, i.e., the triple products of velocity and temperature. The organized motions and their contributions to transport process in wall turbulence have been discussed in concrete terms.

The important conclusions drawn from this study are presented in Chapter VII.

CHAPTER II

EXPERIMENTAL FACILITIES AND DATA ACQUISITION

The experimental apparatus used for the present study is shown in Fig. 2.1. The experiment was performed in an air flow in a 45.68 mm ID reamed brass tube heated by saturated steam of atmospheric pressure to a uniform wall temperature of 100 ℃ at a Reynolds number (based on bulk velocity and pipe diameter) of 40,000. Measurements were performed at a location 167 diameters downstream from the pipe inlet and 40 diameters downstream from the beginning of the heated section. Both velocity and thermal fields were fully developed at this measurement location (Hishida & Nagano 1978b, 1979). The mean characteristics of the flow are given in Table 4.1, where $R_\theta = \overline{U}_c \theta / \nu$ ($\overline{U}_c$ being the centerline velocity) is the momentum thickness Reynolds number, $\overline{T}_w$ and $\overline{T}_c$ are the wall and centerline temperatures, q_w is the wall heat flux, and u_τ and t_τ are the friction velocity and temperature. Displacement and momentum thicknesses were 2.23 mm and 1.22 mm, respectively.

Fluctuations of velocity components (u axial, and v normal) and temperature (t) were simultaneously measured with the specially devised three-wire probe shown in Fig. 2.2(a). As seen in this figure, a conventional straight tungsten wire (l_w= 0.8 mm, d_w= 5μm) was symmetrically bent into a V-shape and combined with a normal hot-wire (l_w= 0.6 mm, d_w= 3μm), together with a cold wire (l_w= 0.9 mm, d_w= 3μm) located upstream of the hot-wires. The V-shaped hot-wire has proven highly effective for the measurement of turbulence very near the wall, where a conventional X-wire anemometry technique is either subject to large errors or, at worst, cannot

be used (Nagano & Hishida 1985; Hishida & Nagano 1988a, b). Note that the probe was constructed as small as practicable in order to assure spatial resolution without causing any thermal and aerodynamic interference between each wire, i.e., the sensing part was kept less than $6\eta_k$ (where η_k is the Kolmogorov microscale). Heat loss due to end-conduction occurs for a shorter cold-wire, which lowers the sensitivity to temperature fluctuations, and so some corrections are needed as pointed out by Paranthoen et al. (1982). In measurement of isothermal flow, a probe with two V-shaped hot-wires in an X arrangement was used as shown in Fig. 2.2(b). The circumferential velocity fluctuation (w) was measured by rotating a single normal hot-wire (Fujita & Kovasznay 1968).

All data were recorded in analog form with an FM data recorder (TEAC R-210B) and then reproduced for conversion to digital form. The digitized data were stored on magnetic tape with a 12-bit analog-to-digital converter (TEAC DR-2000). The real time sampling frequency was 32 kHz and the number of data was 52,428 per measurement. It was confirmed that the sampling frequency and the data length were quite adequate to obtain statistical values. Any slight phase lag in high-frequency temperature fluctuations that occurred in a filter circuit was eliminated almost completely by the following method: first, the Fourier transform was performed on signals of temperature fluctuation; secondly, phase discrepancy determined by a transfer function of the circuit was corrected to each Fourier coefficient; finally, the inverse Fourier transform was performed to obtain true temperature fluctuations. Conditional sampling and averaging were made for these digital data on a FACOM M-382 computer system.

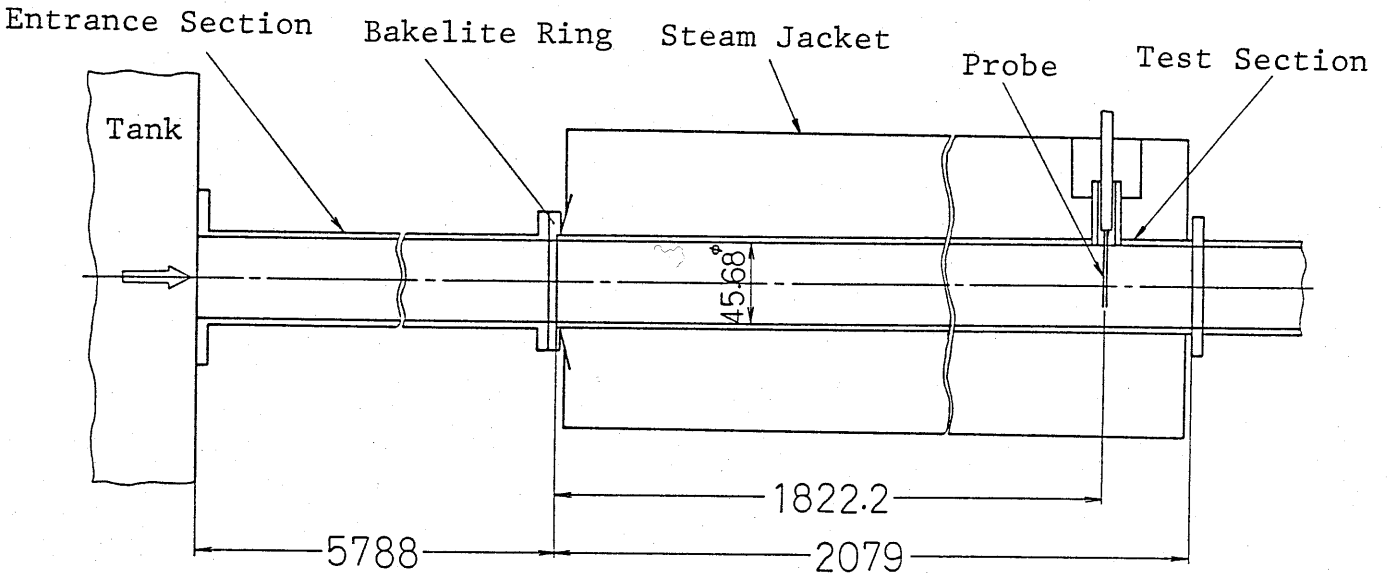

Fig. 2.1. Schematic of apparatus.

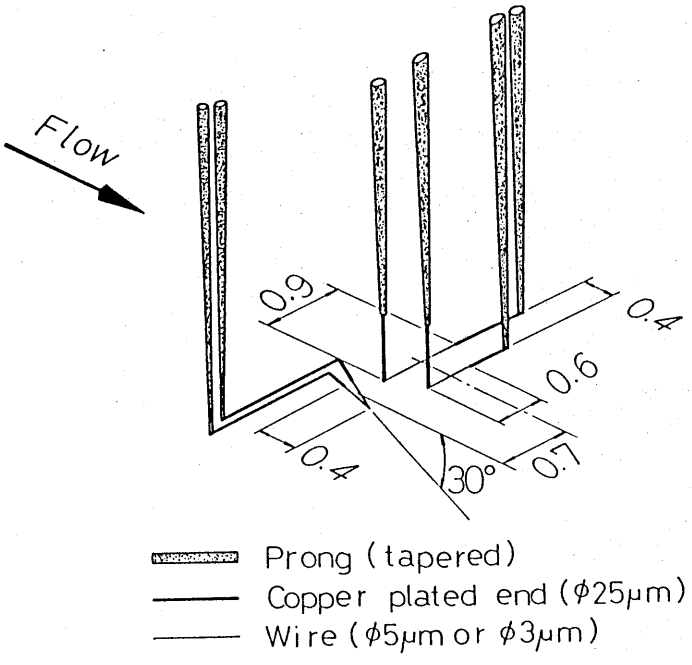

(a)

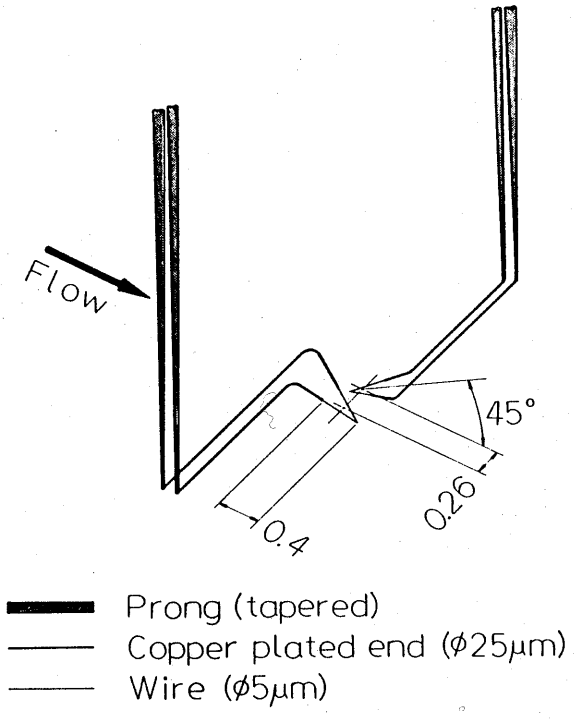

(b)

Fig. 2.2. Probe configuration (all dimensions in millimeters).
(a) Three wire probe for measurement of nonisothermal flows;
(b) X-wire probe consisting of two V-shaped hot-wires for measurement of isothermal flows.

CHAPTER Ⅲ

BASIC THEORY OF THE STATISTICS OF TURBULENT HEAT TRANSFER

To analyze generally the statistics of momentum and heat transfer, we should introduce the four-dimensional joint pdf with three components of a velocity vector $\mathbb{V}(u,v,w)$ and a fluctuating temperature t as random variables. In two-dimensional turbulent flows, however, the random properties pertaining to transport processes can be sufficiently specified by the three-dimensional joint pdf P(u,v,t). When a Gaussian distribution is supposed to be P(u,v,t), mean values of any third-order moments are consistently zero, which is usually not the case in an actual phenomenon. Thus, as given below, a more general representation for $P(\hat{u},\hat{v},\hat{t})$ is developed using their characteristic function ψ, which is the Fourier transform of the pdf. In what follows, a symbol " ^ " denotes the normalization by the respective r.m.s. value, and an overbar "— " represents an expected value or time average.

$$\psi(\xi,\eta,\zeta) = \int\int\int_{-\infty}^{\infty} P(\hat{u},\hat{v},\hat{t}) \exp\{i(\hat{u}\xi + \hat{v}\eta + \hat{t}\zeta)\}\, d\hat{u}\, d\hat{v}\, d\hat{t} \qquad (3\text{-}1)$$

If some form is given to the characteristic function ψ defined by Eq.(3-1), $P(\hat{u},\hat{v},\hat{t})$ can be obtained by executing the inverse Fourier transform of ψ. Two expressions for ψ are conceivable.

[A] Description of ψ in terms of moment m_{pqr}.

The following relation holds between m_{pqr} and ψ :

$$\left.\frac{\partial^K \psi(\xi,\eta,\zeta)}{\partial \xi^p \partial \eta^q \partial \zeta^r}\right|_{\xi=\eta=\zeta=0} = i^K m_{pqr} \tag{3-2}$$

where

K=p+q+r and

$$m_{pqr} = \overline{\hat{u}^p \hat{v}^q \hat{t}^r}$$
$$= \int\int\int_{-\infty}^{\infty} \hat{u}^p \hat{v}^q \hat{t}^r \, P(\hat{u},\hat{v},\hat{t}) \, d\hat{u} \, d\hat{v} \, d\hat{t} \tag{3-3}$$

Thus, we obtain the following expression for ψ :

$$\psi(\xi,\eta,\zeta) = \sum_{p,q,r=0}^{\infty} \frac{i^K}{p!\,q!\,r!} m_{pqr} \xi^p \eta^q \zeta^r \tag{3-4}$$

[B] Description of ψ in terms of cumulant k_{pqr}.

The definition of cumulant k_{pqr} is:

$$\left.\frac{\partial^K \ln \psi(\xi,\eta,\zeta)}{\partial \xi^p \partial \eta^q \partial \zeta^r}\right|_{\xi=\eta=\zeta=0} = i^K k_{pqr} \tag{3-5}$$

Thus,

$$\psi(\xi,\eta,\zeta) = \exp\left(\sum_{p,q,r=0}^{\infty} \frac{i^K}{p!\,q!\,r!} k_{pqr} \xi^p \eta^q \zeta^r \right) \tag{3-6}$$

The relations between m_{pqr} and k_{pqr} are:

for K=0,

$m_{000} = 1,\ k_{000} = 0$;

for $1 \leqq K \leqq 3$,

$m_{pqr} = k_{pqr}$; and (3-7)

for K=4,

$$m_{400} = k_{400} + 3,\ m_{040} = k_{040} + 3,\ m_{004} = k_{004} + 3,$$
$$m_{310} = k_{310} + 3m_{110},\ m_{301} = k_{301} + 3m_{101},\ \cdots\cdots,\ m_{013} = k_{013} + 3m_{011},$$
$$m_{220} = k_{220} + 2(m_{110})^2 + 1,\ \cdots\cdots,\ m_{112} = k_{112} + 2m_{101}m_{011} + m_{110}.$$

Similarly, the relations for $K \geqq 5$ can be deduced, but the calculations become increasingly cumbersome.

Now, the Gaussian joint pdf can be written as:

$$P_G(\hat{u},\hat{v},\hat{t}) = \exp\{-\left(\sum_{i,j=1}^{3} \Delta_{ij}\hat{x}_i\hat{x}_j\right)/(2|\mathbb{R}|)\}/\{(2\pi)^{3/2}\sqrt{|\mathbb{R}|}\} \qquad (3\text{-}8)$$

with $\hat{x}_1 = \hat{u}$, $\hat{x}_2 = \hat{v}$ and $\hat{x}_3 = \hat{t}$,

where

$$\mathbb{R} = \begin{pmatrix} 1 & R_{12} & R_{13} \\ R_{12} & 1 & R_{23} \\ R_{13} & R_{23} & 1 \end{pmatrix}$$; Δ_{ij} is the cofactor of the matrix $\mathbb{R}$; and

R_{ij} denotes the correlation coefficient between χ_i and χ_j ($= \overline{\hat{\chi}_i \hat{\chi}_j}$). In a Gaussian field given by Eq.(3-8), moments and cumulants preserve the following characteristics.

(a) Odd-order moments (i.e., K is odd) are all zero.

(b) Even-order moments (i.e., K is even) can be represented by zero- and second-order moments.

(c) For $K \geqq 3$, all cumulants are zero.

In statistical analysis of a field close to Gaussian, the above characteristic (c) is quite useful. It is generally recognized that probability distributions of turbulent phenomena do not deviate largely from a Gaussian distribution. Hence, adopting [B] for describing ψ and using the characteristic (c), we can accurately represent the pdf $P(\hat{u},\hat{v},\hat{t})$ with a small number of series-expansion terms. From Eqs.(3-6) and (3-7), we obtain:

$$\psi(\xi,\eta,\zeta) = \exp\{-(\xi^2+\eta^2+\zeta^2+2R_{uv}\xi\eta+2R_{ut}\xi\zeta+2R_{vt}\eta\zeta)/2 + \sum_{K\geqq 3}^{\infty} \frac{j^K}{p!\,q!\,r!} k_{pqr}\xi^p\eta^q\zeta^r\} \qquad (3\text{-}9)$$

where $k_{110} = m_{110} = \overline{\hat{u}\hat{v}} = R_{uv}$, $k_{101} = R_{ut}$ and $k_{011} = R_{vt}$. Equation (3-9) can be rewritten in either of two ways:

$$\psi(\xi,\eta,\zeta) = \exp\{-(\xi^2+\eta^2+\zeta^2)/2\} \sum_{p,q,r=0}^{\infty} C_{pqr} j^K \xi^p\eta^q\zeta^r \qquad (3\text{-}10)$$

$$\psi(\xi,\eta,\zeta) = \exp\{-(\xi^2+\eta^2+\zeta^2+2R_{uv}\xi\eta+2R_{ut}\xi\zeta+2R_{vt}\eta\zeta)/2\}$$

$$\times \sum_{p,q,r=0}^{\infty} D_{pqr}\, i^K\, \xi^p \eta^q \zeta^r \qquad (3\text{-}11)$$

where C_{pqr} and D_{pqr} are the coefficients in the power-series expansion of Eq.(3-9). If we use Eq.(3-10), the final form for $P(\hat{u},\hat{v},\hat{t})$ is expressed by the products of one-dimensional Hermite polynomials. On the other hand, with Eq.(3-11), $P(\hat{u},\hat{v},\hat{t})$ is represented by three-dimensional conjugate Hermite polynomials. The study by Antonia & Atkinson (1973) on a two-dimensional pdf with two random variables, showed that an expression with conjugate Hermite polynomials predicted the experimental results a little more closely than with one-dimensional Hermite polynomials. However, even in their two-dimensional analysis, numerous series-expansion terms were needed for the pdf, and the expression was complex. Since, in the present study, the third-order moments in a three-dimensional field is analyzed, the use of Eq.(3-11) will obviously make mathematical treatment extremely difficult. In addition, to apply a pdf to multisided analyses of transport processes of momentum and heat and to modelling third-order moments, it is desirable to keep the number of parameters as few as possible. Hence, expression (3-10) is adopted.

Substituting the characteristic function (3-10) into Eq.(3-1) and performing the inverse Fourier transform, we obtain the following general representation for $P(\hat{u},\hat{v},\hat{t})$:

$$P(\hat{u},\hat{v},\hat{t}) = \frac{1}{(2\pi)^3} \iiint_{-\infty}^{\infty} \psi(\xi,\eta,\zeta) \exp\{-i(\hat{u}\xi + \hat{v}\eta + \hat{t}\zeta)\} d\xi\, d\eta\, d\zeta$$

$$= \frac{1}{(2\pi)^{3/2}} \sum_{p,q,r=0}^{\infty} C_{pqr} H_p(\hat{u}) H_q(\hat{v}) H_r(\hat{t}) \exp\{-(\hat{u}^2+\hat{v}^2+\hat{t}^2)/2\} \quad (3\text{-}12)$$

where

$$H_n(\chi) = (-1)^n \exp\left(\frac{\chi^2}{2}\right) \frac{d^n}{d\chi^n} \exp\left(-\frac{\chi^2}{2}\right) \quad (3\text{-}13)$$

$H_n(\chi)$ is an Hermite polynomial. The subsequent analysis has been made for $K \leqq 4$. Calculating C_{pqr} from Eqs.(3-9) and (3-10) yields:

$$\begin{aligned}
&C_{000} = 1,\ C_{100} = C_{010} = C_{001} = 0,\ C_{200} = C_{020} = C_{002} = 0,\\
&C_{110} = R_{uv},\ C_{101} = R_{ut},\ C_{011} = R_{vt},\ C_{300} = k_{300}/6,\ C_{030} = k_{030}/6,\ \cdots,\\
&C_{210} = k_{210}/2,\ \cdots\cdots,\ C_{012} = k_{012}/2,\ C_{111} = k_{111},\\
&C_{400} = k_{400}/24,\ \cdots\cdot,\ C_{310} = k_{310}/6,\ \cdots\cdot,\ C_{013} = k_{013}/6,\\
&C_{220} = (k_{220} + 2R_{uv}^2)/4,\ C_{202} = (k_{202} + 2R_{ut}^2)/4,\ \cdots\cdot,\ C_{112} = (k_{112} + 2R_{ut}R_{vt})/2.
\end{aligned} \quad (3\text{-}14)$$

The coefficients listed above are determined from the measured correlations up to the fourth order (see Eq.(3-7)).

CHAPTER IV

HIGH-ORDER MOMENTS AND PROBABILITY DISTRIBUTIONS OF VELOCITY AND TEMPERATURE

4.1. Distributions of Turbulence Quantities in Velocity and Thermal Fields

The distributions of r.m.s. amplitude of velocity component and temperature fluctuations normalized by the friction velocity u_τ and friction temperature t_τ are presented as a function of y^+ in Fig. 4.1. The maximum production of turbulence energy and temperature variance occurs near the heat-transfer surface ($y^+=10\sim 20$), where the existence of coherent motions is most pronounced (Nagano & Hishida 1985). Intensities of u and t fluctuations also peak in this region. The r.m.s. values of v fluctuations are much smaller than those of u and w in the wall region. This is because the preferential damping of v fluctuations increases sharply as the wall is approached. At the pipe centerline, intensities of u, v and w fluctuations become nearly identical, thus indicating the existence of the apparent isotropic structure. The intensity of u fluctuations in an isothermal flow measured in the same pipe using an X-array probe with two V-shaped hot-wires (Fig. 2.2(b)) is also shown in Fig. 4.1. Evidently, the influence of heat input is immaterial over most of the pipe section. The r.m.s. values of v and w fluctuations in the wall region are compared with those obtained by Laufer (1954) and by Kreplin & Eckelmann (1979). The present profiles for the near-wall region ($y^+<30$) agree well with the results by Kreplin & Eckelmann. In the region $y^+>30$, the data of Kreplin & Eckelmann become smaller than the present

measurements, because this region in their low-Reynolds-number experiment (Re$\simeq$ 7700) corresponds to the outer region of the flow.

The normalized Reynolds shear stress (i.e., momentum transfer) and turbulent heat fluxes are shown in Fig. 4.2. For a fully-developed turbulent pipe flow, the Reynolds shear stress $\overline{uv}$ and the radial turbulent heat flux $\overline{vt}$ can be calculated from the momentum and energy equations. The profiles thus obtained are expressed with the following equations:

$$-\overline{uv}/u_\tau^2 = (1 - y^+/r_0^+) - \partial\overline{U}^+/\partial y^+ \tag{4-1}$$

$$\frac{\overline{vt}}{u_\tau t_\tau} = \frac{r_0^+}{r_0^+ - y^+}\frac{(\overline{U}^+\overline{T}^+)_c}{(\overline{U}^+\overline{T}^+)_{ov}} - \frac{1}{Pr}\frac{\partial\overline{T}^+}{\partial y^+} \tag{4-2}$$

where

$$(\overline{U}^+\overline{T}^+)_c = \int_{y^+}^{r_0^+} (r_0^+ - y^+)\overline{U}^+\overline{T}^+ dy^+ \tag{4-3}$$

$$(\overline{U}^+\overline{T}^+)_{ov} = \int_{0}^{r_0^+} (r_0^+ - y^+)\overline{U}^+\overline{T}^+ dy^+ \tag{4-4}$$

which are respectively shown by the broken and chain lines in Fig. 4.2. Obviously, the present direct measurements of $\overline{uv}$ and $\overline{vt}$ are in almost complete agreement with those calculated from Eqs.(4-1) and (4-2).

The cross-correlation coefficients, which are indicative of the degree of both similarity in waveforms and difference in phase, are defined by:

$$R_{uv} = \overline{\hat{u}\hat{v}}, \quad R_{ut} = \overline{\hat{u}\hat{t}}, \quad R_{vt} = \overline{\hat{v}\hat{t}} \tag{4-5}$$

As seen in Fig. 4.3, the cross-correlation coefficient between u and v, R_{uv}, and that between v and t, R_{vt}, are almost equal in the absolute values. The correlation coefficient R_{uv} remains constant at -0.47 over most of the pipe section from within the buffer layer out to the core region of the flow ($10<y^+<400$; $0.011<y/r_o<0.45$). In the near-wall region, R_{uv} becomes a bit higher than R_{vt} ($R_{vt}\simeq 0.45$, $-R_{uv}\simeq 0.50$), while in the near-centerline region isotropy of the fluctuating velocity-temperature field is approached with a vanishing of both correlation coefficients. As for the cross-correlation between velocity and temperature fluctuations near the wall, very little information has appeared to date. There are, however, several published data for correlation coefficients in the outer region of the flow. For pipe flow turbulence, Bremhorst & Bullock (1973) obtained the values of $R_{vt}=0.47$ and $-R_{uv}=0.43$. For boundary layer flows, the corresponding values are: $R_{vt}=0.49$, and $-R_{uv}=0.47$ measured by Subramanian & Antonia (1981); $R_{vt}=0.57$ and $-R_{uv}=0.47$ by Verriopoulos (1983). The present values of R_{vt} and $-R_{uv}$ in the core region are in good agreement with these published data. The important finding in this study is that heat and momentum transfer correlation coefficients in the wall region have practically the same values as those for the outer region.

Values of $-R_{ut}$ are greater than those of R_{vt} throughout the pipe section, thus indicating that the temperature fluctuations are better correlated with the streamwise than the transverse velocity components. At the pipe centerline, R_{ut} does not vanish even though isotropy is generally thought to be approached in this region. From all these

measurements, we may conclude that the relation $-R_{ut} > R_{vt} \simeq -R_{uv}$ generally holds true.

4.2. Probability Density Distributions of Velocity and Temperature Fluctuations

The pdf distributions $P(\hat{v})$ and $P(\hat{t})$ at various locations, from within the sublayer out to the pipe centerline (y^+=863.0), are shown in Fig. 4.4. The solid lines indicate the theoretical values derived from Eq.(3-12), and the broken lines represent the Gaussian distributions. Thus, the theoretical values of $P(\hat{v})$, $P(\hat{t})$ and the first-order Gaussian pdf $P_G(\chi)$ are given by:

$$P(\hat{v}) = \int\int_{-\infty}^{\infty} P(\hat{u},\hat{v},\hat{t})\, d\hat{u}\, d\hat{t}$$

$$= P_G(\hat{v}) \{ 1 + C_{030} (\hat{v}^3 - 3\hat{v}) + C_{040} (\hat{v}^4 - 6\hat{v}^2 + 3) \} \qquad (4\text{-}6a)$$

$$P(\hat{t}) = P_G(\hat{t}) \{ 1 + C_{003} (\hat{t}^3 - 3\hat{t}) + C_{004} (\hat{t}^4 - 6\hat{t}^2 + 3) \} \qquad (4\text{-}6b)$$

$$P_G(\chi) = \exp(-\chi^2/2)/\sqrt{2\pi} \quad , \qquad \chi = \hat{v} \text{ or } \hat{t} \qquad (4\text{-}7)$$

The $P(\hat{v})$ curve is very close to Gaussian near the wall. A departure from the Gaussian distribution, however, occurs in the log-law region and in the

core region of the flow. The $P(\hat{t})$ curve, on the other hand, is strongly skewed to the negative side of t very near the wall, although it may be approximated with a Gaussian distribution in the log-law region. Inversely, $P(\hat{u})$ is skewed positively in the near-wall region (not shown). The measurement of a joint pdf $P(\hat{u}, \hat{v})$ shown in Fig. 4.5(a) indicates that the sweep-type motions, rushing into the near-wall region from regions away from the wall, predominate in the near-wall structure, i.e., the large-amplitude motions with u positive and v negative occur most frequently near the wall. The negatively skewed $P(\hat{t})$ and positively skewed $P(\hat{u})$ distributions are the consequence of these inrushes of low-enthalpy and high-momentum fluid. Totally opposite trends are observed in the core region, reflecting the dominant influence of high-enthalpy and low-momentum fluid ejections from the wall region. These unique features, as seen from Fig. 4.4, are almost perfectly predicted by Eq.(4-6).

The theoretical value of $P(\hat{u}, \hat{v})$ derived from Eq.(3-12) becomes:

$$P(\hat{u},\hat{v}) = \int_{-\infty}^{\infty} P(\hat{u},\hat{v},\hat{t})\, d\hat{t}$$

$$= \frac{1}{2\pi} \sum_{p,q=0}^{K \leqq 4} C_{pq0}\, H_p(\hat{u})\, H_q(\hat{v}) \exp\{-(\hat{u}^2+\hat{v}^2)/2\} \qquad (4\text{-}8)$$

Comparison of predictions (Fig. 4.5(b)) with measurements (Fig. 4.5(a)) proves that Eq.(4-8) represents accurately a highly anisotropic velocity field near the wall. Equation (4-8) is also identical to the theoretical formula developed by Antonia & Atkinson (1973).

The shapes of pdf $P(\chi)$ are well marked by the skewness $S(\chi) = \overline{\hat{\chi}^3}$ and the flatness factor $F(\chi) = \overline{\hat{\chi}^4}$. The former is particularly indicative of

the probabilistic asymmetry of χ and the latter is a measure of symmetrical peakedness of the probability. A random variable with a Gaussian pdf has values of $S(\chi)=0$ and $F(\chi)=3$. The skewness and flatness factors of u, v and t fluctuations are shown in Figs. 4.6 and 4.7, respectively. The skewness factor S(u) becomes negative in the outer region and positive in the near-wall region, while it is approximately zero over the fully turbulent log region. It is conceivable that a marked change in S(u) for $y^+<20$ is a reflection of the existence of coherent motions near the wall. Measurements of S(u) and S(t) indicate that u and t fluctuations are skewed in the opposite direction. In contrast, S(v) is essentially positive over most of the pipe section.

Next, it is shown that the skewness factor is related closely to the fraction of time during which a random variable χ is positive (γ_+) or negative (γ_-). With Eq.(4-6), the time fraction $\gamma_\pm$ is expressed as:

$$\begin{aligned}\gamma_\pm(\chi) &= \int_0^\infty P(\pm\hat{\chi})\, d\hat{\chi} \\ &= \{\sqrt{\pi/2} \mp S(\chi)/6\} / \sqrt{2\pi}\end{aligned} \qquad (4\text{-}9)$$

Thus, Eq.(4-9) gives the following formula for $S(\chi)$:

$$S(\chi) = 3\sqrt{2\pi}\{\gamma_-(\chi) - \gamma_+(\chi)\} \qquad (4\text{-}10)$$

The values of $S(\chi)$ from Eq.(4-10), calculated using measurements of the time fractions, are compared with the present direct measurements of skewness factors in Fig. 4.6. Agreement is seen to be almost perfect. This is important knowledge which demonstrates that the skewness factor characterizing turbulence structures can be represented with the time

fractions (i.e., intermittency factor) occupied by positive or negative events of a turbulence component.

The flatness factors F(u) and F(t) present similar distributions which are very close to the Gaussian value of 3 in the log-law region. And the skewness factors of u and t are nearly equal to zero in this region. Thus, the assumption of the Gaussian for $P(\hat{u})$ and $P(\hat{t})$ distributions does not lead to a noticeable error, as evidenced in Fig. 4.4. Besides, F(t) becomes minimum at a location where temperature variance attains a maximum (see Section 4.1), which provides a good similarity to F(u) behaviour (Zarić 1979). Values of F(v), on the other hand, deviate considerably from the Gaussian value over a greater part of the pipe section (see Fig. 4.4).

A full knowledge of skewness and flatness factors near the wall is also required to investigate the coherent structures of wall turbulence. However, we can refer to few reliable measurements of these factors (Zarić 1979), particularly for v and t, so accumulation of accurate data can be expected. The present distributions of S(u) and F(u) agree quite well with the recent measurements in a flat-plate boundary layer (Durst et al. 1987).

4.3. Probability Density Distributions of Second-Order Moments

The pdf distributions of Reynolds shear stress uv and turbulent heat flux vt are shown in Figs. 4.8(a) and (b), respectively. The solid line stands for the theoretical pdf $P_{II}(x)$ for a second-order moment derived from

Eq.(3-12). The pdf of uv has been studied by Lu & Willmarth (1973), Antonia & Atkinson (1973) and Nakagawa & Nezu (1977), but a systematic investigation of the pdf of vt has not been performed so far.

The theoretical pdf $P_{II}(x)$ can be obtained by differentiating a cumulative probability distribution function $F_{II}(x)$ with respect to x. In the case of $x= \hat{v}\hat{t}$, a definition of $F_{II}(x)$ is:

$$F_{II}(x) = \text{Prob}\{ \hat{v}\hat{t} < x \} \tag{4-11}$$

The corresponding representation in the (v, t)-plane yields:

$$F_{II}(x) = \int_{-\infty}^{0} \left[\int_{x/\hat{v}}^{\infty} \left\{ \int_{-\infty}^{\infty} P(\hat{u},\hat{v},\hat{t})\, d\hat{u} \right\} d\hat{t} \right] d\hat{v} + \int_{0}^{\infty} \left[\int_{-\infty}^{x/\hat{v}} \left\{ \int_{-\infty}^{\infty} P(\hat{u},\hat{v},\hat{t})\, d\hat{u} \right\} d\hat{t} \right] d\hat{v} \tag{4-12}$$

Differentiation of Eq.(4-12) with respect to x leads to:

$$\begin{aligned} P_{II}(\hat{v}\hat{t}) &= d F_{II}(x) / d x \\ &= \int_{0}^{\infty} \left[\int_{-\infty}^{\infty} \{ P(\hat{u},-\hat{v},-x/\hat{v}) + P(\hat{u},\hat{v},x/\hat{v}) \}\, d\hat{u} \right] d\hat{v}/\hat{v} \\ &= \frac{1}{\pi} \sum_{q+r=\text{even}}^{K \leqq 4} C_{0qr} \int_{0}^{\infty} H_q(\hat{v})\, H_r(x/\hat{v}) \exp[-\{\hat{v}^2 + (x/\hat{v})^2\}/2]\, d\hat{v}/\hat{v} \end{aligned} \tag{4-13}$$

Similarly, the pdf for $\hat{u}\hat{v}$ is derived as:

$$P_{II}(\hat{u}\hat{v}) = \frac{1}{\pi} \sum_{p+q=\text{even}}^{K \leqq 4} C_{pq0} \int_{0}^{\infty} H_p(\hat{u})\, H_q(x/\hat{u}) \exp[-\{\hat{u}^2 + (x/\hat{u})^2\}/2]\, d\hat{u}/\hat{u} \tag{4-14}$$

As shown in Fig. 4.8, though skewed opposite, the distributions of $P_{II}(\hat{u}\hat{v})$ and $P_{II}(\hat{v}\hat{t})$ are seen to be similar in every respect. The shapes of pdf change little with radial location, from within the wall region out to the core region of the flow, which corresponds to constancy in correlation coefficients ($R_{uv} \simeq -0.5$ and $R_{vt} \simeq 0.5$) over these regions (see Section 4.1). The long tails of pdf substantiate the highly intermittent nature of momentum and heat transfer. At the pipe centerline, R_{uv} and R_{vt} are zero, and both $P_{II}(\hat{u}\hat{v})$ and $P_{II}(\hat{v}\hat{t})$ distributions become symmetrical. It is evident from Figs. 4.8(a) and (b) that the theoretical predictions from Eqs.(4-13) and (4-14) follow the experimental trend quite closely.

4.4. Turbulent Diffusion of Turbulence Energy Components, Temperature Variance, Reynolds Shear Stress and Turbulent Heat Fluxes

4.4.1. Comparison of measurements of turbulent diffusion with predictions by existing models for triple products

The distributions of turbulent diffusion, i.e., third-order moments, of turbulence energy components u^2 and v^2, temperature variance t^2, Reynolds shear stress uv, and turbulent heat fluxes ut and vt are presented in Figs. 4.9(a) and (b). The values predicted from the existing models for triple products $\overline{vuv}$ and $\overline{vvt}$, i.e., diffusion of uv and vt, are included in Fig. 4.9 so as to evaluate the performance of the models. A prime " ' " denotes the normalization of velocity and temperature by the friction velocity and friction temperature, respectively. The representative

existing models are as follows:

[I] Models for turbulent diffusion of Reynolds stress $\overline{u_i u_j u_k}$

(a) Daly & Harlow (1970)

$$\overline{u_i u_j u_k} = - C_{R1} \frac{k}{\varepsilon} \overline{u_k u_\ell} \frac{\partial \overline{u_i u_j}}{\partial x_\ell} \tag{4-15}$$

(b) Hanjalić & Launder (1972)

$$\overline{u_i u_j u_k} = -C_{R2} \frac{k}{\varepsilon} \left[\overline{u_\ell u_j} \frac{\partial \overline{u_i u_k}}{\partial x_\ell} + \overline{u_\ell u_i} \frac{\partial \overline{u_j u_k}}{\partial x_\ell} + \overline{u_\ell u_k} \frac{\partial \overline{u_i u_j}}{\partial x_\ell} \right] \tag{4-16}$$

(c) Cormack et al. (1978)

$$\begin{aligned} \overline{u_i u_j u_k} = {} & \frac{4k^2}{\varepsilon} \{ 2\alpha_1 (\delta_{ij} \delta_{k\ell} + \delta_{ik} \delta_{j\ell} + \delta_{kj} \delta_{i\ell}) \frac{\partial k}{\partial x_\ell} + \alpha_2 \left(\frac{\partial a_{ik}}{\partial x_j} + \frac{\partial a_{ij}}{\partial x_k} + \frac{\partial a_{kj}}{\partial x_i} \right) \} \\ & + \frac{2k}{\varepsilon} \{ 2\alpha_3 (\delta_{ik} a_{j\ell} + \delta_{ij} a_{k\ell} + \delta_{jk} a_{i\ell}) \frac{\partial k}{\partial x_\ell} \\ & + \alpha_4 \left(a_{ik} \frac{\partial a_{j\ell}}{\partial x_\ell} + a_{ij} \frac{\partial a_{k\ell}}{\partial x_\ell} + a_{kj} \frac{\partial a_{i\ell}}{\partial x_\ell} \right) \}, \end{aligned}$$

$$a_{ij} = \overline{u_i u_j} - 2\delta_{ij} k/3 \tag{4-17}$$

[II] Models for turbulent diffusion of heat flux $\overline{u_i u_j t}$

(a) Deardorff (1973)

$$\overline{u_i u_j t} = - \frac{k}{\varepsilon} \left[c_1 \overline{u_j u_\ell} \frac{\partial \overline{u_i t}}{\partial x_\ell} + c_2 \overline{u_i u_\ell} \frac{\partial \overline{u_j t}}{\partial x_\ell} + c_3 \overline{u_\ell t} \frac{\partial \overline{u_i u_j}}{\partial x_\ell} \right] \tag{4-18}$$

with $c_1 = c_2 = c_3 = c_{s1}$.

(b) Owen (1973)

One letting $c_3=0$, $c_1=c_2=c_{s2}$ in Eq.(4-18).

(c) Wyngaard & Cotè (1974)

One letting $c_2=c_3=0$, $c_1=c_{s3}$ in Eq.(4-18).

[III] Models for turbulent diffusion of temperature variance $\overline{u_j t^2}$

(a) Deardorff (1973)

One letting $u_i = t$ in [II] (a).

(b) Wyngaard (1975)

One letting $u_i = t$ in [II] (c).

where k and ε are the turbulence kinetic energy ($= \overline{u_i u_i}/2$) and dissipation rate of turbulence energy, respectively. Definitely, all are the gradient-type diffusion models. The model constants used in the present study are summarized in Table 4.2.

As shown in Fig. 4.9, turbulent diffusions pertaining to the velocity field are similarly distributed with maximums at approximately $y^+ \simeq 30$. The same applies to turbulent diffusions for the thermal field, in which the second peaks are seen to exist in the outer region. Comparing the calculated values of $-\overline{vuv}$ and $\overline{vvt}$ from the existing models with the experimental results, we find that all models fail to predict the measurements quantitatively for $y^+>100$ and even qualitatively for $y^+<100$, where the predictions present the trend opposite to the measurements. Accordingly, there is a risk that serious errors may be introduced into the results of predictions if these models are incorporated in the Reynolds stress and/or heat flux equation modelling.

4.4.2. Probability density distributions of third-order moments

For appropriate modelling, it is necessary to investigate the statistical characteristics of third-order moments in detail and give a theoretical explanation for them. Figure 4.10 shows measurements of pdf distributions of third-order moments. Every pdf is nearly symmetrical about zero and has very long tails for positive and negative values of the abscissa, although not distributed in the Gaussian manner. Also, all of these distributions are too similar to be readily distinguished from others. This means that turbulent diffusion is a very intermittent phenomenon and that the magnitude and direction of time-averaged diffusion are determined by a delicate imbalance (i.e., asymmetry) of pdf distribution.

To illustrate this situation, the theoretical pdf distributions for third-order moments $P_{III}(\hat{v}\hat{u}\hat{v})$, $P_{III}(\hat{v}\hat{v}\hat{t})$ and $P_{III}(\hat{v}\hat{u}\hat{t})$ are derived from a non-Gaussian joint pdf (3-12). Following the same procedure as for the second-order moments (cf. Eqs.(4-13) and (4-14)), we get $P_{III}(x)$ for $x= \hat{v}\hat{u}\hat{v}$, $\hat{v}\hat{v}\hat{t}$ and $\hat{v}\hat{u}\hat{t}$ as:

$$P_{III}(\hat{v}\hat{u}\hat{v}) = \int_0^{\infty}\int_{-\infty}^{\infty} \{P(x/\hat{v}^2,\hat{v},\hat{t}) + P(x/\hat{v}^2,-\hat{v},\hat{t})\}\, d\hat{t}\, d\hat{v}/\hat{v}^2$$

$$= \frac{1}{\pi} \sum_{q=even}^{K\leqq 4} C_{pq0} \int_0^{\infty} H_p(x/\hat{v}^2)\, H_q(\hat{v})\, \exp[-\{(x/\hat{v}^2)^2+\hat{v}^2\}/2]\, d\hat{v}/\hat{v}^2 \qquad (4\text{-}19)$$

$$P_{III}(\hat{v}\hat{v}\hat{t}) = \int_0^{\infty}\int_{-\infty}^{\infty} \{P(\hat{u},\hat{v},x/\hat{v}^2) + P(\hat{u},-\hat{v},x/\hat{v}^2)\}\, d\hat{u}\, d\hat{v}/\hat{v}^2$$

$$= \frac{1}{\pi} \sum_{q=even}^{K\leqq 4} C_{0qr} \int_0^{\infty} H_q(\hat{v})\, H_r(x/\hat{v}^2)\, \exp[-\{\hat{v}^2+(x/\hat{v}^2)^2\}/2]\, d\hat{v}/\hat{v}^2 \qquad (4\text{-}20)$$

$$P_{III}(\hat{v}\hat{u}\hat{t}) = \int_0^\infty\int \{P(\hat{u},\hat{v},x/\hat{u}\hat{v}) + P(-\hat{u},\hat{v},-x/\hat{u}\hat{v})$$

$$+ P(-\hat{u},-\hat{v},x/\hat{u}\hat{v}) + P(\hat{u},-\hat{v},-x/\hat{u}\hat{v})\}\, d\hat{u}\, d\hat{v}/\,\hat{u}\hat{v} \qquad (4\text{-}21)$$

The pdf based on an assumption of Gaussian behaviour, $P_{G_{III}}(x)$, is similarly obtained using Eq.(3-8) instead of Eq.(3-12).

The measured pdf distributions of $\hat{v}\hat{u}\hat{v}$ and $\hat{v}\hat{v}\hat{t}$ are presented in Fig. 4.11, compared with the theoretical predictions from Eqs.(4-19) and (4-20) and those based on a Gaussian joint pdf. Evidently, the asymmetry in pdf distributions is fractional. But it is this asymmetry that determines the net value of turbulent diffusion. If a theory is developed on the basis of an assumption of Gaussian behaviour, the pdf distributions of third-order moments become symmetrical about zero. Consequently, time-averaged values of third-order moments (i.e., expectations of instantaneous third-order moments) are consistently zero, and the important characteristics of turbulent diffusion are not described fully. However, as seen from Fig. 4.11, the present theoretical models (4-19) and (4-20) can precisely predict the asymmetry in pdf distributions, thus yielding the correct values of third-order moments.

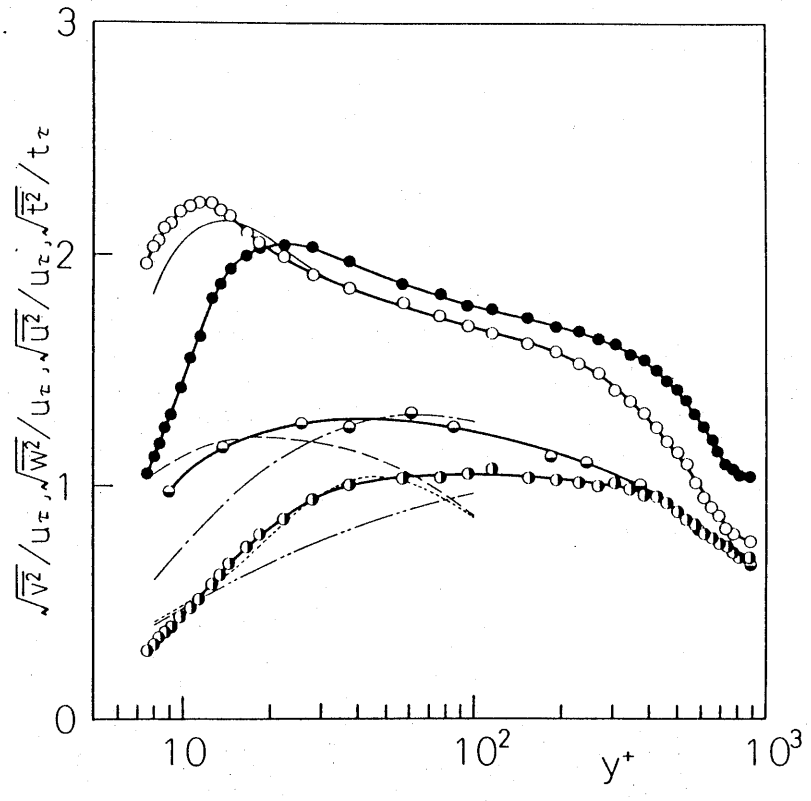

Fig. 4.1. Distributions of intensities of velocity and temperature fluctuations. —○—, $\sqrt{\overline{u^2}}/u_\tau$; —◑—, $\sqrt{\overline{v^2}}/u_\tau$; —◒—, $\sqrt{\overline{w^2}}/u_\tau$; —●—, $\sqrt{\overline{t^2}}/t_\tau$; ———, $\sqrt{\overline{u^2}}/u_\tau$, isothermal; — — —, $\sqrt{\overline{v^2}}/u_\tau$, Laufer 1954; ·····, $\sqrt{\overline{v^2}}/u_\tau$, Kreplin & Eckelmann 1979; —·—, $\sqrt{\overline{w^2}}/u_\tau$, Laufer 1954; – – – –, $\sqrt{\overline{w^2}}/u_\tau$, Kreplin & Eckelmann 1979.

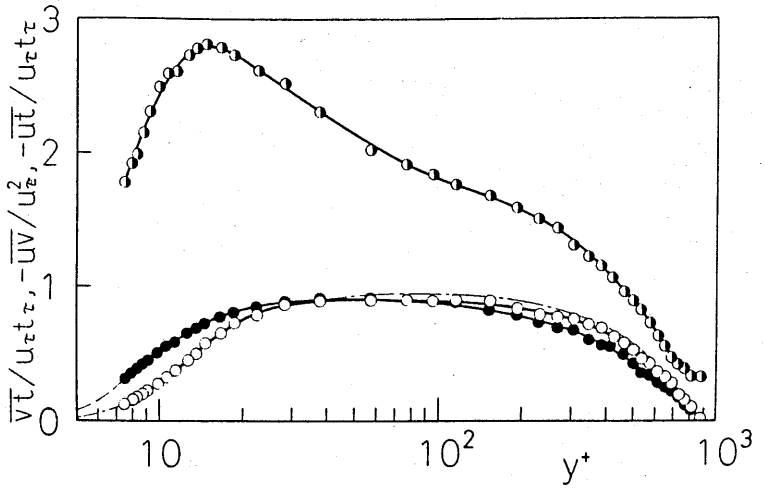

Fig. 4.2. Distributions of Reynolds shear stress and turbulent heat fluxes. —●—, $-\overline{uv}/u_\tau^2$; —◑—, $-\overline{ut}/u_\tau t_\tau$; —○—, $\overline{vt}/u_\tau t_\tau$; ———, Eq.(4-1); —·—, Eq.(4-2).

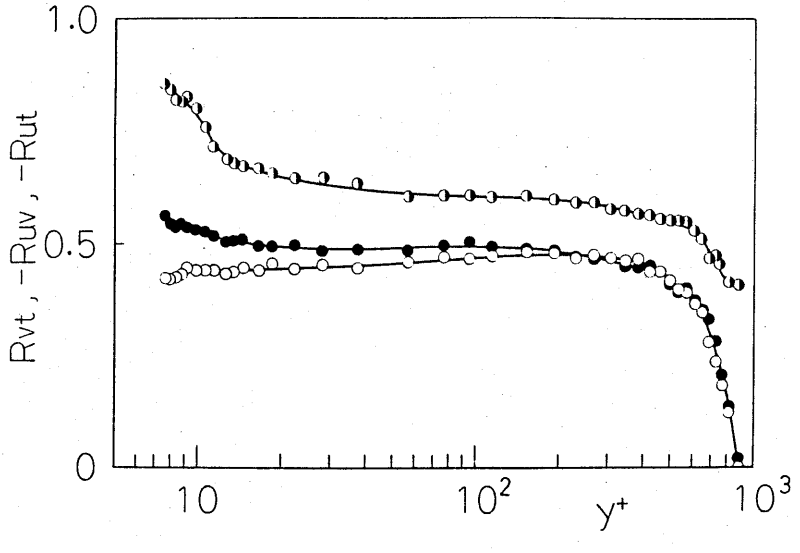

Fig. 4.3. Heat and momentum transfer correlation coefficients.
—●—, -Ruv; —◑—, -Rut; —○—, Rvt.

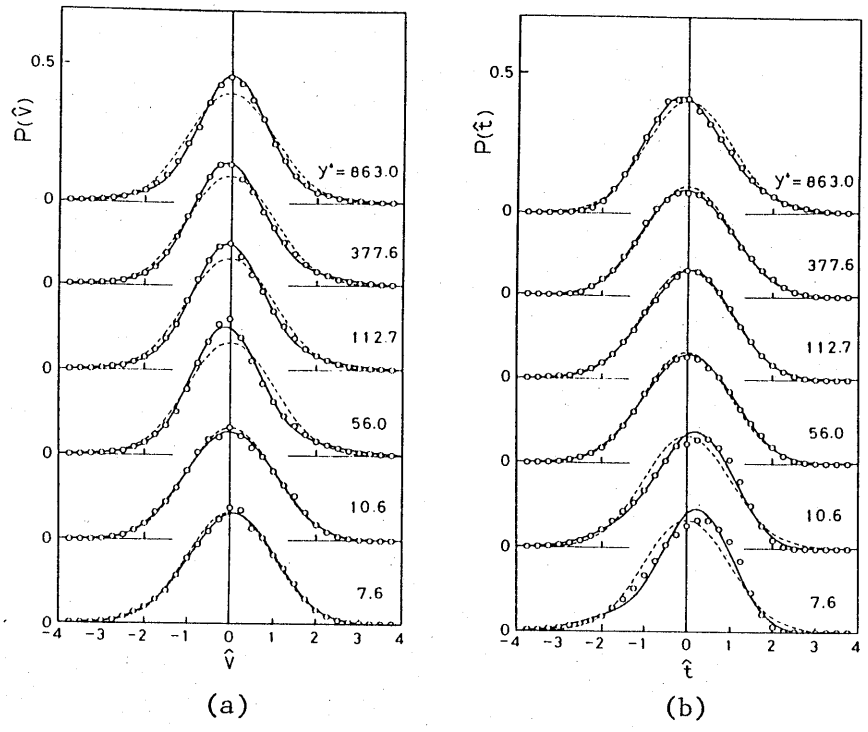

Fig. 4.4. Probability density distributions of velocity and temperature fluctuations.

(a) $P(\hat{v})$: ○ , experiment; ———— , Eq.(4-6a); – – – – , Gaussian;

(b) $P(\hat{t})$: ○ , experiment; ———— , Eq.(4-6b); – – – – , Gaussian.

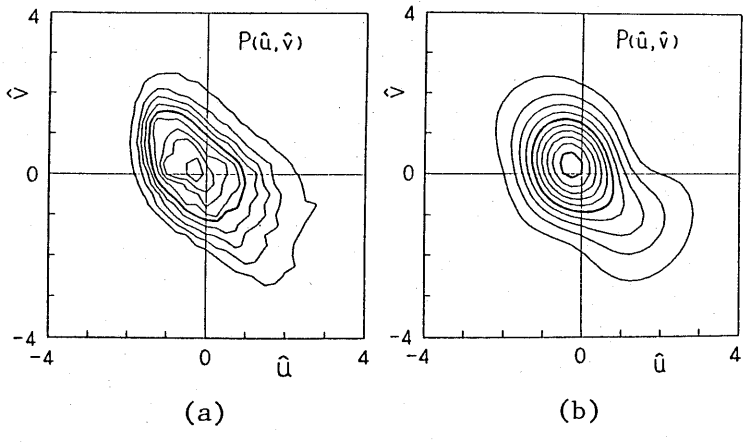

Fig. 4.5. Joint probability density of $\hat{u}$ and $\hat{v}$ (y^+=7.6). Lines are isocontours with an equal increment of 0.02.

(a) Experiment; (b) Prediction.

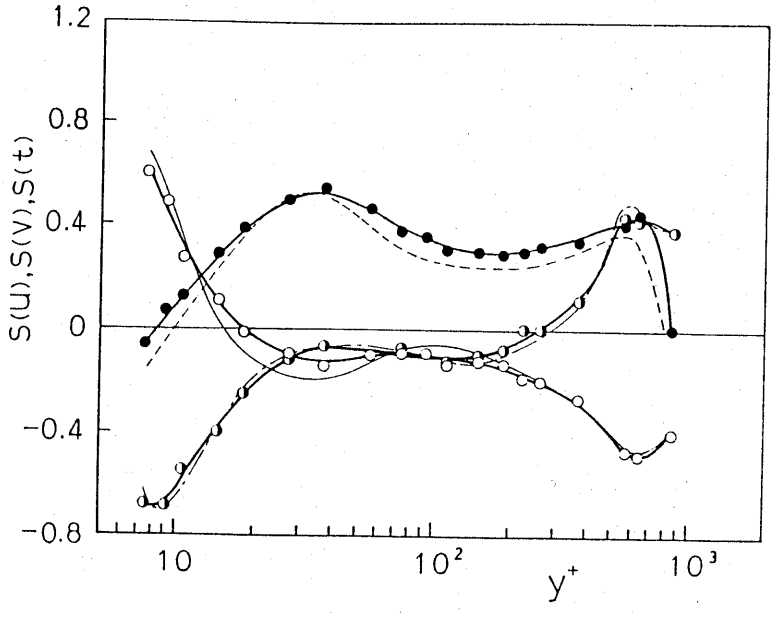

Fig. 4.6. Skewness factors. Experiments: —○—, S(u); —●—, S(v); —◑—, S(t). Calculations from Eq.(4-10): ———, S(u); – – – –, S(v); —·—, S(t).

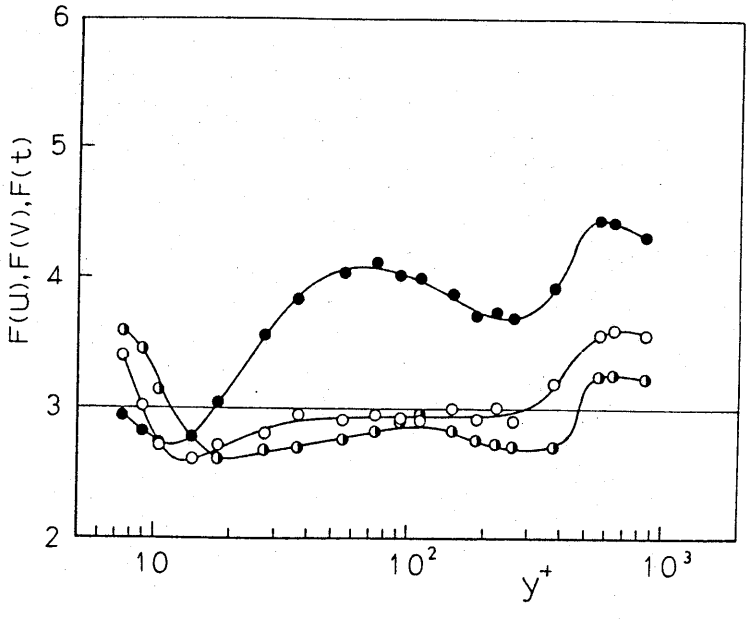

Fig. 4.7. Flatness factors. —○—, F(u); —●—, F(v); —◑—, F(t).

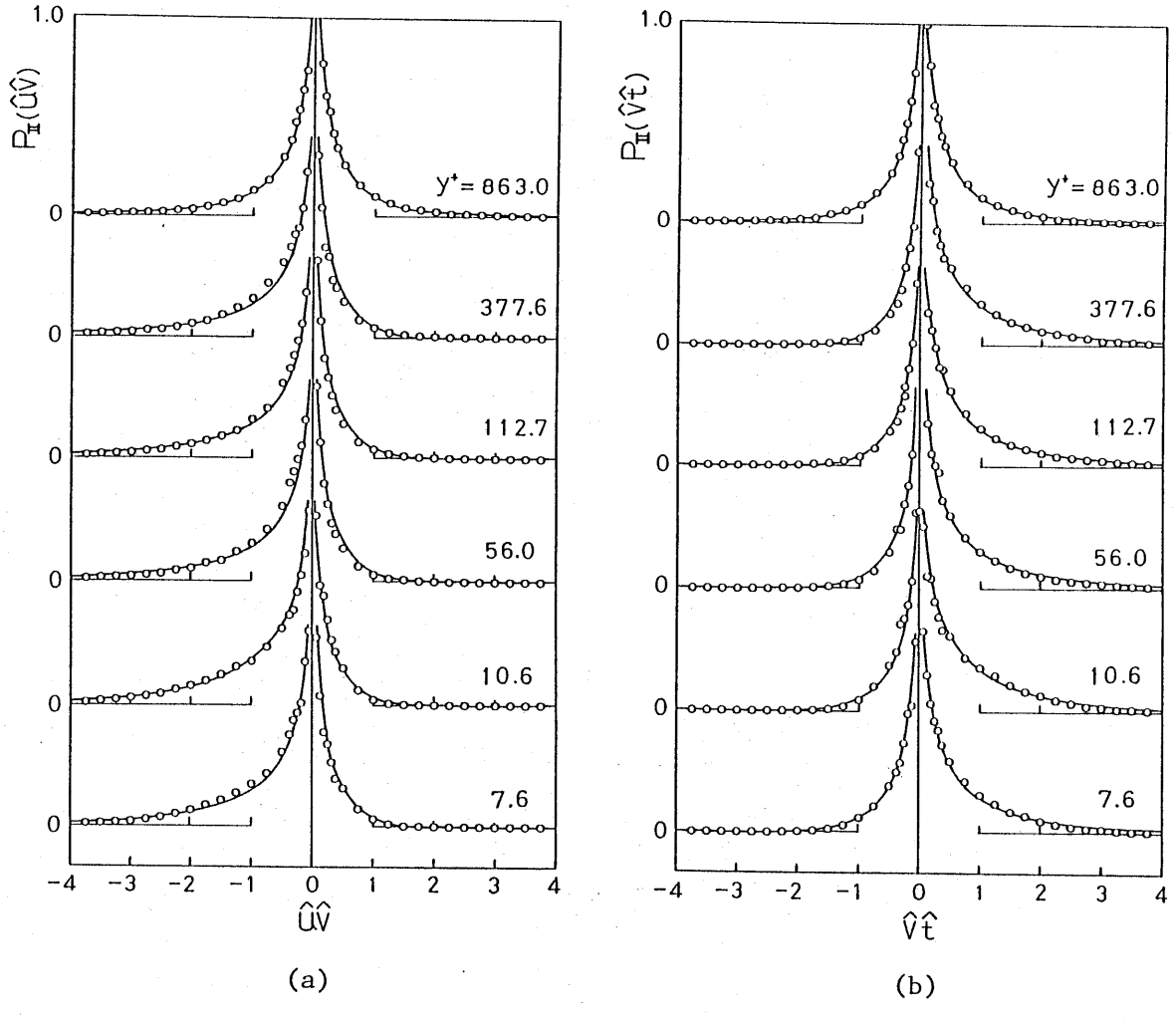

Fig. 4.8. Probability density distributions of Reynolds shear stress and turbulent heat flux.

(a) $P_{II}(\hat{u}\hat{v})$: ○ , experiment; ——— , Eq.(4-14);

(b) $P_{II}(\hat{v}\hat{t})$: ○ , experiment; ——— , Eq.(4-13).

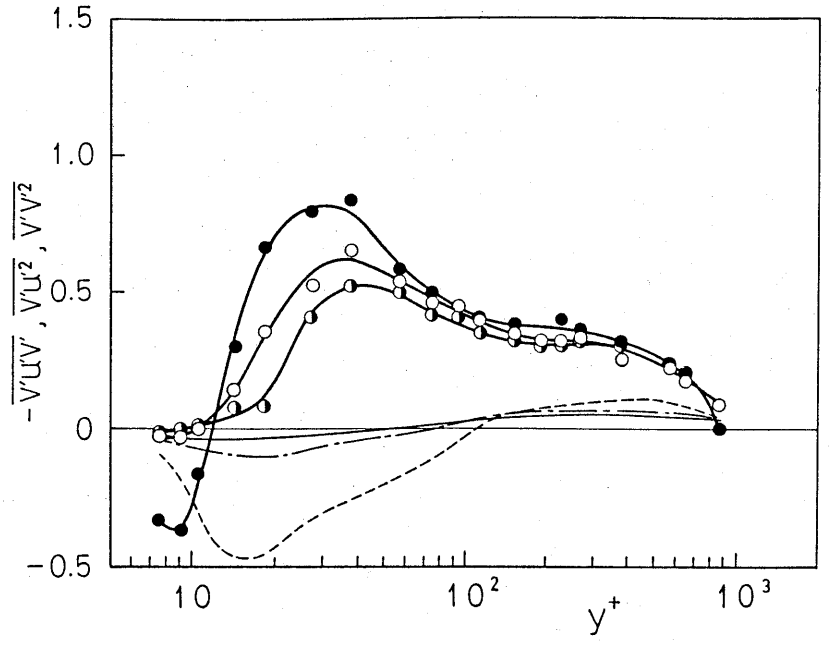

(a)

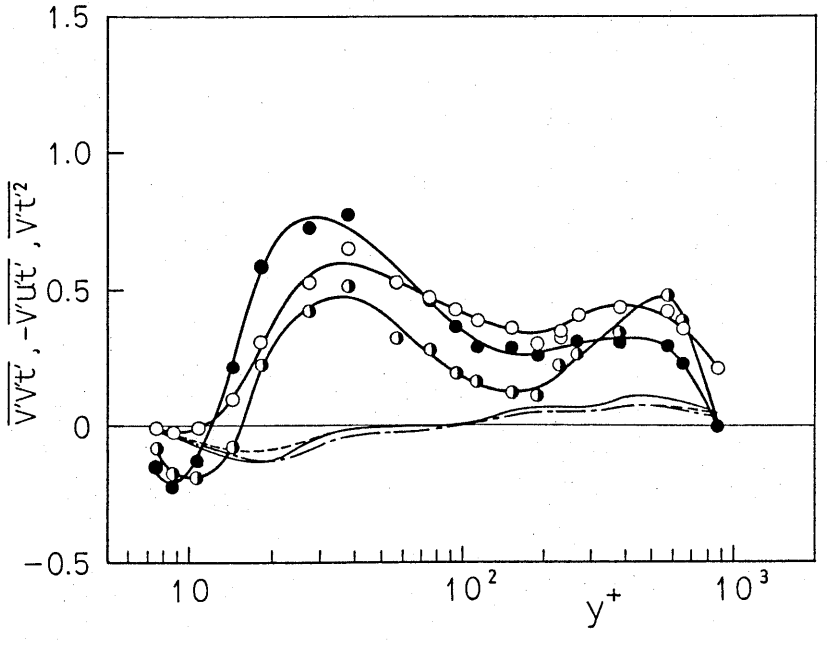

(b)

Fig. 4.9. Distributions of turbulent diffusion (third-order moments).

(a) Velocity field. Experiments: —○—, $-\overline{vuv}$; —●—, $\overline{vu^2}$; —◑—, $\overline{vv^2}$. Predictions for $-\overline{vuv}$: ———, Daly & Harlow; —·—, Hanjalić & Launder; – – – –, Cormack et al.;

(b) Thermal field. Experiments: —○—, $\overline{vvt}$; —●—, $-\overline{vut}$; —◑—, $\overline{vt^2}$. Predictions for $\overline{vvt}$: ———, Owen; —·—, Deardorff; – – – –, Wyngaard & Cotė.

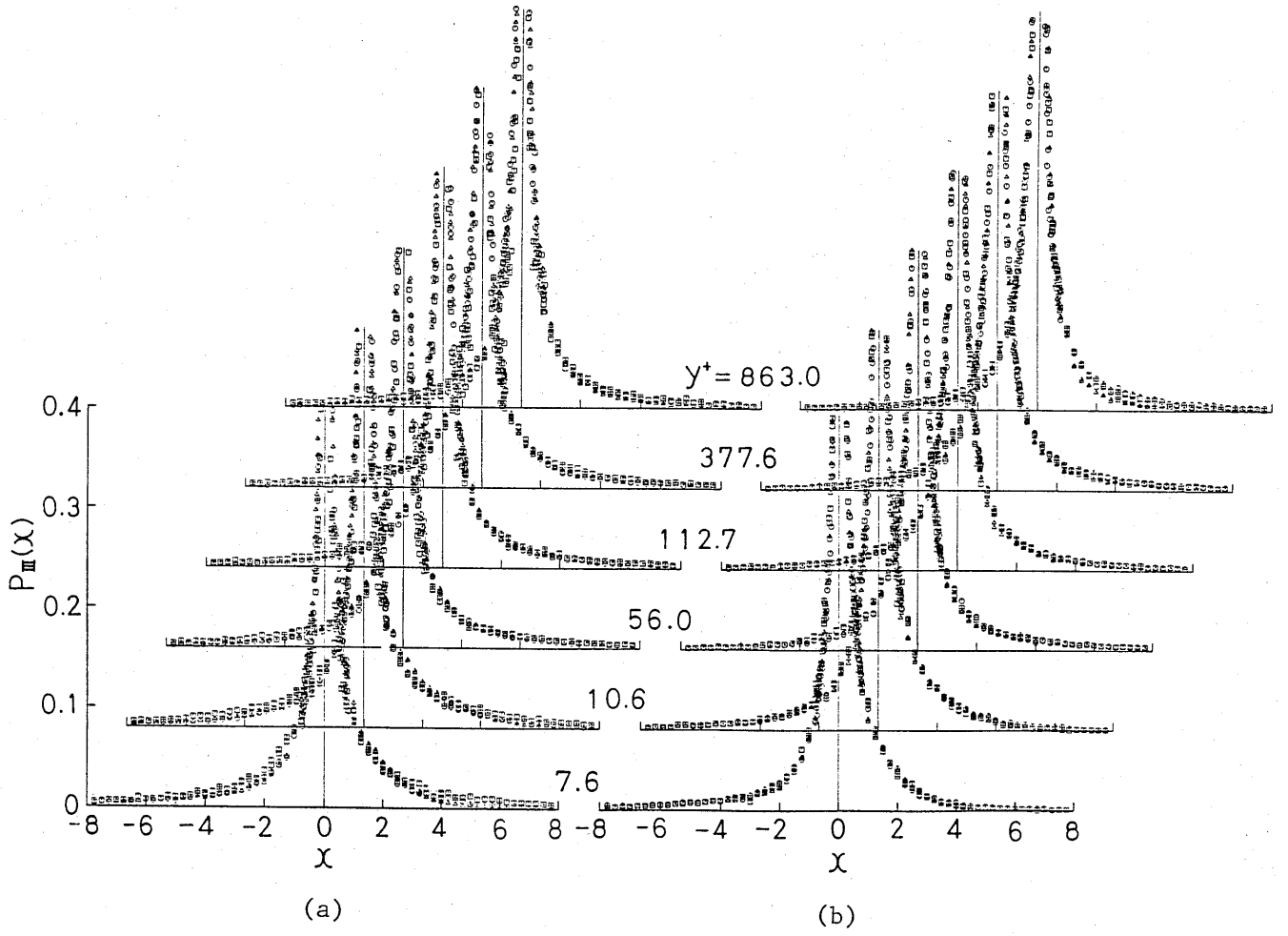

Fig. 4.10. Probability density distributions of third-order moments.
(a) Velocity field: ○ , $-\hat{v}\hat{u}\hat{v}$; △ , $\hat{v}\hat{u}^2$; □ , $\hat{v}\hat{v}^2$;
(b) Thermal field: ○ , $\hat{v}\hat{v}\hat{t}$; △ , $-\hat{v}\hat{u}\hat{t}$; □ , $\hat{v}\hat{t}^2$.

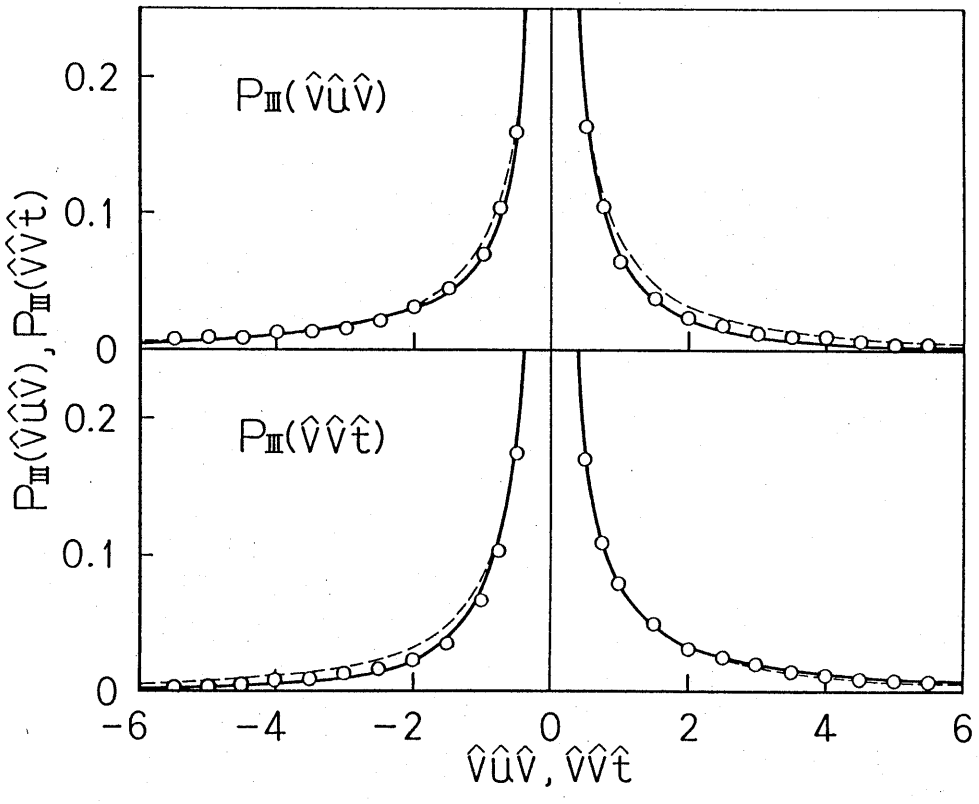

Fig. 4.11. Comparison of predictions with experimental results for probability density of third-order moments (y^+=37.1). ○ , experiments; ———, Eq.(4-19) for $P_{III}(\hat{v}\hat{u}\hat{v})$ and Eq.(4-20) for $P_{III}(\hat{v}\hat{v}\hat{t})$; – – – –, Gaussian.

Re	Rθ	$\bar{U}_c$ m/s	U_τ m/s	$\bar{T}_w$ °C	$\bar{T}_c$ °C	t_τ °C	q_w w/m2
4×10^4	1032	17.2	0.79	100.3	41.2	2.9	2333

Table 4.1. Characteristics of the flow.

Model for triple product	Constant	Value (Present work)
Daly & Harlow (1970)	C_{R1}	0.21
Hanjalić & Launder (1972)	C_{R2}	0.11
Cormack et al. (1978) (for all flows)	α_1	-8.14×10^{-3}
	α_2	-1.72×10^{-2}
	α_3	-4.80×10^{-2}
	α_4	-1.02×10^{-1}
Deardorff (1973)	C_{s1}	0.11
Owen (1973)	C_{s2}	0.11
Wyngaard & Coté (1974)	C_{s3}	0.13
Wyngaard (1975)	C_{s3}	0.13

Table 4.2. Model constants used in the existing models for triple products of velocity and temperature.

CHAPTER V

COHERENT MOTIONS AND THEIR ROLE IN HEAT TRANSPORT PROCESSES

5.1. Pictorial Structure Survey

The velocity and temperature profiles agreed with those fully developed profiles already generally accepted (Hishida & Nagano 1979). A pipe section can be partitioned into four basic flow zones: (i) the viscous sublayer ($y^+<5$), (ii) the buffer layer ($5<y^+<30$), (iii) the fully turbulent part of the wall region, i.e., log-law region, ($30<y^+<180\simeq 0.2r_o^+$), and (iv) the outer region ($y^+>0.2r_o^+$). Here, r_o^+ is the dimensionless pipe radius. In what follows, the characteristics of fluid flow and heat transfer structures are investigated in conjunction with these basic flow zones.

Typical instantaneous fluctuations of the velocity components u and v, temperature t, turbulence energy components u^2 and v^2, temperature variance t^2, turbulent momentum transfer (i.e., Reynolds shear stress) uv, and axial and radial turbulent heat fluxes, ut and vt, recorded simultaneously, are presented in Fig. 5.1. Figure 5.1(a) shows the records of the signals in the buffer layer where most intense turbulent mixing takes place. From this figure, the highly intermittent and spiky nature of turbulent heat and momentum transfer is apparent. Almost all large peaks of $uv<0$ and $vt>0$ are the consequence of inrushes of high-momentum and low-enthalpy fluid from the outer region ($v<0$, $u>0$, $t<0$), and low-momentum and high-enthalpy fluid ejections from the near-wall region ($v>0$, $u<0$, $t>0$). Also observed in this figure are the typical u-signal patterns of the ejection- and sweep-type motions consisting of a gradual deceleration from a local

maximum followed by a strong acceleration (Blackwelder & Kaplan 1976; Wallace, Brodkey & Eckelmann 1977).

Despite increasing distance from the wall, as in the outer region of the flow shown in Fig. 5.1(b), violent fluctuations of Reynolds shear stress and turbulent heat fluxes are still associated with ejection- and sweep-type motions. This indicates that the coherent motions originating in the wall region also play a very dominant role in determining the transport processes of heat and momentum in the outer region.

From these observations, the inherent intermittency of turbulent heat and momentum transfer can be regarded as the consequence of the intermittent coherent motions near the wall. Therefore, it is very important to detect the coherent structures accurately in order to clarify the transport phenomena in turbulent flows.

5.2. Description and Recognition of Coherent Motions

To investigate coherent structures, first fluid motions are classified into four types of events according to each quadrant of the (u, v)-plane. Four different types of motion and the properties of different quadrants are given in Table 5.1. As shown in Fig. 5.2, each classified motion has the deterministic mean period $\overline{T_i}$ and mean duration $\overline{\Delta T_i}$. The mean periods for each motion are essentially equal at a location, indicating that each classified motion on the average occurs at the same interval. In contrast to this, the mean durations of the two interaction-type motions (i=1, 3) are about half as large as those of the ejection- (i=2) and sweep-type

(i=4) motions. Thus, the fractions of time occupied by the ejections and sweeps are generally larger than those of the interactions.

From the pictorial structure survey presented in Section 5.1, it is clear that the coherent structures of wall turbulence afford the key to an understanding of the mechanism of turbulent heat transfer. Here, the important questions are: What are the relations between the ejection- and sweep-type motions (both motions play a main role in turbulent heat transfer)? What is the role of both interaction-type motions in turbulent heat transfer? How strongly do in fact the coherent structures and turbulent heat transfer correlate? To answer these questions fully, we must determine objectively coherent structures consisting of well-ordered motions from random time-series data and then describe them appropriately. The following procedure has been developed to judge whether the detected motions are the coherent motions.

In order to improve the accuracy of the recognition of coherent structures, it is often very effective to apply a detection algorithm to the localized fluctuations of turbulence quantities about their short-time temporal averages (moving-averages), i.e., to extract a specific structure covered with unnecessary large-scale fluctuations (Blackwelder & Kaplan 1976; Wallace, Brodkey & Eckelmann 1977). The localized fluctuating part of a turbulence quantity, $Q'(\tau)$, about the moving-average is given by:

$$Q'(\tau) = Q(\tau) - \frac{1}{T}\int_{\tau-T/2}^{\tau+T/2} Q(\tau')d\tau' \qquad (5\text{-}1)$$

where τ and τ' denote time, and T represents the averaging time. The accuracy of recognition of coherent structures can be improved by making

the averaging time T as short as possible. The value, however, has a lower limit so as not to influence average time-quantities characterizing the intermittent nature of coherent structures such as those shown in Fig. 5.2. The dependence of the evaluated mean duration of each classified motion, $\overline{\Delta T_i}$, with the averaging time T, is demonstrated in Fig. 5.3. Judging from this figure, the authors have employed $T=51.9\delta^*/\bar{U}_c$ as the most appropriate value in the present study. It has been also confirmed that the mean period and the mean duration calculated at other y locations by using this averaging time agree well with those given in Fig. 5.2.

If any organized motions exist truly in a flow, there should be a certain regularity in the trajectories of quadrant-sequences on the (u, v)-plane because of continuity of turbulent motions. In order to detect the coherent motions in a wall turbulent shear flow, an investigation of all possible trajectories on the (u, v)-plane is necessary, since various stages are observed in the evolution of coherent structures. Therefore, at the beginning, the frequencies of occurrence of a specific quadrant-sequence are investigated at various amplitudes of velocity fluctuations. Figure 5.4 shows an example of the results. Here, instantaneous velocity fluctuations, $u'(\tau)$ and $v'(\tau)$, are conditionally sampled and averaged using the detection function $I_i(\tau, H)$ given by:

$$I_i(\tau, H)=\begin{cases} 1, \text{ if } |u'(\tau)v'(\tau)| > H\sqrt{\overline{u'^2}}\sqrt{\overline{v'^2}} \text{ and point } (u', v') \\ \quad \text{is in quadrant i,} \\ 0, \text{ otherwise} \end{cases} \tag{5-2}$$

The parameter H in Eq.(5-2) is a threshold and permits a conditional sampling.

From Fig. 5.4, we can see that the trajectory in the sequence of [4]-[1]-[2] occurs much more frequently than that of [4]-[2]-[1], and the ejection- and sweep-type motions have larger amplitudes than the interaction-type motions. Strictly speaking, the importance of a trajectory to turbulent heat transfer is not necessarily expressed with the frequency of occurrence alone. It was established by Hishida & Nagano (1979) that large-amplitude fluid motions bring about strong correlations between the velocity and thermal fields and contribute largely to turbulent heat transfer. In addition, the frequency of occurrence of the trajectory detected with a high threshold is closely related to the frequency at H=0. Accordingly, we can evaluate the importance of a trajectory correctly with its frequency of occurrence at H=0.

All possible sequences of events have been investigated. Figures 5.5(a) and (b) show the sample results in the buffer layer and in the core region of the flow, respectively. Numbers appended to a trajectory denote the detected frequencies of quadrant-sequences for H=0. For example, in Fig. 5.5(a), the frequency of the quadrant-sequence [4]-[1] is 717, and that of [1]-[2] which follows the previous sequence [4]-[1] is 502. The frequencies of [1]-[3] and [1]-[4] which follow [4]-[1] are 7 and 208, respectively. Similarly, the frequency of [2]-[3] is 780, which is followed by 537 [3]-[4], seven [3]-[1] and 236 [3]-[2] sequences of events. If wall turbulent shear flows should consist of completely chaotic motions, a specific trajectory does not occur with such a high frequency. In the

core region of the flow shown in Fig. 5.5(b), the tendency similar to that in the buffer layer can be noted only except for an increase in the trajectories of [2]-[1]-[2], [2]-[3]-[2], [4]-[1]-[4], and [4]-[3]-[4].

The main reason for the increase of these trajectories is that the well-organized motions such as ejections and sweeps gradually degenerate with increasing distance from the wall, and so the ejection- and sweep-type motions are easily cut off by the interaction-type motions. Therefore, the principal features of the coherent motions are reflected more clearly by the measurements in the buffer layer. In other words, we can extract the coherent motions more reliably and more easily from the result shown in Fig. 5.5(a), which indicates that: (1) possibility of direct coupling of the ejections and the sweeps is very low, and the interactions exist almost always between the ejections and sweeps; (2) the interactions wedge themselves into the ejections or sweeps less frequently than between the ejections and sweeps (or vice versa); and (3) the two interactions (i=1, 3) are rarely coupled with each other.

Furthermore, a set of trajectories moving on any four quadrants of the (u, v)-plane have been also sampled, e.g., [4]-[1]-[2]-[3]. The recognized regularity in the sequence of events is exemplified in Fig. 5.6. The frequencies are included in the figure. The numbers in parentheses represent the relevant percentage. As a matter of course, the frequencies of occurrence are nearly identical with those predicted from the values given in Fig. 5.5. For example, the frequency predicted for the trajectory [4]-[1]-[2]-[1] is $502 \times (367/765)=241$, which is in excellent agreement with an actual value of 236.

From these results, it becomes now evident that the deterministic

regularity exists in the trajectory of individual coherent events and that we can detect and describe the coherent motions objectively. Four distinct patterns are eventually recognized in the sequence of coherent motions as given in Table 5.2.

5.3. Basic Flow-Patterns of Coherent Structures

The finding described in the previous section makes it possible to program a computer to extract and ensemble-average sequence of events, and to delineate the characteristics of the coherent structures. The ensemble-averaged velocity and temperature fluctuations can be established by arranging temporal duration and period of each event in the mean duration and the mean period of the respective motions. This procedure is expressed by the following equation:

$$\langle Q'(\tau)\rangle = \frac{1}{N}\sum_{n=1}^{N} Q'\left(\frac{\Delta T_{i,n}}{\overline{\Delta T_i}}\tau + \tau'_n\right) \qquad (5\text{-}3)$$

where $\langle Q'\rangle$ denotes the conditional average of a quantity $Q'(\tau)$, N is the number of events classified into the ith-quadrant, $\Delta T_{i,n}$ represents the duration of events in the ith-quadrant, and $\overline{\Delta T_i}$ is equal to $(1/N)\sum_{n=1}^{N}\Delta T_{i,n}$. The points τ_n' denote the reference points in time when events in the ith-quadrant begin. Time $\tau=0$ arbitrarily corresponds to the position where all the reference points τ_n' are brought into alignment. Figures 5.7, 5.8 and 5.9 show the conditionally averaged patterns of velocity and temperature fluctuations, $\langle u'\rangle$, $\langle v'\rangle$ and $\langle t'\rangle$, Reynolds shear stress,

$\langle u'v' \rangle$, and turbulent heat fluxes, $\langle u't' \rangle$ and $\langle v't' \rangle$, in the buffer layer adjacent to the heat-transfer surface, in the log-law region and in the core region of the flow, respectively. In each figure, the conditional averages are presented in terms of four basic flow-patterns of coherent structures. The velocity and temperature fluctuations are normalized by the respective r.m.s. values and the time τ on the abscissa is normalized by the centerline velocity $\overline{U}_c$ and the displacement thickness $\delta*$. The quantities $\langle \dot{u}'^2 \rangle$ and $\langle \dot{t}'^2 \rangle$ denote $\langle (\partial u'/\partial \tau)^2 \rangle$ and $\langle (\partial t'/\partial \tau)^2 \rangle$, and correspond to the dissipation rates of velocity and temperature fluctuations, ε and ε_t, which can be obtained using the local isotropy and Taylor's hypothesis as:

$$\varepsilon = 15\nu\overline{(\partial u/\partial x)^2} = 15\nu\overline{(\partial u/\partial \tau)^2}/\overline{U}^2 \qquad (5\text{-}4)$$

$$\varepsilon_t = 3\alpha\overline{(\partial t/\partial x)^2} = 3\alpha\overline{(\partial t/\partial \tau)^2}/\overline{U}^2 \qquad (5\text{-}5)$$

where ν and α are the kinematic viscosity and the thermal diffusivity, respectively. The conditional averages of $\langle \dot{u}'^2 \rangle$ and $\langle \dot{t}'^2 \rangle$ are normalized by the respective appropriate common values so that the magnitude of the two becomes nearly the same through Figs. 5.7-5.9.

From Fig. 5.7, it is obvious that four basic patterns have distinct characteristics from each other in the conditional averages of turbulence quantities and in the relevant transport processes of heat and momentum. The interaction-type motions are very important events providing a phase-information for recognition and classification of organized structures. The prominent characteristics of each pattern are: waveforms of $\langle u' \rangle$ and

$\langle v' \rangle$ related to classified patterns 1 and 3 are bilaterally symmetrical at a midpoint of each waveform; $\langle u' \rangle$ and $\langle v' \rangle$ of patterns 2 and 4 are bilaterally asymmetrical, with a larger $\langle u' \rangle$ amplitude of pattern 2 in the first fourth-quadrant and with a completely opposite trend in pattern 4; almost all net heat transfer occurs during the sweeps and ejections; heat transport becomes greatest when the pattern-4 motions dominate a flow field.

It is also found that the dissipation of both velocity and temperature fluctuations happens mainly during the interaction-type motions associated with a change of flow patterns from the ejections to sweeps. Wallace, Eckelmann & Brodkey (1972) reported, from an observation of the flow-visualization film, that the dissipation rate of turbulent kinematic energy peaked at a boundary between the ejection- and sweep-type motions. The present result proves that the fluid flows shifting from the ejections to sweeps dominate not only the dissipation rate of the velocity fluctuations but also that of the temperature.

In the log-law region (Fig. 5.8) and in the outer region (Fig. 5.9) as well, the time length of every pattern becomes shorter, reflecting a decrease in the mean duration of each event $\overline{\Delta T_i}$ (see Fig. 5.2). The difference between patterns 2 and 4 becomes remarkable in magnitude of turbulent heat and momentum transfer. However, the main characteristics of related conditional averages in the log-law and outer regions are similar to those found in the buffer layer. This provides further support for preciseness of the present sampling method to extract the coherent structures which may exist over a greater part of the pipe section.

Here, the characteristics of the basic flow-patterns are supplemented.

The <u'>-waveform of pattern 4 depicts the typical u-signal patterns of the coherent structures consisting of a gradual deceleration from a local maximum followed by a strong acceleration, which was identified by using the pattern-recognition technique (Wallace, Brodkey & Eckelmann 1977). The <t'>-waveform of pattern 4 has a steep negative gradient when <u'> is under strong acceleration. This might reflect the possible existence of a large-scale temperature-front, noted first by Chen & Blackwelder (1978). The dissipation rates of both velocity and temperature fluctuations have their minima during the ejection-phase, but are not zero even near the points of zero-gradient of <u'> and <t'> patterns. Thus, in the course of ensemble-averaging, the waveforms of <u'> and <t'> have lost their small-scale disturbances irresponsible for the larger-scale coherent motions. Furthermore, high-frequency components contributing to the dissipation should have a universal nature regardless of the flow-patterns, since the waveforms of the dissipation rates change little among four basic flow patterns.

Next, the threshold level H is increased to 0.5 for the recognition of the ejection- and sweep-events so as to get, if any, a property of larger scale organized motions. An example of conditional averages is shown in Fig. 5.10. The total number of detected patterns decreases with increasing H values, but the characteristics of each pattern become more pronounced. As shown in Fig. 5.10, the duration of pattern 4 becomes longer than that for H=0, and the typical features of coherent motions such as a weak deceleration of the flow followed by a period of low velocity and a strong acceleration leading to a period of higher velocity are more emphasized. The magnitude of Reynolds shear stress and turbulent heat

fluxes becomes very large accordingly. It is also evident that, in the immediate neighborhood of the heat transfer surface, the larger scale sweep-type motions contribute more to the production processes of turbulent heat and momentum transfer than the ejections; in particular, $\langle -u't' \rangle$ is generated so as to be quite large in the last fourth-quadrant. Note that, however, important changes are not observed in the essential characteristics of every pattern even though the threshold H has changed. This in turn indicates the adequacy of the present detection algorithm.

5.4. Vortex Structures of Coherent Motions

To better understand the spatial extent and evolution of four distinct flow-patterns, the vortex structures of organized motions have been examined. Temporal variation of velocity vectors obtained from the ensemble-averages of $\langle u' \rangle$ and $\langle v' \rangle$ is transformed into its spatial variation by using Taylor's hypothesis. The velocity vector, $\tilde{w}$, relative to an observer moving at a convection velocity U_v, can be written as:

$$\tilde{w} = \{\langle u' \rangle + (\bar{U} - U_v)\}\, i + \langle v' \rangle j \qquad (5\text{-}6)$$

where $\bar{U}$ is a local mean velocity, and i and j represent the unit vectors in the x and y directions, respectively. The velocity vector-diagram of each flow-pattern is established from a set of vectors calculated from Eq.(5-6), which can visualize the spatial structure of the coherent motions observed from a moving "camera". To verify the reality of the deduced velocity-

vector contours, however, it is necessary to ascertain the fact that the same flow pattern occurs simultaneously at different positions in the y direction, at least over some area. Blackwelder & Kaplan (1976) used ten hot-wires arranged normal to the wall, i.e., a hot-wire rake, to examine the degree of coherence in a turbulent boundary layer. Figure 5.11(a) shows their measurements of instantaneous streamwise velocity fluctuations in the inner region of the flow. As shown in Fig. 5.11(b), the authors too have measured the streamwise velocity fluctuations simultaneously at three different y positions in the wall region. Both figures show that the same flow-pattern really occurs at the same time over a considerable area in the direction normal to the wall.

Furthermore, in order to obtain direct evidence for this fact, the axial and normal velocity fluctuations have been also measured simultaneously. A normal hot-wire was set at $y^+=28.8$ and an X-wire probe consisting of two V-shaped hot-wires (Fig. 2.2(b)) was positioned at $y^+=57.5$ right above the normal hot-wire. The X-probe was used as a detector probe when applying the present detection algorithm. The detection-signal from the X-probe afforded a pattern criterion for conditionally averaging the streamwise velocity fluctuations measured by the normal hot-wire. It should be noted that the convection velocities of the coherent motions have a little irregularity (Blackwelder 1977), so the point at which the correlation coefficient between two streamwise velocities (i.e., measured by the normal hot-wire and by the X-probe) becomes maximum is adopted as the reference point in time for obtaining conditional averages. An example of the results is shown in Fig. 5.12. Apparently, the conditional average of $\langle u' \rangle$ obtained from the normal hot-wire is nearly identical to that detected

with the X-probe, thus indicating the existence of a flow field with the same flow pattern. It was confirmed with three other flow-patterns that the same respective pattern did occur simultaneously at different positions in the wall region.

The vortex structures of each flow pattern in the wall region are depicted in Figs. 5.13(a)-(d), calculated from Eq.(5-6) with the convection velocity of an observer equal to a mean streamwise velocity at $y^+=37.8$. Here, the relative velocity vector $\tilde{u}$ is normalized by the friction velocity u_τ. The fluid motions of each flow pattern appear to be considerably different from those expected from Figs. 5.7 and 5.8. The important differences may be listed as follows. Pattern 1 has a small-scale vortical motion in the immediate neighborhood of the wall. The fluid upstream of this vortex is ejected from the near-wall region as if it were penetrating the sweep-type motion fluid which comes from far upstream at a small angle to the wall. In the case of pattern 2, the small-scale vortical motion observed in pattern 1 increases its scale slightly and the outflowing motion from the wall becomes weaker. The ejection- and sweep-type motions interact violently with each other within a very small region. This is a reason why the velocity dissipation rate has its maximum in this limited region (see Fig. 5.7(b)). The upstream fluid rushes toward the wall at a larger angle to the wall, particularly in the neighborhood of the wall, than that which occurs in pattern 1. Pattern 3 has a large-scale vortical motion at about $y^+=70$, and this vortex is seen to dominate the whole structure of pattern 3. The mode of mutual interference between the ejections and upstream sweeps is similar to that of pattern 2. However, a flow state considerably different from patterns 1 and 2 is seen in the

near-wall region downstream of the vortex. Pattern 4 also has a large-scale vortical motion which is similar to that of pattern 3 and centers around $y^+=70$. The important characteristics of this pattern are: the fluid downstream of the vortex penetrates into the region in immediate proximity to the wall and is ejected outward from the wall as if it were involving the near-wall fluid in its motion (i.e., the fluid staying in the near-wall region is brought outward from the wall by the strong vortical motion); the upstream sweeps in the near-wall region have approach angles to the wall much smaller than those of patterns 2 and 3, and move parallel to the wall; the interference between the sweeps and the ejections occurs over a wider area, and this explains why the peak of $\langle \dot{u}'^2 \rangle$ in pattern 4 lasts longer (Fig. 5.7(d)). As mentioned in Section 5.3, much of the turbulent kinetic energy dissipates when the flow changes from the ejections to the sweeps. It can be seen from Figs. 5.13(a)-(d) that this is due to the fact that the ejections and sweeps, which are usually large-scale motions, interact violently with each other, as if clashing in a very narrow region.

To investigate the structure away from the wall, the vortex motions are presented in Figs. 5.14(a) and (b) on condition that the convection velocity of an observer U_v is set to $0.8\overline{U}_c$. Here, structures of patterns 1 and 4 have been focused on. Pattern 1 has a very large-scale vortical motion centering around $y^+=110$. This vortex cannot be observed in Fig. 5.13(a) in which a small-scale vortex exists near the wall. Such a double vortical structure corresponds well with the model which explains the cyclic process of bursting phenomena (Offen & Kline 1975, see Fig. 5.15). Their model may be rephrased as follows: a small-scale vortex

is formed in the near-wall region when the previous burst has just ended; this vortex is lifted up from the wall and grows gradually while increasing its spatial scale; finally, the grown vortex leads to bursting, and this process is then repeated. Hence, it is more reasonable to regard each of the four basic flow-patterns as an elemental motion which does not represent an independent motion of one another but the stage of development of the coherent structures. Especially pattern 4 can be considered to be the flow in the final stage of the bursting phenomena (i.e., breakup), because very active motions with vigorous ejection are observed in Fig. 5.13(d). In addition, as seen from Fig. 5.14(b), pattern 4 delineates the lower part of a very large-scale transverse vortex downstream of the ejections. This structure corresponds to the transverse vortex motions which appear prior to the ejections found by Praturi & Brodkey (1978) (see Fig. 5.16). Furthermore, it might be possible to identify the vortical motion in each flow-pattern (i.e., Figs. 5.13(a)-(d)) with the tip of such a horseshoe vortex as visualized by Head & Bandyopadhyay (1981). No assertion, however, can be made at present.

Consequently, it is established that each of the four basic flow-patterns of the coherent motions is the principal member of the sequential bursting phenomena. In particular, pattern 4 is a very important flow-pattern which involves vigorous ejections. The scale and scope of conditionally averaged vortical motions also agree quite well with the flow-visualization results of Nychas, Hershey & Brodkey (1973), and the calculated results of LES by Kim & Moin (1986). As mentioned in Section 1.1, Bogard & Tiederman (1986) reported that the uv-quadrant method is most effective for detecting ejection-type motions. The idea of the present

detection-method is the same as the uv-quadrant method in respect to classification of the flow into the four quadrants on the (u, v)-plane. However, the present method differs essentially from the conventional one in regard to high ability, objectivity and reliability of the detection algorithm based on the trajectories of quadrant-sequences. It is also self-evident from the above results that the quantitative structures obtained by the present method are in good agreement with most of the flow-visualization results.

5.5. Higher-Order Moments of Coherent Motions

Good modelling of third-order moments $\overline{u_i u_j u_k}$, $\overline{u_i u_j t}$ and $\overline{u_j t^2}$ is an essential subject to develop a reliable turbulence model (Bradshaw et al. 1981; Launder 1985). There are, however, only a few experimental data for third-order moments because of the difficulty in measuring turbulent shear stress and heat flux fluctuations simultaneously. Thus, in this section, the dynamic characteristics of third-order moments are investigated in connection with the organized motions. To associate the results with the vortex structures shown in Figs. 5.13(a)-(d), typical waveforms of third-order moments at $y^+=37.8$ are presented in Figs. 5.17(a)-(d). The distinct evidence is that much of the production of third-order moments occurs during the ejection-phase of pattern 4, which may well be explained by the vortical motion of pattern 4 shown in Fig. 5.13(d). Regarding the dynamic aspects of $\langle v'^3 \rangle$, the positive skewness can be clearly seen in the ejection-phase of patterns 1 and 4, and the negative skewness is observed

in the sweep-phase of pattern 3. It should be noted that the behaviour of $\langle v'^3 \rangle$ dominates strongly the other third-order moments.

5.6. Relationship Between Coherent Motions and Heat Transport Processes

As the details of elemental flow-patterns for the coherent structures have been understood, next the relation between the coherent structures and heat transport processes is investigated. With the conditional averages of $\langle u' \rangle$ and $\langle v' \rangle$, a velocity vector $\mathbf{u}'$ for coherent motions is given by:

$$\mathbf{u}' = \langle u' \rangle \mathbf{i} + \langle v' \rangle \mathbf{j} \tag{5-7}$$

A relevant turbulent heat-flux vector $\mathbf{q}'$ may be written as:

$$\mathbf{q}' = \langle u't' \rangle \mathbf{i} + \langle v't' \rangle \mathbf{j} \tag{5-8}$$

The turbulent heat-flux vector does not describe the direction of a turbulent motion (e.g., the direction of heat-flux vector for $v'<0$ and $t'<0$ is identical to that for $v'>0$ and $t'>0$), and hence we must refer to the velocity vectors together to examine the dependence of heat transport processes on coherent motions. The diagrams of nondimensional velocity and turbulent heat-flux vectors, $\mathbf{u}$ $(=\mathbf{u}'/u_\tau)$ and $\mathbf{q}$ $(=\mathbf{q}'/u_\tau t_\tau)$, of each flow pattern, are demonstrated in Figs. 5.18(a)-(d) as a function of y^+. Taylor's hypothesis is used for conversion of a temporal pattern-length to its spatial scale in the streamwise direction. The zero mark on the

abscissa is the beginning point where the pattern is detected. The spatial extent of each pattern in x direction is found almost equal throughout the pipe section. In the near-centerline region, the accuracy of pattern recognition decreases due to the effect of the ejections from the opposite wall (Sabot & Comte-Bellot 1976, Hishida & Nagano 1981), and so the vector-diagrams for this region are not included in Fig. 5.18. As was seen in Section 5.4, the difference in fluid vectors among basic flow-patterns is much larger than that deduced from Figs. 5.7-5.9. For example, the ejections of pattern 2 disperse upward, whereas the ejections of pattern 4 concentrate in the outward direction. The sweeps for patterns 1 and 2 concentrate in the wallward direction with small angles to the wall, whereas those for patterns 3 and 4 occur at larger angles to the wall as if fluids were crashing against the wall.

These different characteristics in flow patterns significantly influence the state of turbulent heat transport. In pattern 1, net turbulent heat transfer is small during the ejection-phase and becomes considerably larger during the sweep-phase. In pattern 2, large axial transports $\langle -u't' \rangle$ are observed near the wall during the sweep-phase downstream of the ejections, but away from the wall (say $y^+ > 40$) they become smaller; thus turbulent heat-flux vectors diverge upward. The heat-flux vectors of pattern 2 are not so intermittent in nature. In pattern 3, $\langle -u't' \rangle$ is large during the ejection-phase, and both $\langle -u't' \rangle$ and $\langle v't' \rangle$ are negative during the wallward-interaction phase. In pattern 4, much turbulent heat transport occurs overall. In particular, the magnitude of $\langle v't' \rangle$ during the ejection-phase is far larger than for other patterns, and turbulent heat-flux vectors are very intermittent.

These results should be viewed in the light of the velocity vector diagrams shown in Fig. 5.13 to understand the relationship between the vortex structures and heat transport processes. It is readily evident that the streamwise turbulent heat-flux $\langle -u't' \rangle$ becomes large during the sweeps penetrating into the immediate neighborhood of the wall with small angles to the wall, but becomes smaller during the other sweeps with large angles to the wall (also see Fig. 5.7). The radial turbulent heat-flux $\langle v't' \rangle$ is very large in pattern 4 which involves the strong ejection-type motions (i.e., fluid approaching to the wall being carried outward spontaneously), and the heated fluid near the heat transfer-surface is transported outward largely by this pattern. In pattern 3, on the other hand, such an outward flow as occurs in pattern 4 returns again toward the wall and $\langle v't' \rangle$ becomes negative due to the realization of $t'>0$ and $v'<0$; thus heat transfer is suppressed in this pattern.

5.7. Contributions to Turbulence Quantities in Velocity and Thermal Fields From Coherent Motions

As evidenced previously, the ejection- and sweep-type coherent motions, irrespective of flow patterns, are the primary mechanisms of the production of the turbulent shear stress and heat fluxes. Therefore, it is important to evaluate quantitatively the fractional contributions to turbulent quantities related to heat transfer from these coherent motions.

The contribution to the radial turbulent heat flux $\overline{vt}$ from the ith quadrant motions in the (u, v)-plane may be written as:

$$\frac{\overline{(vt)_i}}{\overline{vt}} = \frac{1}{\overline{vt}} \lim_{T\to\infty} \frac{1}{T} \int_0^T v(\tau)t(\tau)I_i(\tau,H)d\tau \qquad (5\text{-}9)$$

where $I_i(\tau,H)$ is the detection function given by Eq.(5-2). The fractional contributions to $\overline{vt}$ from four distinct types of motion for H=0 are presented in Fig. 5.19 as a function of y^+. The ejection-type outflow of high-enthalpy fluid from regions very near the wall is the main contributor to turbulent heat transfer through a greater part of the pipe section. However, sweeps of low-enthalpy fluid from regions away from the wall are prominent as the wall is approached. This is consistent with the mechanism of Reynolds shear stress production; sweeps are the largest contributors in the immediate neighborhood of the wall, and ejections become predominant further away from the buffer layer (Lu & Willmarth 1973; Hishida & Nagano 1981).

The scales of turbulent motions which contribute mainly to $\overline{vt}$ can be analyzed from Eq.(5-9) by varying a threshold level H, and the results for the characteristic flow regions are shown in Fig. 5.20 as a function of H. Over the entire cross section except for the near-centerline region, the turbulent heat transport induced by large-amplitude turbulent motions for H>1 exclusively occurs during the ejection- and sweep-phase and the contributions of both wallward and outward interactions are negligible. The distributions of $\overline{(vt)_i}$ for i=2, 4 (i=2: ejection, i=4: sweep) are very similar to those of Reynolds shear stress $\overline{(uv)_i}$ (Hishida & Nagano 1981), so one may conclude that amplitudes of turbulent heat flux fluctuations are determined by those of Reynolds shear stress fluctuations. This is consistent with previously identified conditional averages of $\langle -u'v' \rangle$ and

$\langle v't' \rangle$ shown in Figs. 5.7-5.10. The ejections of high-enthalpy fluid originating from the wall regions in any azimuthal direction reach the centerline region, and the classification of fluid motions given in Table 5.1 becomes meaningless due to complex effects of interactive motions. As a result, the contributions to $\overline{vt}$ from the classified flows become equal to one another at the pipe centerline.

The fractional contributions to turbulent kinetic energy $\overline{q^2}$ ($= \overline{u^2} + \overline{v^2} + \overline{w^2}$), and temperature variance $\overline{t^2}$ are computed in a manner similar to the fractional contributions to $\overline{vt}$, and the results for H=0 are presented in Figs. 5.21 and 5.22, respectively. Although the circumferential velocity fluctuation w was not measured simultaneously, we could reasonably estimate the fractional contribution to $\overline{(q^2)_i}/\overline{q^2}$ with $[\overline{(u^2)_i} + \overline{(v^2)_i}]/(\overline{u^2} + \overline{v^2})$, because the relation $\overline{w^2} \simeq (\overline{u^2} + \overline{v^2})/2$ holds as shown in Fig. 4.1. Figures 5.21 and 5.22 show that most of the turbulent kinetic energy and temperature variance are produced by the ejection- and sweep-type motions, and the fractional contributions made by these two coherent motions total about 80 % of the whole. In close proximity to the heat-transfer surface, the sweep-type motions are the largest contributor to the production of turbulent kinetic energy and temperature variance. In the buffer layer where turbulent kinetic energy and temperature variance reach their maximums, the ejections and sweeps equally predominate the production of these turbulent quantities, reflecting the highly organized structure composed of the sequence of ejection- and sweep-type coherent motions. At the pipe centerline, the relation $\overline{(q^2)_i}/\overline{q^2} = \overline{(t^2)_i}/\overline{t^2} = 0.25$ holds, and the distinct coherent structures observed in the wall region almost disappear.

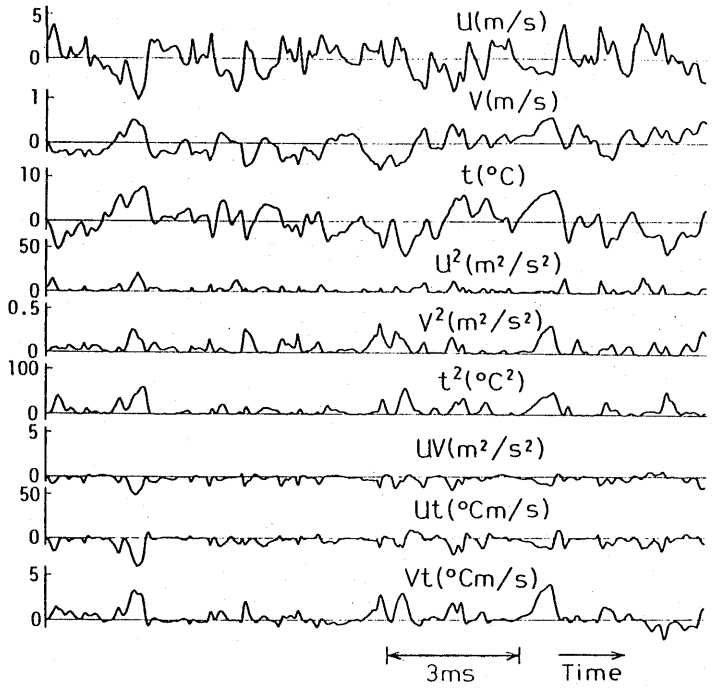

(a)

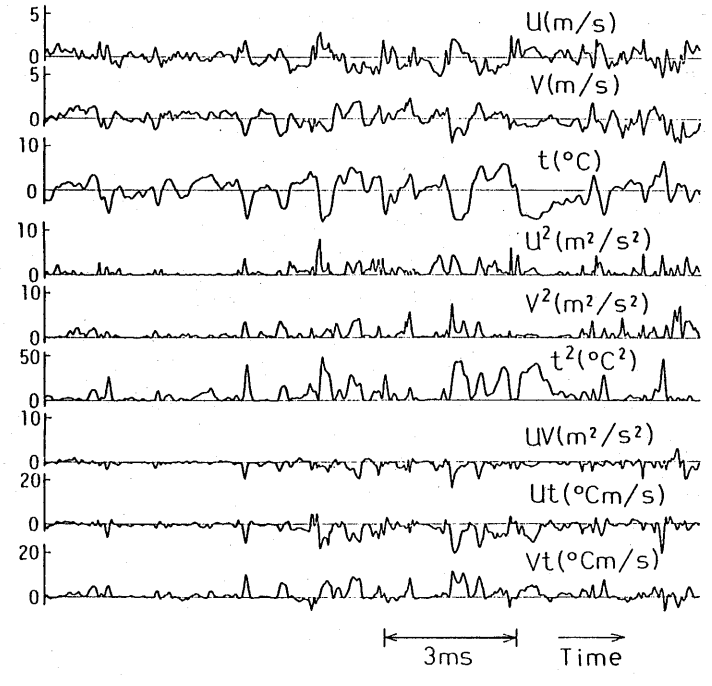

(b)

Fig. 5.1. Simultaneous traces of turbulent quantities related to heat and momentum transfer.

(a) Buffer layer: $y^+ = 10.4$, $y/r_o = 0.012$;

(b) Outer region: $y^+ = 387.7$, $y/r_o = 0.441$.

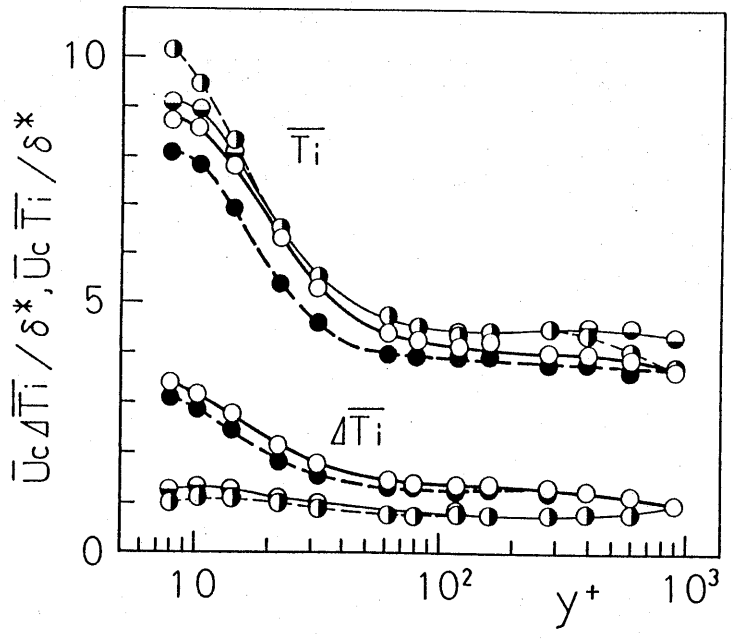

Fig. 5.2. Mean period between events $\overline{Ti}$ and duration of the respective motions $\overline{\Delta Ti}$.

—◑—, i=1, outward interaction; —○—, i=2, ejection;
—◒—, i=3, wallward interaction; —●—, i=4, sweep.

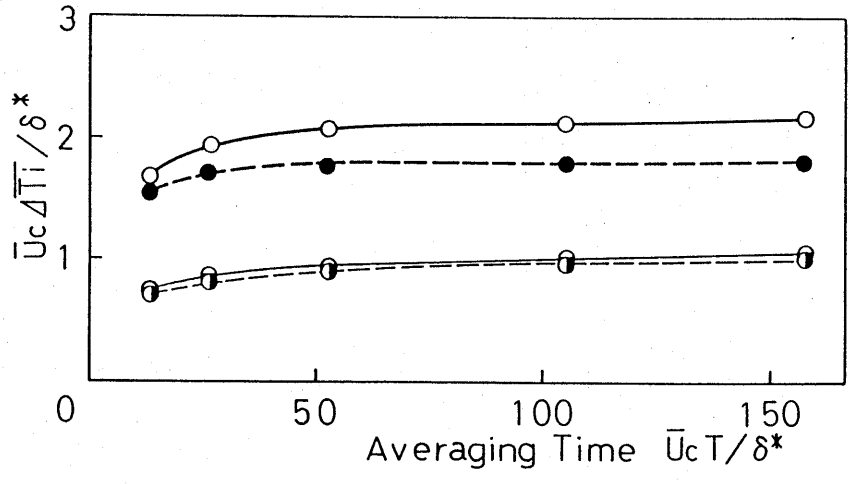

Fig. 5.3. Dependence of mean duration with averaging time T (y^+=22.2). Notation as in figure 5.2.

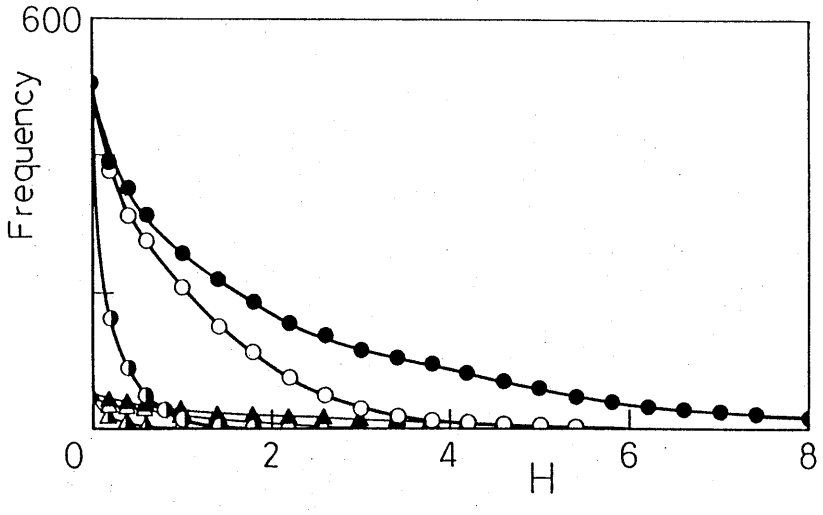

Fig. 5.4. An example of frequencies of occurrence for specific trajectories (y^+=7.6). [●]-[◑]-[○], [4]-[1]-[2]; [▲]-[△]-[◮], [4]-[2]-[1].

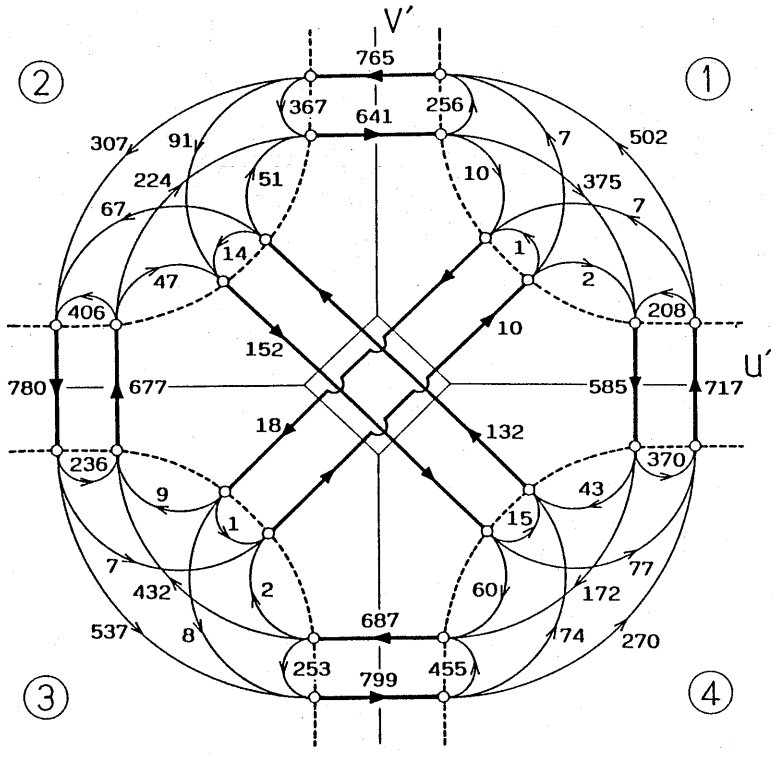

(a)

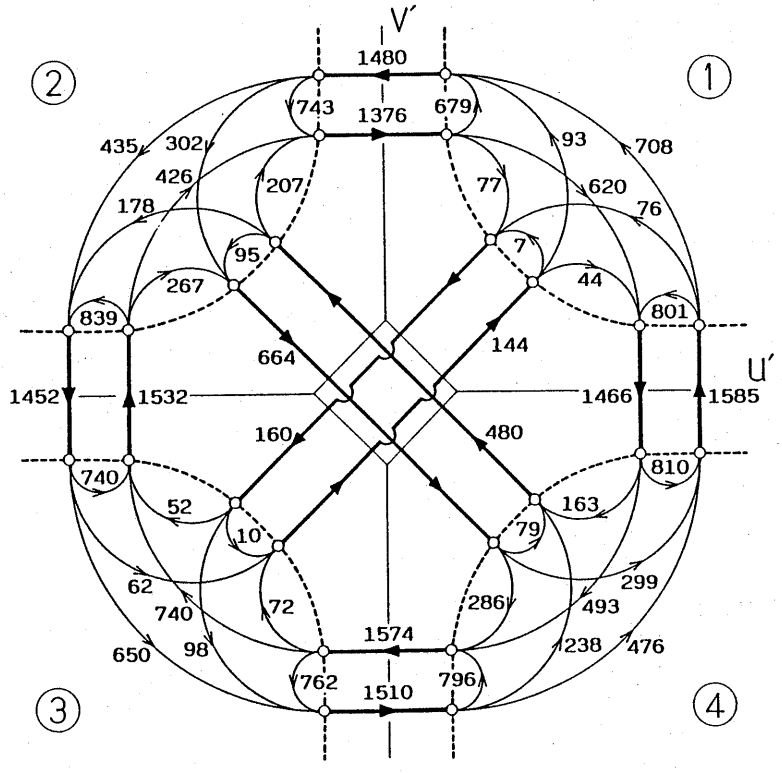

(b)

Fig. 5.5. All possible trajectories on the (u, v)-plane.
(a) Buffer layer, $y^+=7.6$; (b) Core region, $y^+=377.8$.

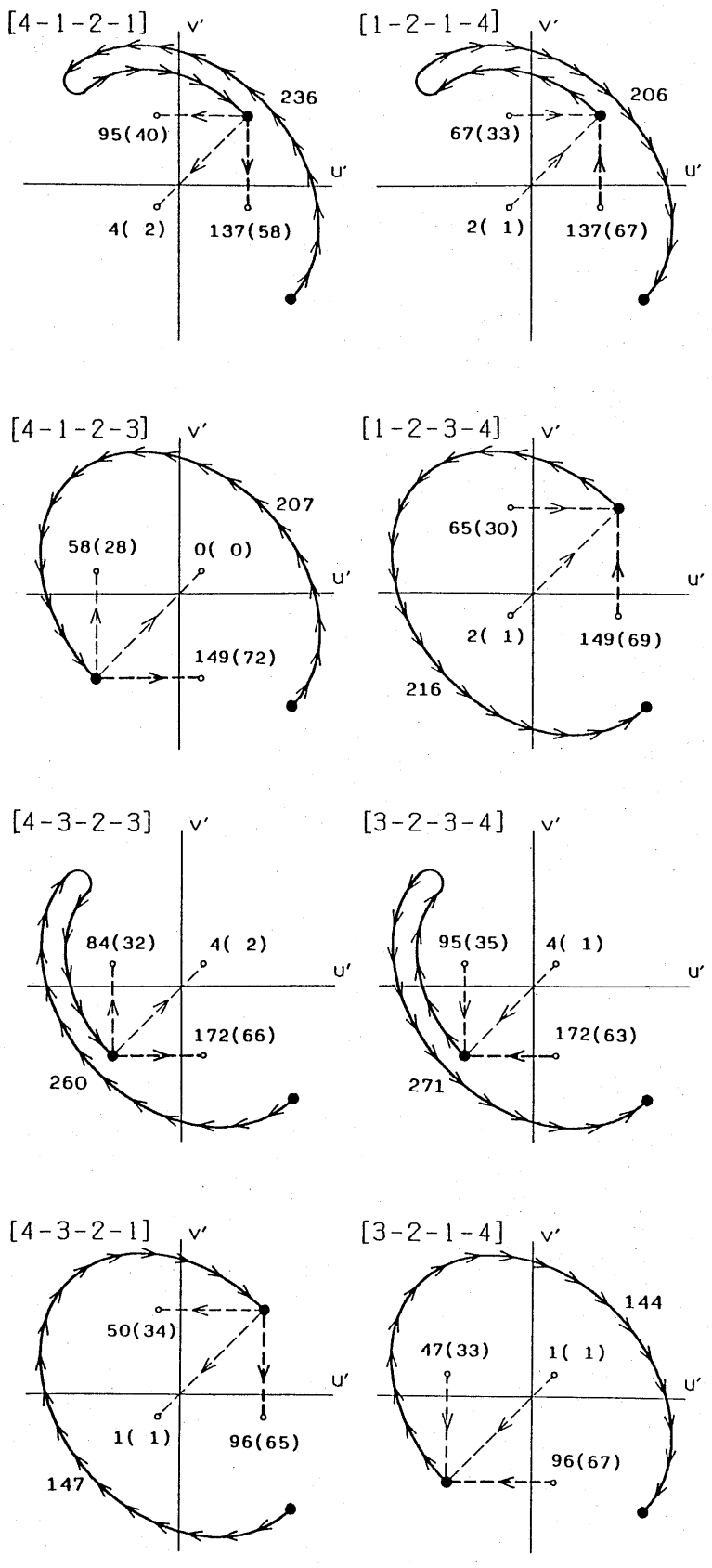

Fig. 5.6. Important trajectories moving on any four quadrants of the (u, v)-plane (y^+=7.6). The numbers in parentheses represent the relevant percentage.

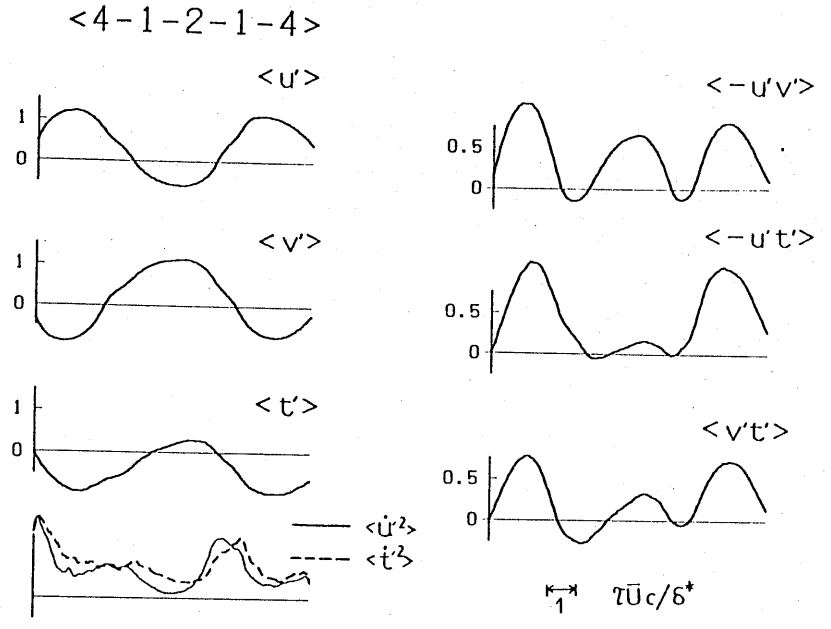

(a)

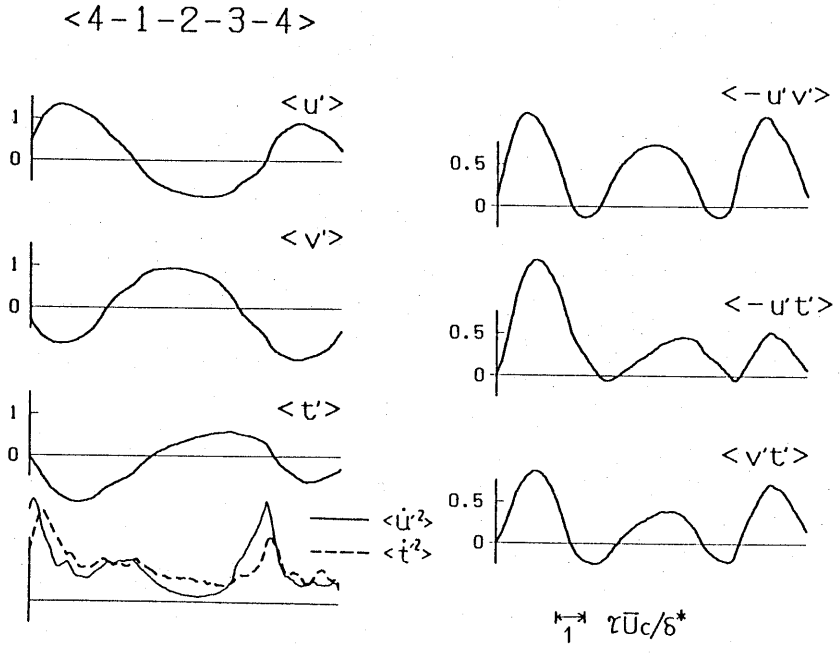

(b)

Fig. 5.7. Basic flow-patterns of coherent motions in the near-wall region (y^+=7.6).

(a) Pattern 1; (b) Pattern 2; (c) Pattern 3; (d) Pattern 4.

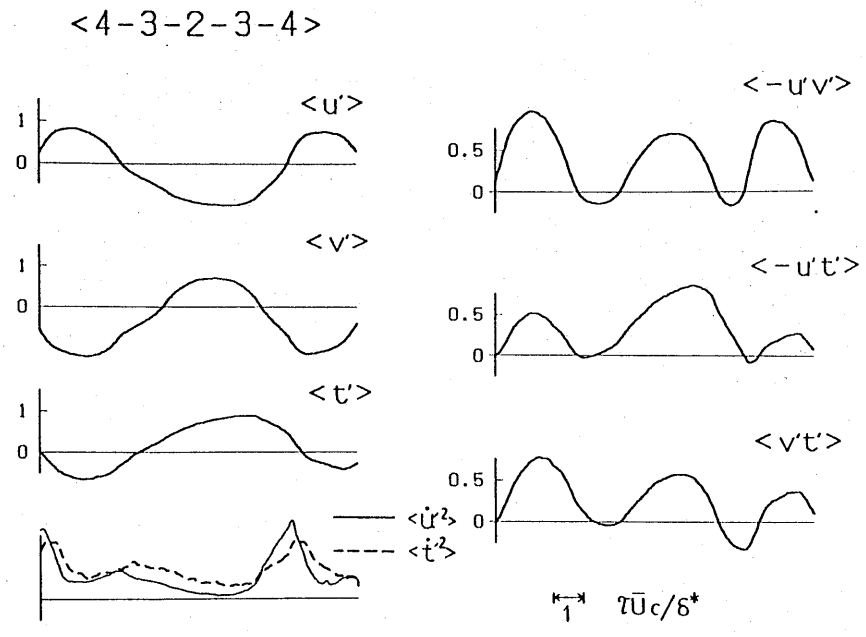

(c)

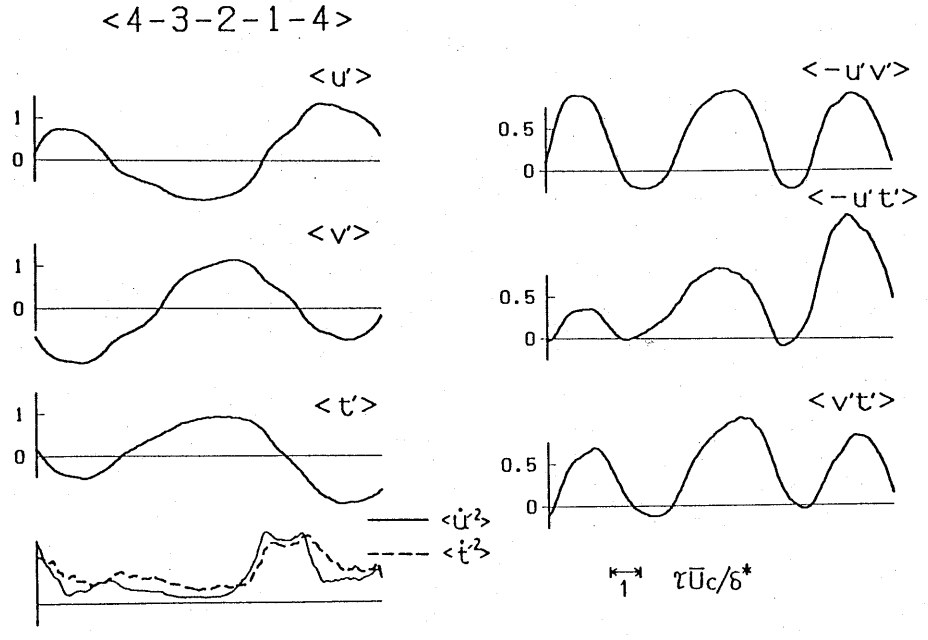

(d)

Fig. 5.7. Basic flow-patterns of coherent motions in the near-wall region ($y^+=7.6$).

(a) Pattern 1; (b) Pattern 2; (c) Pattern 3; (d) Pattern 4.

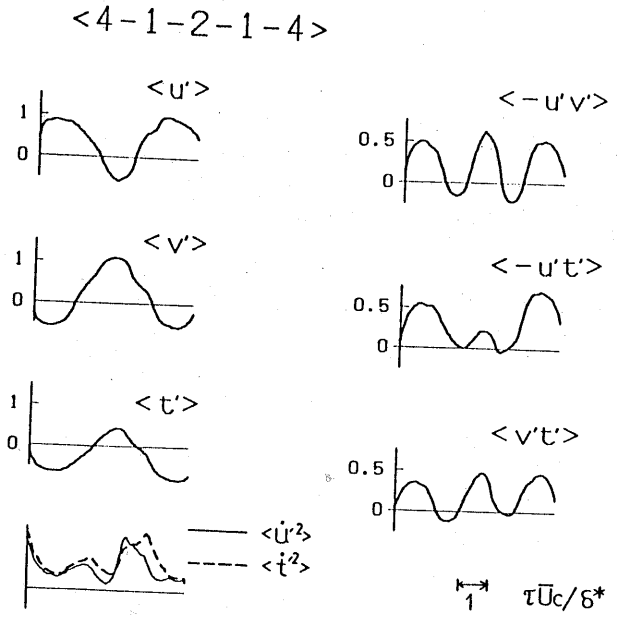

(a)

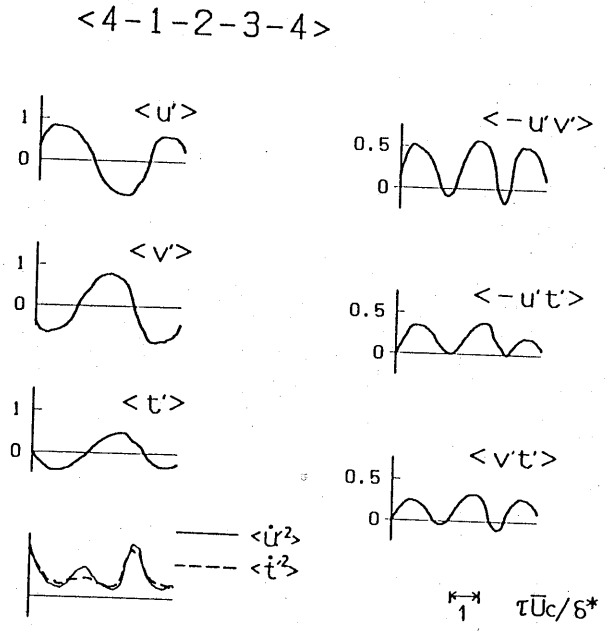

(b)

Fig. 5.8. Basic flow-patterns of coherent motions in the log-law region (y^+=37.8).

(a) Pattern 1; (b) Pattern 2; (c) Pattern 3; (d) Pattern 4.

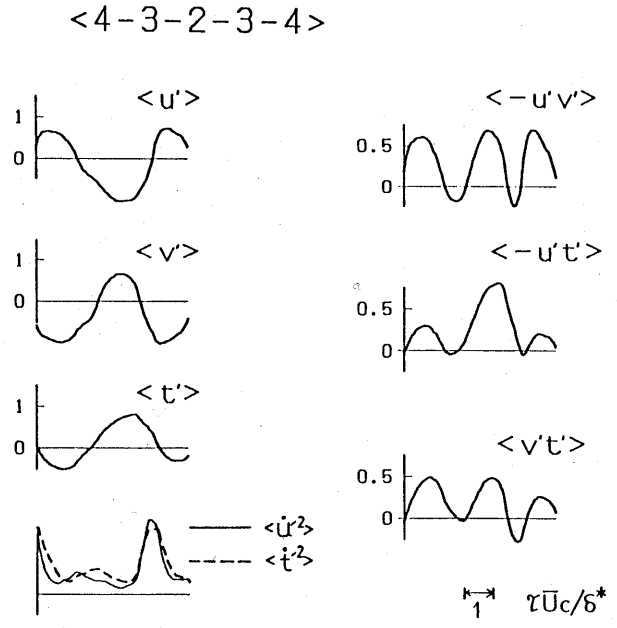

(c)

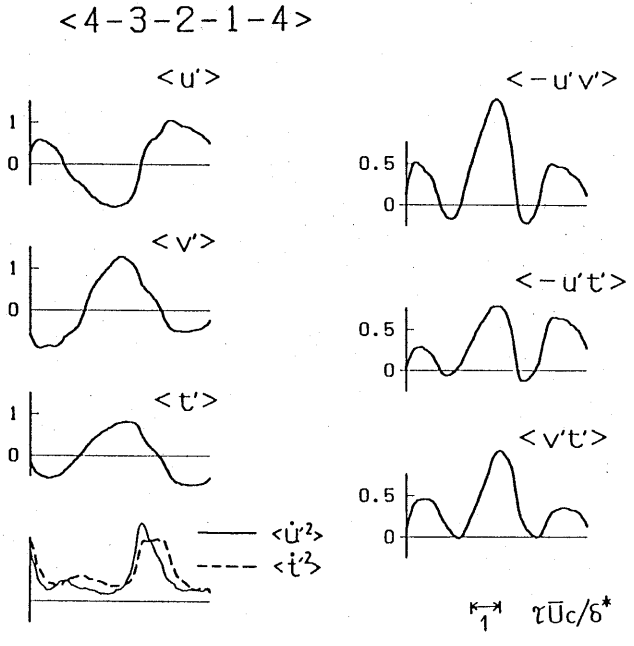

(d)

Fig. 5.8. Basic flow-patterns of coherent motions in the log-law region (y^+=37.8).

(a) Pattern 1; (b) Pattern 2; (c) Pattern 3; (d) Pattern 4.

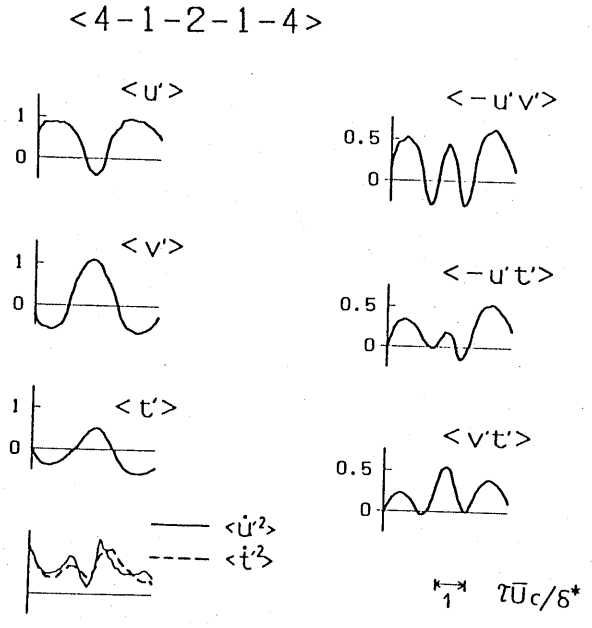

(a)

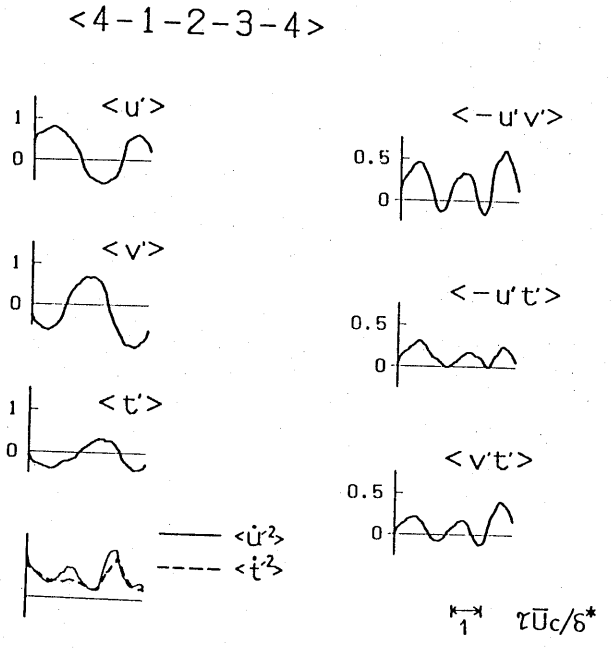

(b)

Fig. 5.9. Basic flow-patterns of coherent motions in the core region (y^+=377.8).

(a) Pattern 1; (b) Pattern 2; (c) Pattern 3; (d) Pattern 4.

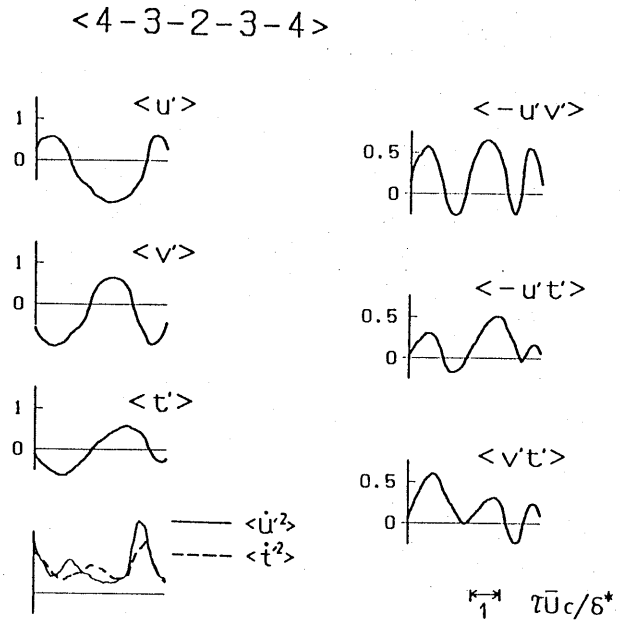

(c)

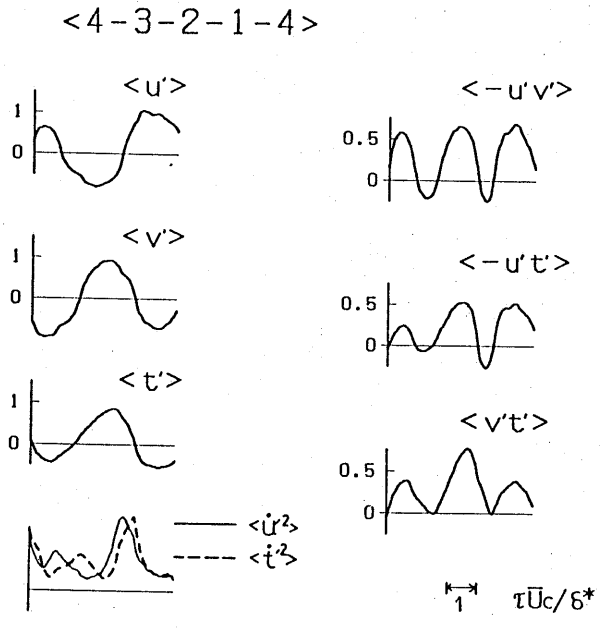

(d)

Fig. 5.9. Basic flow-patterns of coherent motions in the core region (y^+=377.8).

(a) Pattern 1; (b) Pattern 2; (c) Pattern 3; (d) Pattern 4.

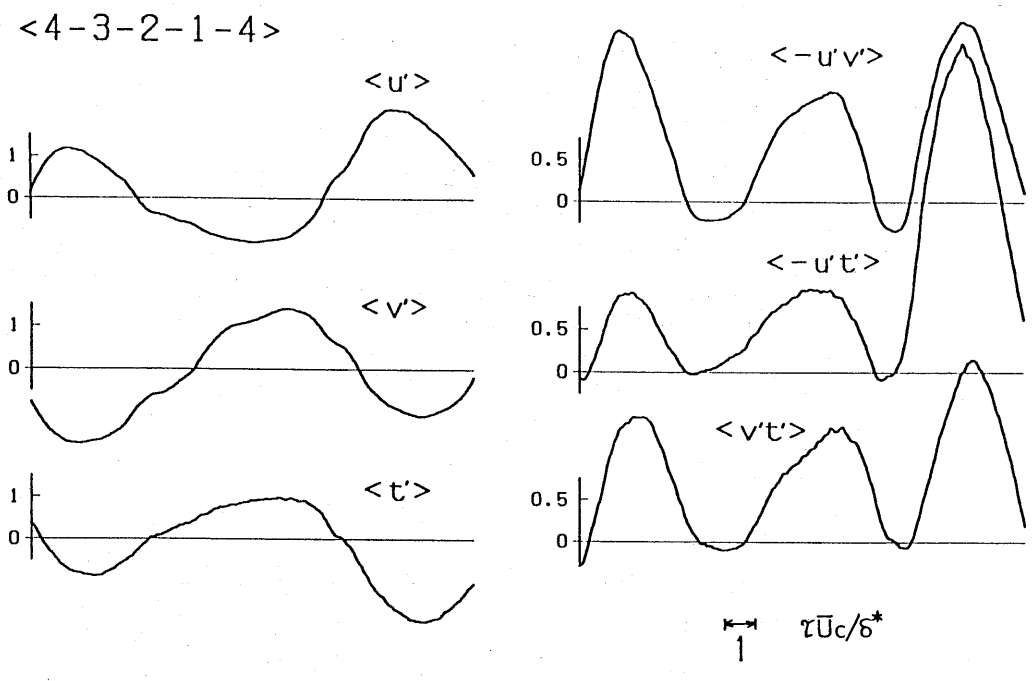

Fig. 5.10. An example of large-amplitude coherent motions (pattern 4, $y^+=7.6$, H=0.5).

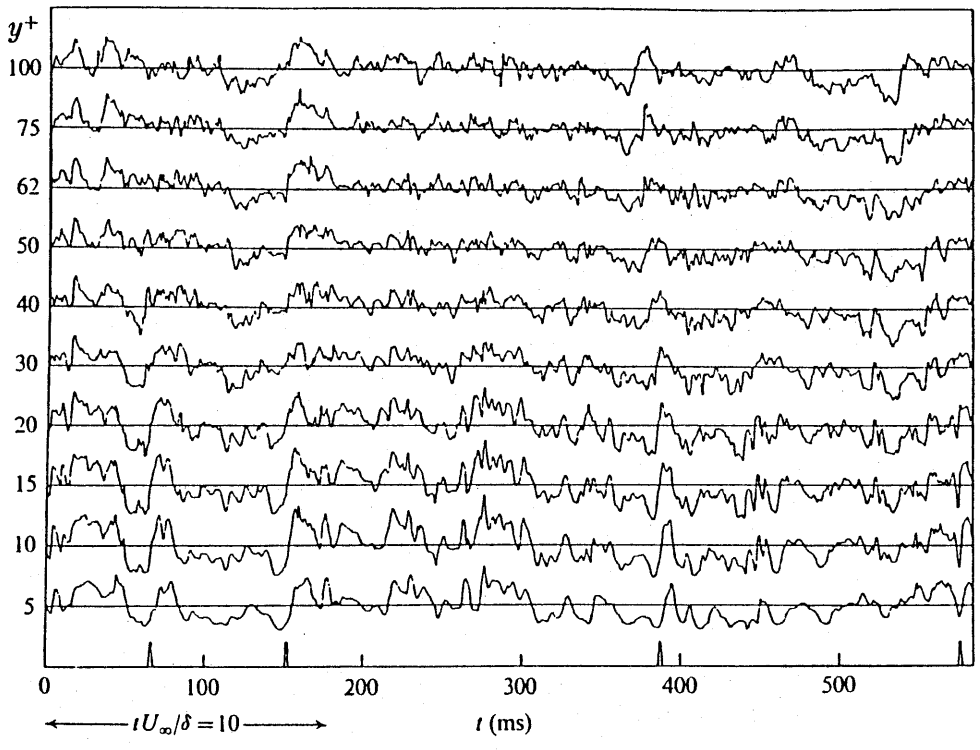

(a)

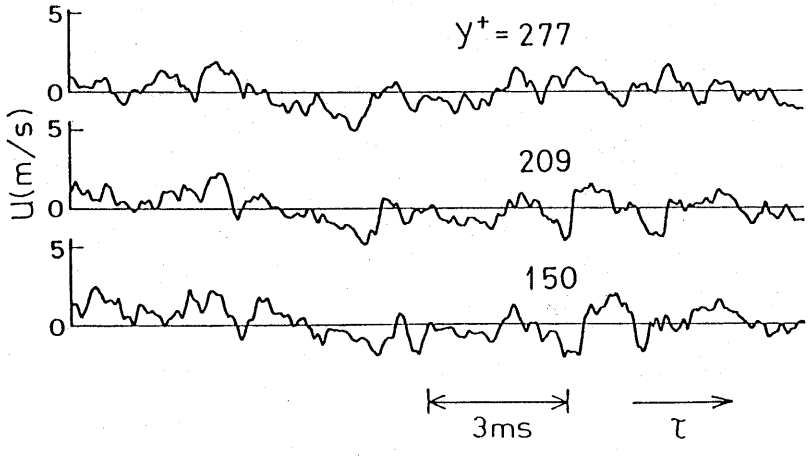

(b)

Fig. 5.11. Evidences of a high degree of coherence of velocity fluctuations in the wall region.

(a) Near-wall region (from Blackwelder & Kaplan 1976; figure 7);

(b) Fully turbulent region.

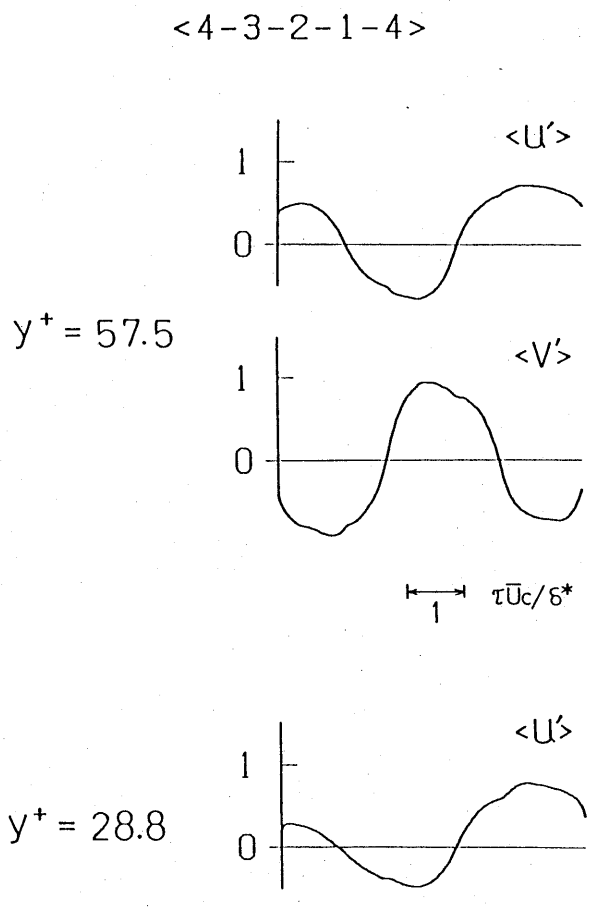

Fig. 5.12. A sample result showing the simultaneous occurrence of identical flow-pattern at two different y positions (pattern 4).

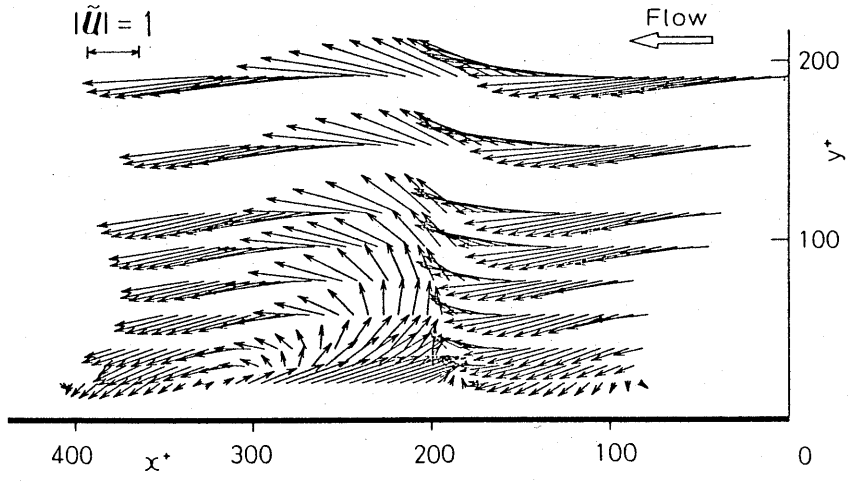

(a)

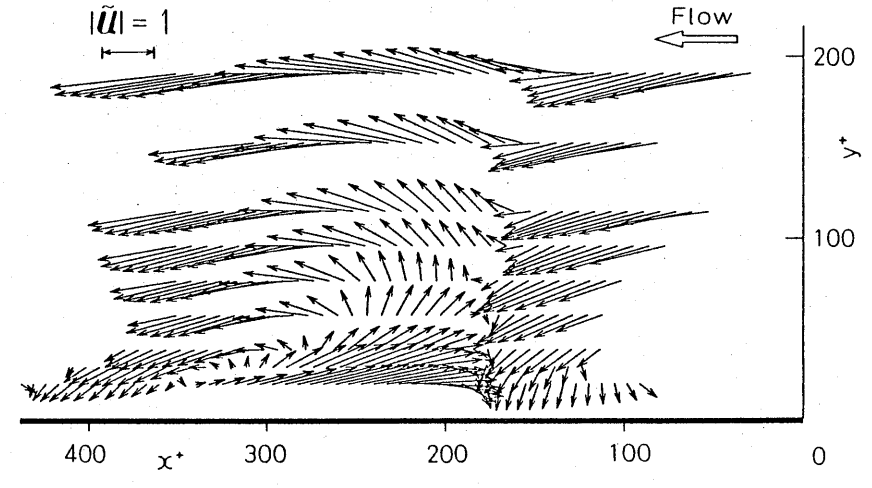

(b)

Fig. 5.13. Vortex structures of basic flow-patterns that might be seen by an observer moving at a speed $U_V=0.64\bar{U}_c$.
(a) Pattern 1; (b) Pattern 2; (c) Pattern 3; (d) Pattern 4.

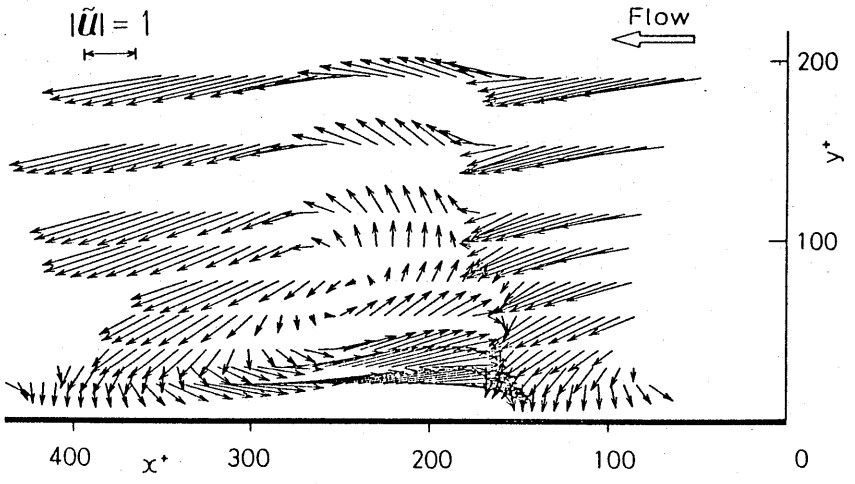

(c)

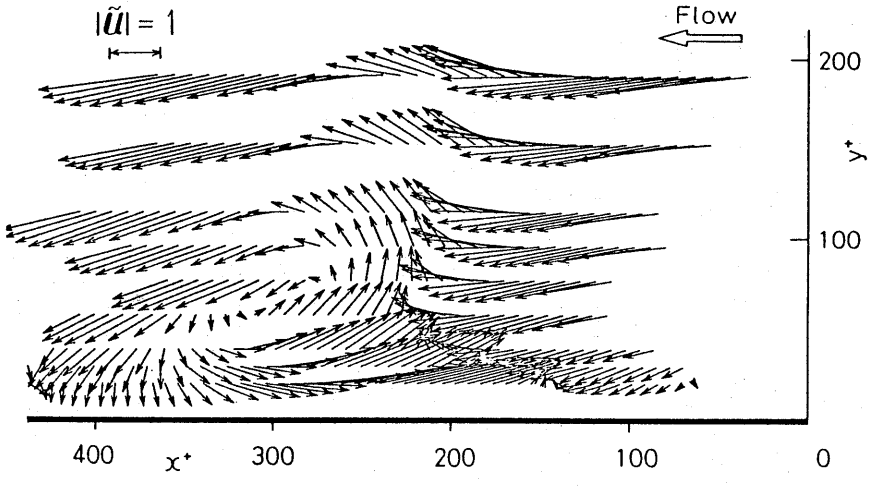

(d)

Fig. 5.13. Vortex structures of basic flow-patterns that might be seen by an observer moving at a speed $U_v=0.64\bar{U}_c$.
(a) Pattern 1; (b) Pattern 2; (c) Pattern 3; (d) Pattern 4.

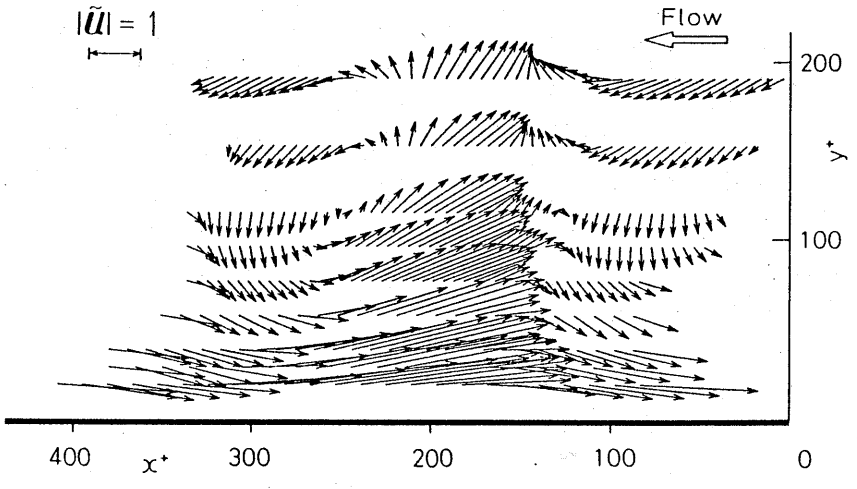

(a)

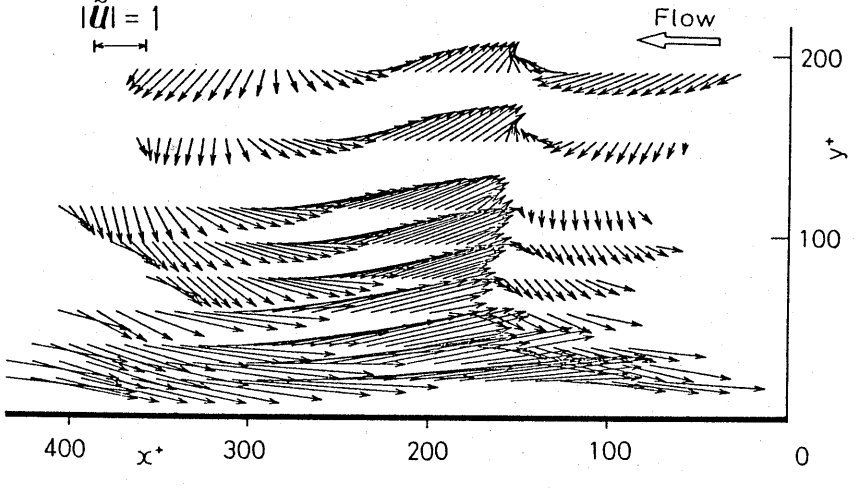

(b)

Fig. 5.14. Vortex structures of basic flow-patterns (U_V=0.8$\bar{U}_c$).
(a) Pattern 1; (b) Pattern 4.

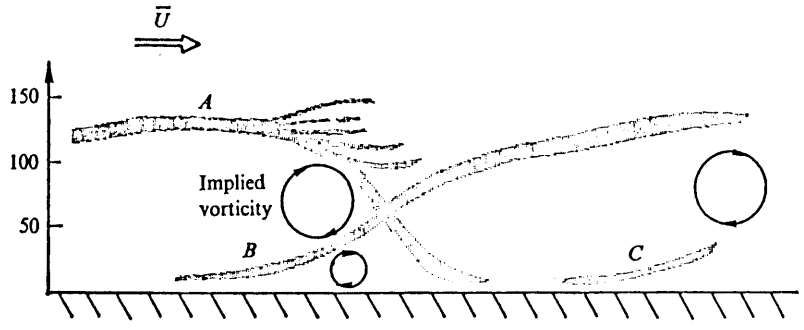

Fig. 5.15. Side view of the interactions between bursting flow modules (from Offen & Kline 1975; figure 1(a)).

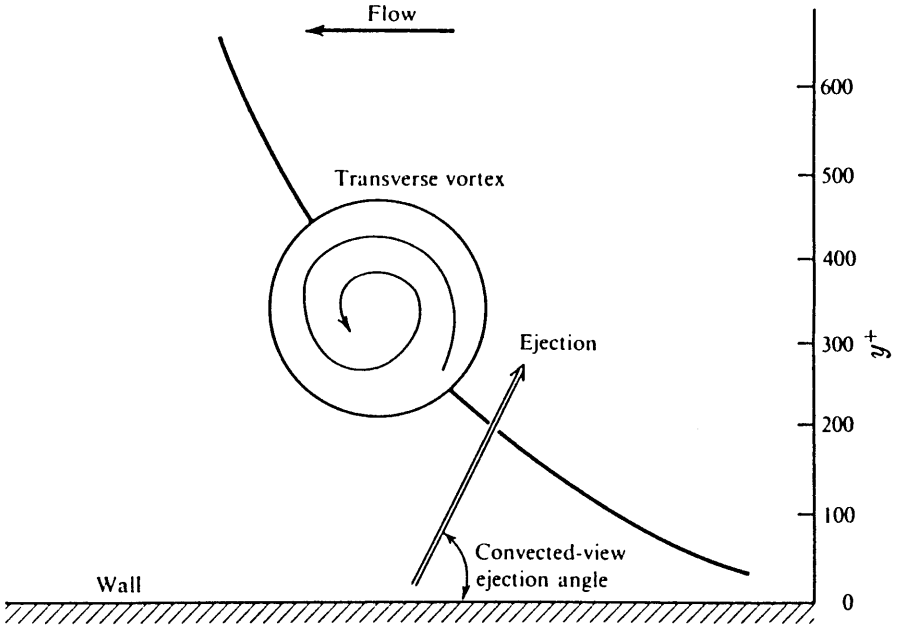

Fig. 5.16. Typical ejection event (from Praturi & Brodkey 1978; figure 8).

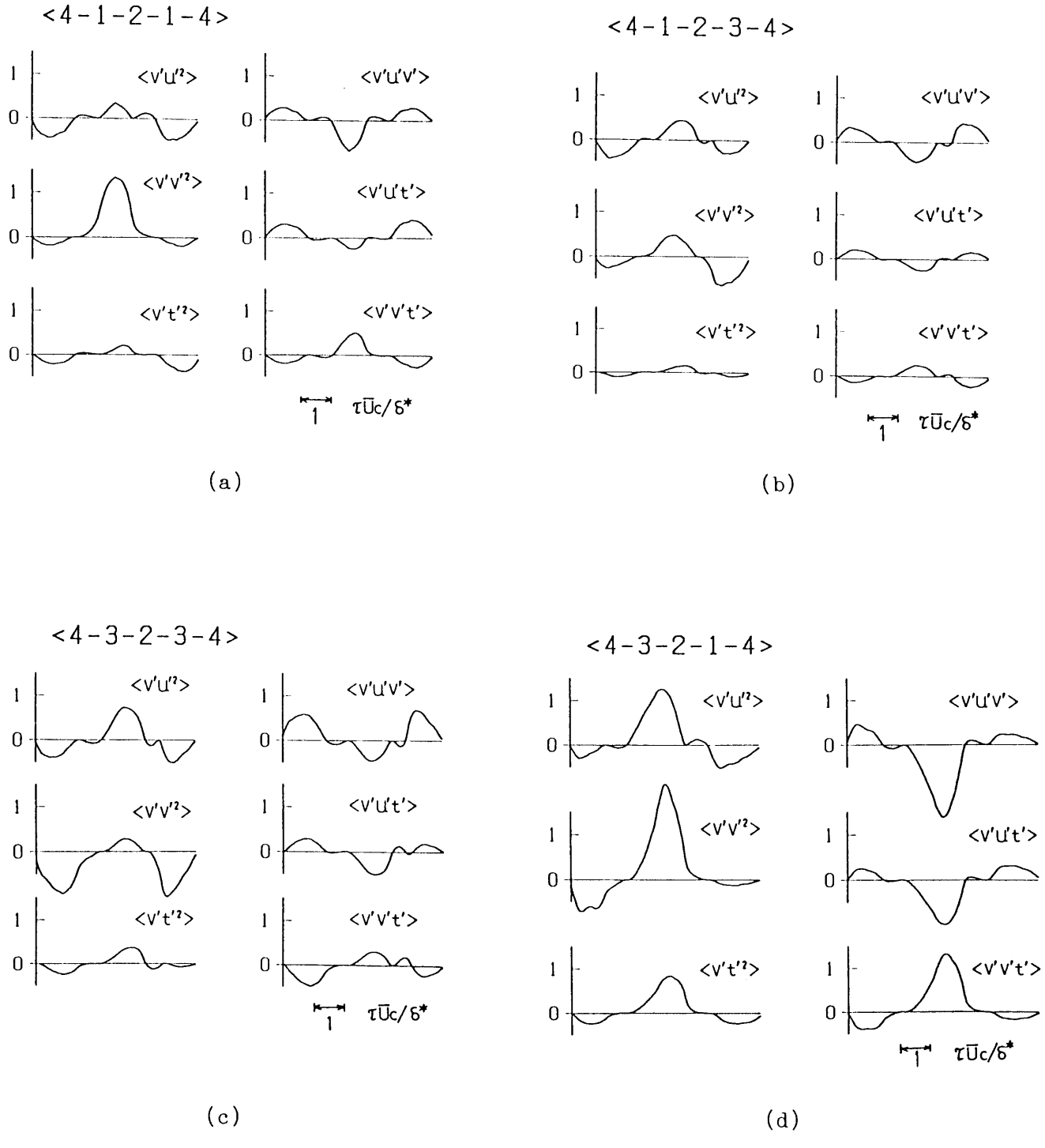

Fig. 5.17. Conditionally averaged patterns of higher-order moments associated with the coherent motions (y^+=37.8).
(a) Pattern 1; (b) Pattern 2; (c) Pattern 3; (d) Pattern 4.

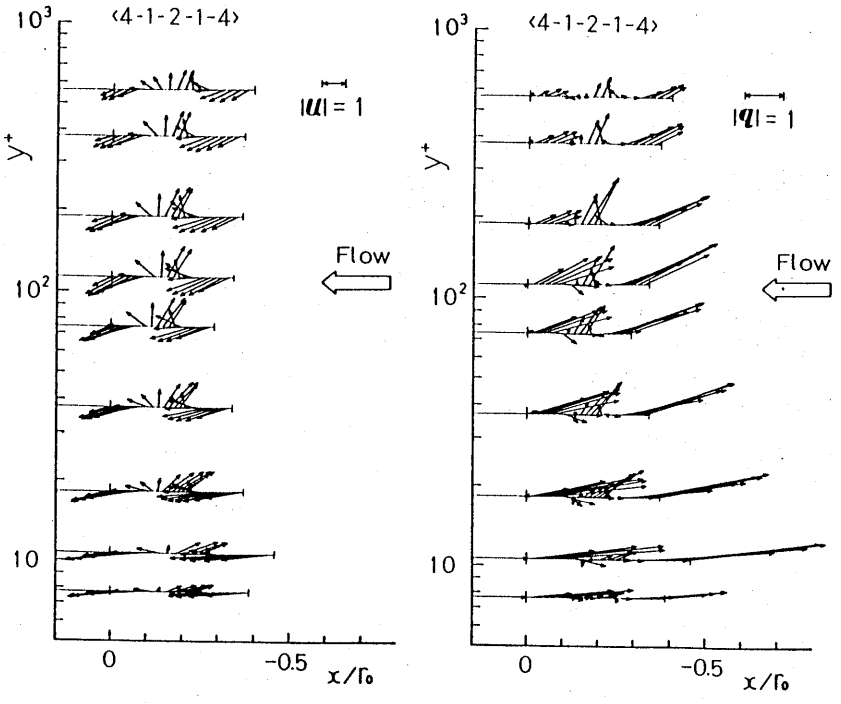

(a)

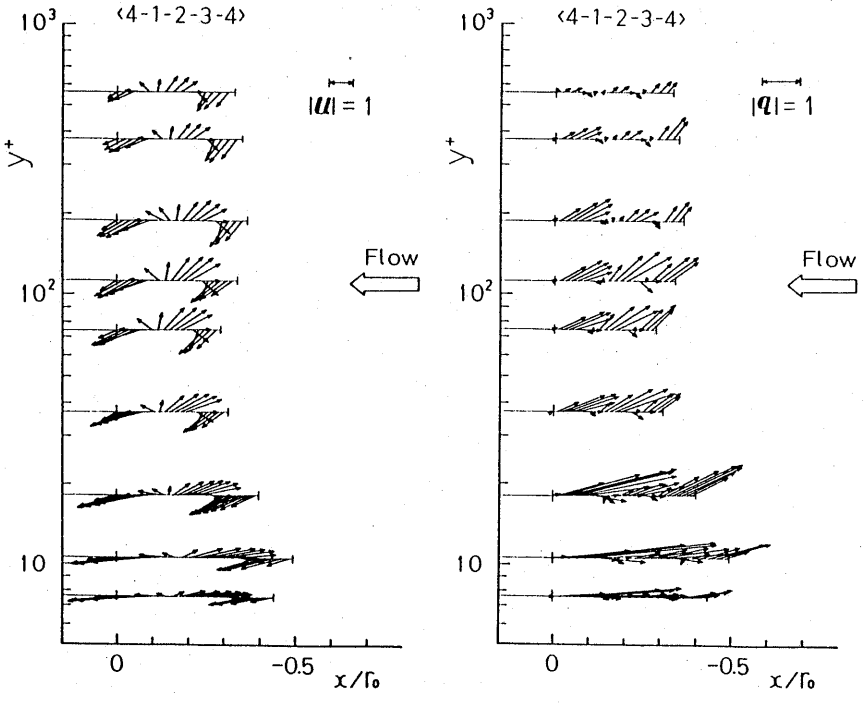

(b)

Fig. 5.18. Velocity and turbulent heat-flux vectors for the basic flow-patterns (normalized by u_τ and t_τ).
(a) Pattern 1; (b) Pattern 2; (c) Pattern 3; (d) Pattern 4.

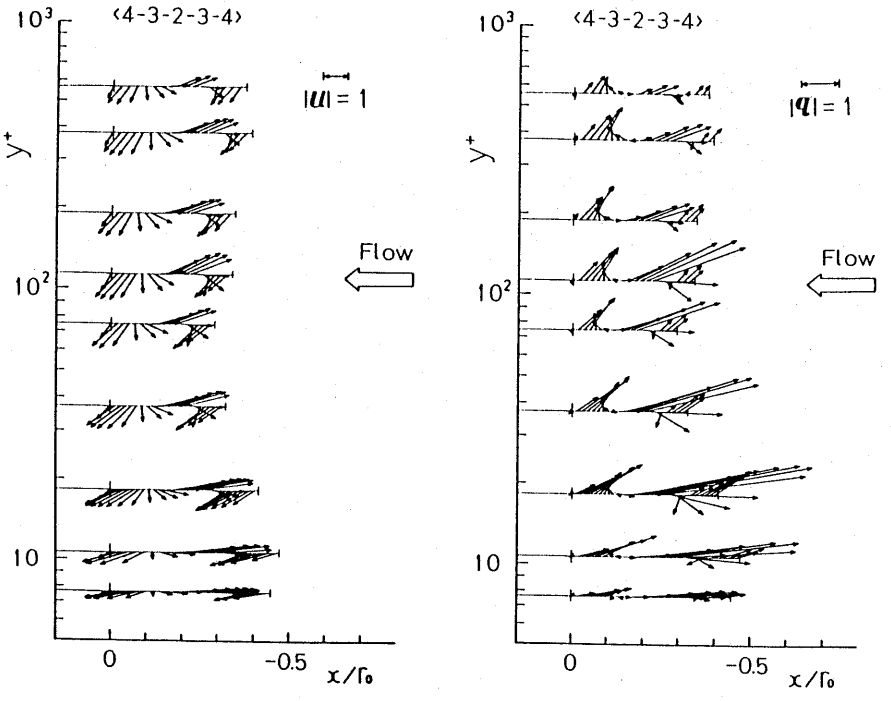

(c)

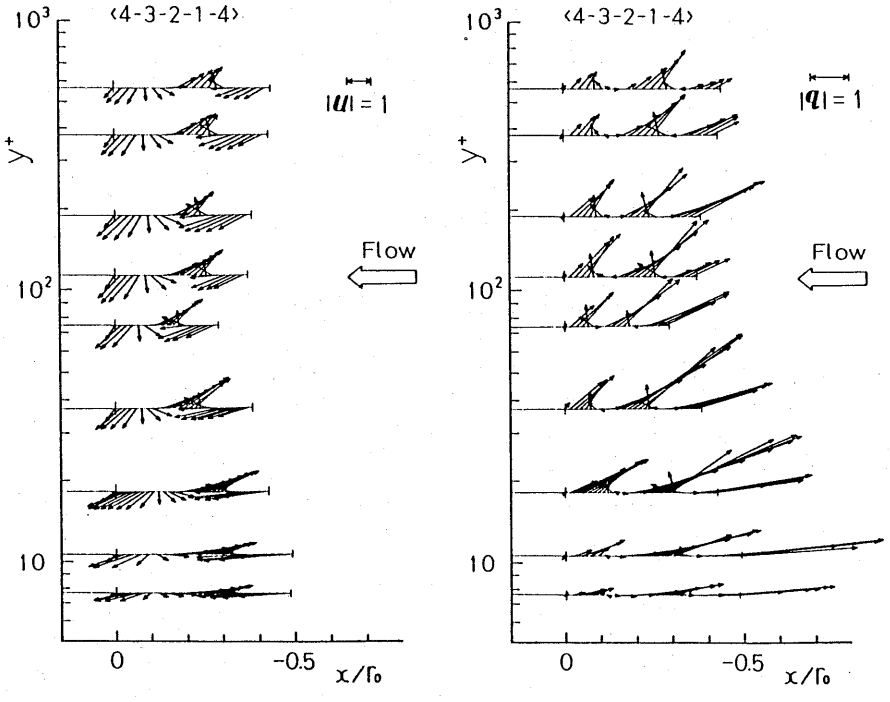

(d)

Fig. 5.18. Velocity and turbulent heat-flux vectors for the basic flow-patterns (normalized by u_τ and t_τ).
(a) Pattern 1; (b) Pattern 2; (c) Pattern 3; (d) Pattern 4.

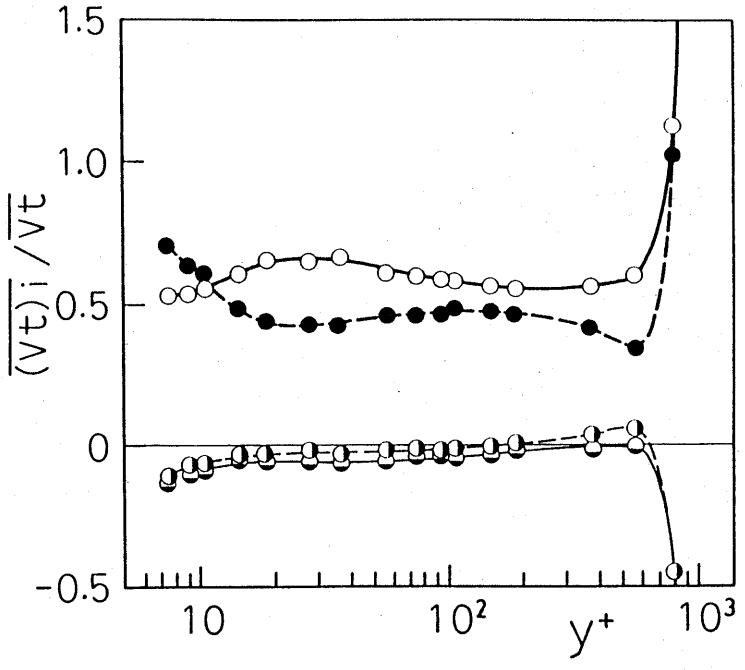

Fig. 5.19. Fractional contributions to turbulent heat-flux $\overline{vt}$ from different motions with H=0. Notation as in figure 5.2.

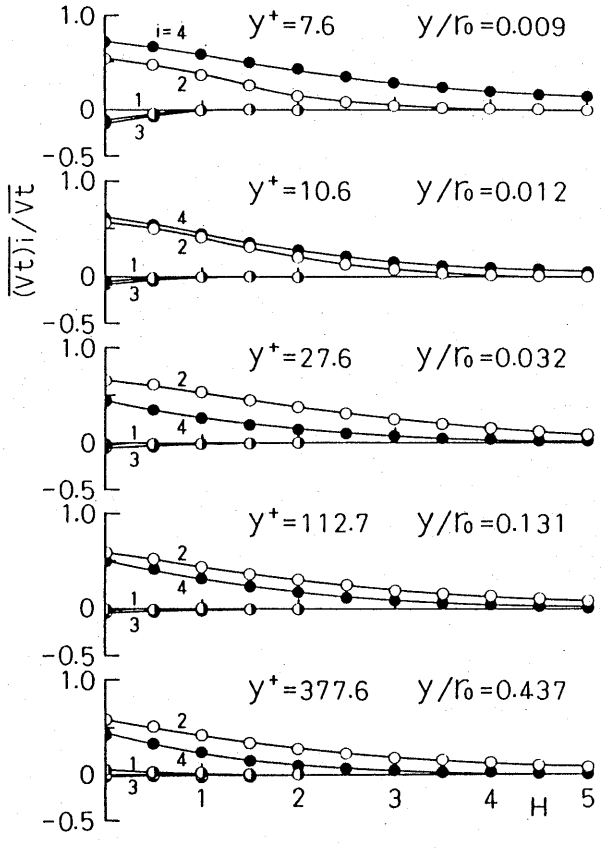

Fig. 5.20. Fractional contributions to $\overline{vt}$ from different motions as a function of H. Notation as in figure 5.2.

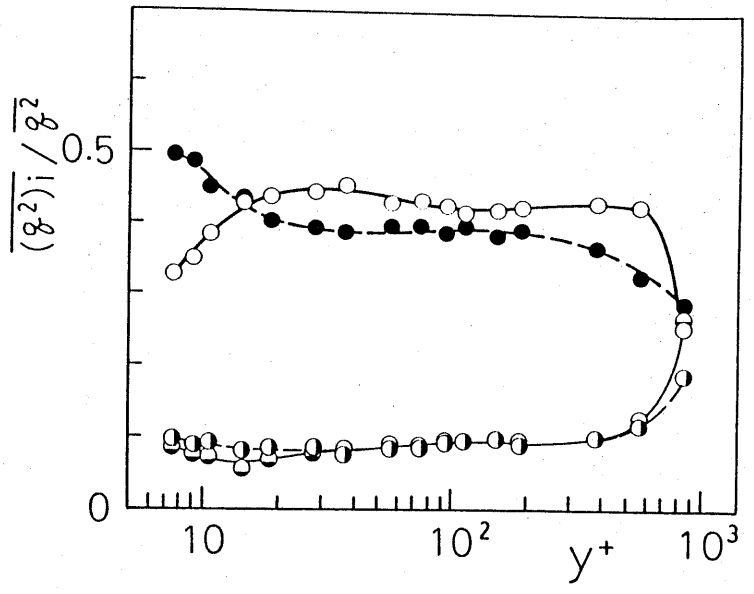

Fig. 5.21. Fractional contributions to turbulent kinetic energy $\overline{q^2}$ from different motions. Notation as in figure 5.2.

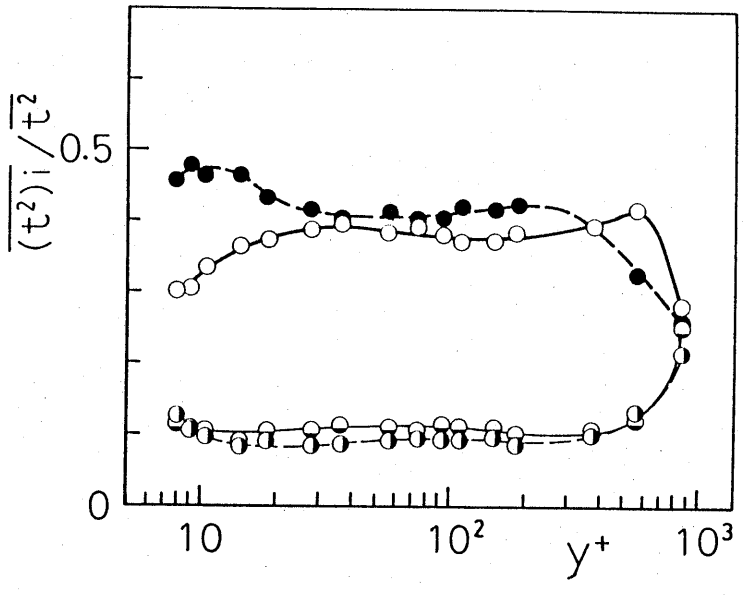

Fig. 5.22. Fractional contributions to temperature variance $\overline{t^2}$ from different motions. Notation as in figure 5.2.

Quadrant (u-v plane)		Type of Motion	Contribution to $-\overline{uv}$
1	u>0, v>0	Outward Interaction	−
2	u<0, v>0	Ejection	+
3	u<0, v<0	Wallward Interaction	−
4	u>0, v<0	Sweep	+

Table 5.1. Classification of the various types of motions in the (u, v)-plane.

Pattern	Quadrant Sequence
1	[4]-[1]-[2]-[1]-[4]
2	[4]-[1]-[2]-[3]-[4]
3	[4]-[3]-[2]-[3]-[4]
4	[4]-[3]-[2]-[1]-[4]

Table 5.2. Four basic flow-patterns of the coherent motions.

CHAPTER VI

FINE STRUCTURES OF COHERENT TURBULENT TRANSPORT PROCESS

6.1. Conditional Probability Density Distributions of Velocity and Temperature Fluctuations

Using the generalized three-dimensional joint pdf developed in Chapter III, we can obtain the following one-dimensional conditional pdf $P_i(\chi)$ in terms of the flow-classification given in Table 5.1:

$$
\begin{aligned}
P_i(\hat{u}) &= \int_0^{\infty} \{ \int_{-\infty}^{\infty} P(\hat{u}, \sigma_{v,i}\hat{v}, \hat{t}) d\hat{t} \} d\hat{v} \\
P_i(\hat{v}) &= \int_0^{\infty} \{ \int_{-\infty}^{\infty} P(\sigma_{u,i}\hat{u}, \hat{v}, \hat{t}) d\hat{t} \} d\hat{u} \\
P_i(\hat{t}) &= \int\int_0^{\infty} P(\sigma_{u,i}\hat{u}, \sigma_{v,i}\hat{v}, \hat{t}) d\hat{u} d\hat{v}
\end{aligned}
\qquad (6\text{-}1)
$$

where

$$
\sigma_{u,i} = (1,-1,-1,1), \quad \sigma_{v,i} = (1,1,-1,-1) \qquad (6\text{-}2)
$$

Here, the suffix i denotes each quadrant in the (u, v)-plane, and $\sigma_{u,i}$ and $\sigma_{v,i}$ are sign-functions which represent the signs of u and v of the ith-quadrant. For example, in the case of i=2, we have:

$$
(\sigma_{u,i},\ \sigma_{v,i}) = (-1,\ 1).
$$

The experimental results of $P_i(\chi)$ are shown in Fig. 6.1, compared with the calculated values from Eq.(6-1). The most probable value of the conditional pdf of temperature fluctuations exists in the region t>0 at an ejection-phase (i=2) and in the region t<0 at a sweep-phase (i=4). This result provides statistical support for the evidence that low-momentum and high-enthalpy fluid moves away from the wall during the ejection-phase and, inversely, high-momentum and low-enthalpy fluid moves toward the wall during the sweep-phase. On the other hand, the conditional pdf $P_i(\hat{t})$ related to both interaction-phases (i=1, 3) are almost symmetrical; that is, the temperature fluctuations do not correlate to the interactive fluid motions.

Predictions from Eq.(6-1) are seen in excellent agreement with the experimental values. Thus, we can apply the joint pdf $P(\hat{u},\hat{v},\hat{t})$ to the analysis of the coherent turbulent structures and the relevant transport processes of momentum and heat.

6.2. Contributions of Organized Fluid Motions to Second-Order Moments

6.2.1. Contributions of different motions to turbulent momentum and heat transfer

Figures 6.2 and 6.3 show the results of the fractional contributions to the time-averaged values of Reynolds shear stress $\overline{uv}$ and turbulent heat flux $\overline{vt}$ from each fluid motion classified in the (u, v)-plane, respectively. The contributions from ejections become the largest in the

region $y^+>10$, while sweeps predominate in the near-wall region ($y^+<10$). These features are equally seen in contributions to both $\overline{uv}$ and $\overline{vt}$. Lines in Figs. 6.2 and 6.3 represent the theoretical predictions from the following equation, which is obtained by calculating the moment $\overline{u^\ell v^m t^n}$ separately in each quadrant of the (u, v)-plane with Eq.(3-12).

$$\overline{(\hat{u}^\ell \hat{v}^m \hat{t}^n)}_{i,H} = \sigma_{u,i}^\ell \sigma_{v,i}^m \int_0^\infty \left[\int_{H/\hat{u}}^\infty \left\{\int_{-\infty}^\infty \hat{u}^\ell \hat{v}^m \hat{t}^n P(\sigma_{u,i}\hat{u}, \sigma_{v,i}\hat{v}, \hat{t})d\hat{t}\right\}d\hat{v}\right]d\hat{u}$$

$$= \frac{2}{(2\pi)^{3/2}} \sum_{\substack{p,q,r=0 \\ n+r=\text{even}}}^{K\leqq 4} \sigma_{u,i}^{\ell+p} \sigma_{v,i}^{m+q} C_{pqr} \int_0^\infty b_{\ell,p}(\hat{u})\left\{\int_{H/\hat{u}}^\infty b_{m,q}(\hat{v})d\hat{v}\right\}d\hat{u} \cdot B_{n,r} \qquad (6\text{-}3)$$

where,

$$b_{j,k}(\chi) = \chi^j H_k(\chi) \exp(-\chi^2/2), \quad B_{j,k} = \int_0^\infty b_{j,k}(\chi)d\chi$$

and the parameter H is a threshold so as to pick out phenomena only for $|\hat{u}\hat{v}| > H$. Putting H=0, ℓ=m=1 and n=0 for $\overline{(uv)}_i$, and H=0, m=n=1 and ℓ=0 for $\overline{(vt)}_i$ in Eq.(6-3), we obtain the theoretical values shown in Figs. 6.2 and 6.3, respectively. As seen in these figures, the theoretical predictions can trace the experimental trends satisfactorily. Thus, essential aspects of the coherent structures such as negligible contributions from both interactions and a reversal of contributions in ejections and sweeps at about $y^+=10$, are well reproduced.

The scales of fluid motions which contribute mainly to the turbulent heat transport are presented in Fig. 6.4, being evaluated with a threshold

level H. From this figure, one can recognize that the transport processes of heat are dominated by large-amplitude ejection- and sweep-type coherent motions, and the contributions of both interactions are negligible for H>2. Nakagawa & Nezu (1977) used a two-dimensional pdf for analyzing the structures of Reynolds shear stress $\overline{uv}$ theoretically. However, in order to clarify the structures of turbulent heat fluxes in terms of typical turbulent motions classified in the (u, v)-plane, we need a three-dimensional pdf. Hence, their approach is not applicable for this purpose. Lines in Fig. 6.4 show the predictions from Eq.(6-3) for various threshold levels. Clearly, Eq.(6-3) is very useful for analyzing the turbulent heat transfer in conjunction with the scales of fluid motions.

6.2.2. Conditional probability density distribution of heat flux vt

As stated previously, turbulent heat flux vt is determined by large-amplitude organized motions (ejections and sweeps). To gain a deeper insight into this distinct feature, the conditional pdf of $\hat{v}\hat{t}$ (Fig. 6.5(a)) and the conditional weighted distribution defined as $\hat{v}\hat{t}\cdot P_{II,i}(\hat{v}\hat{t})$ (Fig. 6.5(b)) have been investigated in the buffer region (y^+=10.6) where the organized motions are prominent. The distribution of $\hat{v}\hat{t}\cdot P_{II,i}(\hat{v}\hat{t})$ represents a statistical contribution to the total heat flux $\overline{vt}$ from various amplitudes of $\hat{v}\hat{t}$ fluctuations. As is obvious from Fig. 6.5(a), ejections (i=2) and sweeps (i=4) are the principal contributors to the time-averaged heat flux $\overline{vt}$, since the conditional pdfs in the ejection- and sweep-phase are skewed largely to the positive side of vt. At this y-location, the fractional contributions of ejections and sweeps are nearly

equal (see Fig. 6.3). However, Fig. 6.5(b) indicates that the detailed structure is somewhat different between ejections and sweeps. Larger-amplitude fluctuations of turbulent heat flux ($\hat{v}\hat{t}>2.5$) are mainly associated with the sweep-type coherent motions. Furthermore, Fig. 6.5(a), (b) also proves that organized motions (ejections and sweeps) sometimes contribute negatively to the time-averaged value $\overline{vt}$. This means that a passive scalar field (thermal field) does not necessarily follow a velocity field in a wall turbulent shear flow. In both interaction-phases (i=1, 3), the distributions of conditional pdf are seen to be much more symmetrical, and the correspondence between turbulent heat transfer and fluid motions is very weak. Hence, the fractional contributions to $\overline{vt}$ from both interactions remain considerably low.

Lines in Fig. 6.5(a) show theoretical values calculated from the following equation (6-4), which is obtained applying the same procedure as in the derivation of the pdf for a second-order moment from the three-dimensional joint pdf.

$$P_{II,i}(\hat{v}\hat{t}) = \int_0^\infty\int P(\sigma_{u,i}\hat{u},\sigma_{v,i}\hat{v},\sigma_{v,i}x/\hat{v})(d\hat{v}/\hat{v})d\hat{u}$$

$$= \frac{1}{(2\pi)^{3/2}} \sum_{p,q,r=0}^{K\leqq 4} \sigma_{u,i}^{p}\,\sigma_{v,i}^{q+r}\,C_{pqr}\,B_{0,p}$$

$$\times \int_0^\infty H_q(\hat{v})H_r(x/\hat{v})\exp[-\{\hat{v}^2+(x/\hat{v})^2\}/2]d\hat{v}/\hat{v} \qquad (6\text{-}4)$$

The appreciable discrepancy between the theories and measurements can be attributed to a little truncation-effect in the series-expansion for the

joint pdf.

6.2.3. Weighted functions in (u, v)-plane

The conditional analysis based on threshold H alone is not sufficient to ascertain the detailed correspondence between momentum/heat transfer and fluid motions. Therefore, the authors define the following weighted function $W_x(\hat{u},\hat{v})$ in the (u, v)-plane:

$$W_x(\hat{u},\hat{v}) = \int_{-\infty}^{\infty} xP(\hat{u},\hat{v},\hat{t})d\hat{t} \qquad (6\text{-}5)$$

$$x = \hat{u}^{\ell}\hat{v}^{m}\hat{t}^{n}$$

This function provides a powerful tool to see how and how much each fluid motion in the quadrants of the (u, v)-plane produces the moment x. The integrated value of W_x in each quadrant becomes the fractional contribution $\overline{(x)}_i$. And the integration over the whole (u, v)-plane reduces to the conventional time-averaged value $\overline{x}$.

The experimental distributions of the weighted function for $x=\hat{t}^2$ are shown in Fig. 6.6. In the immediate neighborhood of the wall ($y^+=7.6$), the distribution extends far to the fourth-quadrant (sweep-phase), and peaks in the second-quadrant (ejection-phase) as if u fluctuations were limited at $\hat{u}= -2$. In the core region of the flow ($y^+=377.6$), on the other hand, the distribution becomes wider, gently sloping in the second-quadrant, and becoming narrower and steeper in the fourth-quadrant. In Section 5.7, it was shown that the contributions to temperature variance

$\overline{(t^2)_i}$ from sweeps were the largest in the vicinity of the wall, and became almost equal to those from ejections in the core region (see Fig. 5.22). However, Fig. 6.6 demonstrates the existence of a definite difference in the internal structures of temperature variance $\overline{t^2}$, which cannot be identified from the conventional fractional contribution $\overline{(t^2)_i}$. Hence, the ways of contribution from ejections and sweeps to the production of temperature variance in the near-wall region are totally different from those in the core region. Moreover, one can recognize that, even if the fractional contributions from ejections and sweeps are equal, there is a large difference in the scales of both motions governing the production of temperature fluctuations.

The experimental results of $W_{\hat{u}\hat{v}}$ and $W_{\hat{v}\hat{t}}$ in the near-wall region and of $W_{\hat{v}\hat{t}}$ in the core region are shown in Figs. 6.7(a), (b) and (c), respectively. In the contour maps of Fig. 6.7, solid and broken lines represent positive and negative values, and intervals between two successive contour lines are 0.02. With Figs. 6.7(a) and (b), we can investigate the internal structures of the production processes of $\overline{uv}$ and $\overline{vt}$ near the wall. Integration of $W_{\hat{u}\hat{v}}$ and $W_{\hat{v}\hat{t}}$ within each quadrant results in the fractional contributions of different motions with H=0 presented in Figs. 6.2 and 6.3, respectively. Also, integration of $W_{\hat{v}\hat{t}}$ over the region outside the hyperbolic boundary $\hat{v}=\pm H/\hat{u}$ results in the fractional contributions to $\overline{vt}$ from different motions as a function of H shown in Fig. 6.4. Thus, Fig. 6.7 contains a great deal of information.

As seen from these figures, the sweep-type motions with large-amplitude u fluctuations dominate the production of $\overline{uv}$ and $\overline{vt}$ in the near-wall region. The distributions have the characteristics similar to temperature

variance (Fig. 6.6; $y^+=7.6$). However, whereas both interactions (i=1, 3) make a positive contribution to the production of temperature variance $\overline{t^2}$, they contribute negatively to the Reynolds shear stress $-\overline{uv}$ and turbulent temperature flux $\overline{vt}$. Profiles shown in Figs. 6.7(a) and (b) are too similar to be readily distinguished from the other. This is an important result which shows that a close analogy exists between the internal structures of $\overline{uv}$ and $\overline{vt}$.

The distribution of $W\hat{v}\hat{t}$ in the core region (Fig. 6.7(c)) is different from that in the near-wall region (Fig. 6.7(b)) in the following respects: (i) the distributions in the second- and fourth-quadrant exhibit opposite trends; (ii) the negative regions seen in the first- and third-quadrant of Fig. 6.7(b) disappear in Fig. 6.7(c). The internal structures of $W\hat{v}\hat{t}$ change with the distance from the wall as in temperature variance, and the analogy between Reynolds shear stress and turbulent heat flux breaks down with increasing distance from the wall. Note that Reynolds shear stress -uv is consistently negative in the first- and third-quadrant.

6.3. Contribution of Organized Motions to Third-Order Moments

In Section 4.4.2, it has been shown that the pdf distributions of third-order moments (i.e., turbulent diffusion of turbulence energy, temperature variance, turbulent heat fluxes, etc.) have very long tails and the asymmetry in these pdfs is fractional, but it is this asymmetry that determines the net value of turbulent diffusion. In this section, their internal structures are elucidated.

The contributions to $\overline{vu^2}$ and $\overline{vt^2}$ from different fluid motions with H=0 are presented in Figs. 6.8(a) and (b), respectively. Obviously, the turbulent diffusion of u^2 and t^2 occurs mainly during the ejection- and sweep-phase (i=2, 4), and hence disparity of contributions between these two-types of motions determines the magnitude and direction (i.e., plus and minus) of time-averaged diffusion. Neither interaction (i=1, 3) influences the time-averaged values $\overline{vu^2}$ and $\overline{vt^2}$, since the fractional contributions from these motions are not only very small in absolute value but nearly symmetrical about zero (sum being zero). It is now established that the turbulent diffusion is determined by dynamic phenomena associated with organized motions of ejections and sweeps. This also explains why the third-order moments cannot be described adequately by a static model such as gradient-type diffusion of the second-order moment (see Section 4.4.1). The theoretical values in Fig. 6.8, calculated from Eq.(6-3), reproduce this dynamic behaviour very well. On the other hand, if a Gaussian distribution is supposed for the joint pdf in Eq.(6-3), the contributions to the third-order moments from motions in the second- and fourth-quadrant of the (u, v)-plane are completely equal in magnitude with an opposite sign. Hence, the foregoing important characteristics of third-order moments cannot be described fully.

To judge the feasibility of predicting the characteristics of the third-order moments theoretically in conjunction with the scales of fluid motions, the experimental distributions of the conditional pdf of vu^2 and vt^2 have been examined at $y^+=37.1$ where the net values of the turbulent diffusion take their maxima (see Fig. 4.9). Figure 6.9 shows the measurements, compared with the present predictions. Solid lines in this figure

represent the following theoretical distributions, which are obtained after differentiating the cumulative probability distribution functions for vu^2 and vt^2.

$$P_{\mathrm{III},i}(\hat{v}\hat{u}^2) = \int_0^\infty \{\int_{-\infty}^\infty P(\sigma_{u,i}\,\hat{u}, x/\hat{u}^2, \hat{t})d\hat{t}\}d\hat{u}/\hat{u}^2$$

$$= \frac{1}{2\pi} \sum_{p,q=0}^{p+q\leqq 4} \sigma_{u,i}^p\, C_{pq0} \int_0^\infty H_p(\hat{u})H_q(x/\hat{u}^2)\exp[-\{\hat{u}^2+(x/\hat{u}^2)^2\}/2]d\hat{u}/\hat{u}^2 \qquad (6\text{-}6)$$

here $x = \hat{v}\hat{u}^2$;

$$P_{\mathrm{III},i}(\hat{v}\hat{t}^2) = \int_0^\infty \{\int_{-\infty}^\infty P(\sigma_{u,i}\,\hat{u}, x/\hat{t}^2, \hat{t})d\hat{t}/\hat{t}^2\}d\hat{u}$$

$$= \frac{2}{(2\pi)^{3/2}} \sum_{\substack{p,q=0 \\ r=\text{even}}}^{K\leqq 4} \sigma_{u,i}^p\, C_{pqr}\, B_{0,p}$$

$$\times \int_0^\infty H_q(x/\hat{t}^2)H_r(\hat{t})\exp[-\{(x/\hat{t}^2)^2+\hat{t}^2\}/2]d\hat{t}/\hat{t}^2 \qquad (6\text{-}7)$$

where $x = \hat{v}\hat{t}^2$.

It can be seen from the measured distributions that both conditional pdfs of vu^2 and vt^2 at small $|x|$ values are a bit larger in the sweep-phase than in the ejection-phase, and vice versa at larger $|x|$ values. Since the fractional contributions $\overline{(vu^2)_i}$ and $\overline{(vt^2)_i}$ are obtained from the integration of Eqs.(6-6) and (6-7) multiplied by x, the conditional pdfs at larger $|x|$ values contribute largely to these quantities. Accordingly, now that large-amplitude fluctuations of vu^2 and vt^2 are generated mainly by ejections, the fractional contributions from ejections become larger than those from sweeps as seen in Fig. 6.8. Such phenomena are well reproduced by the theoretical conditional pdfs given by Eqs.(6-6) and (6-7).

The experimental and theoretical distributions of the weighted function (6-5) for vt^2 are shown in Figs. 6.10(a) and (b), respectively. From the experimental result, one can see that the large-amplitude ejections contribute largely to the production of $\overline{vt^2}$. Apparently, the theoretical results reproduce precisely the peak locations and the extent of the distributions in the second- and fourth-quadrant.

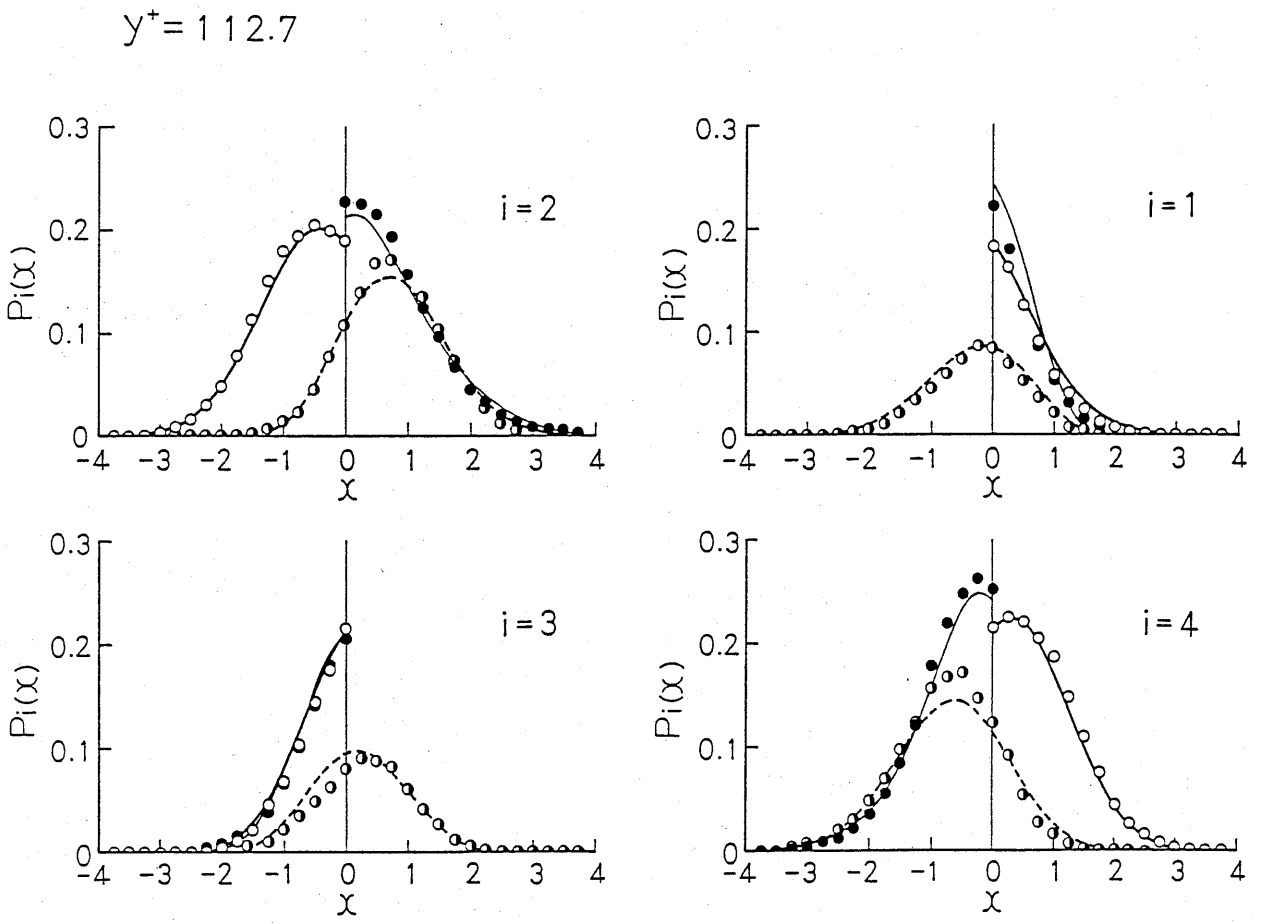

Fig. 6.1. Conditional probability density distributions of velocity and temperature fluctuations. Experiments: ○ , $P_i(\hat{u})$; ● , $P_i(\hat{v})$; ◑ , $P_i(\hat{t})$. Predictions from Eq.(6-1): ———, $P_i(\hat{u})$; ————, $P_i(\hat{v})$; — — —, $P_i(\hat{t})$.

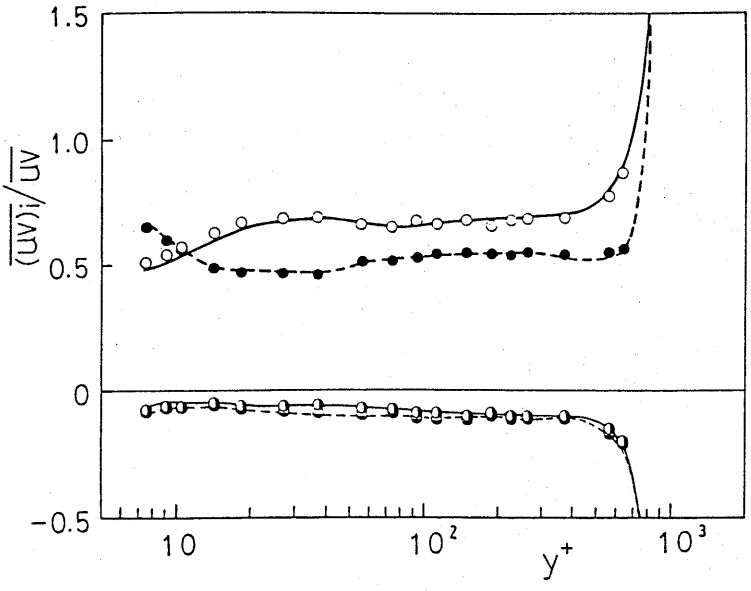

Fig. 6.2. Theoretical predictions of the fractional contributions to Reynolds shear stress $-\overline{uv}$. Experiments: ◑ , i=1; ○ , i=2; ◒ , i=3; ● , i=4. Predictions from Eq.(6-3): ——— , i=1; ——————, i=2; — — — —, i=3; — — — —, I=4.

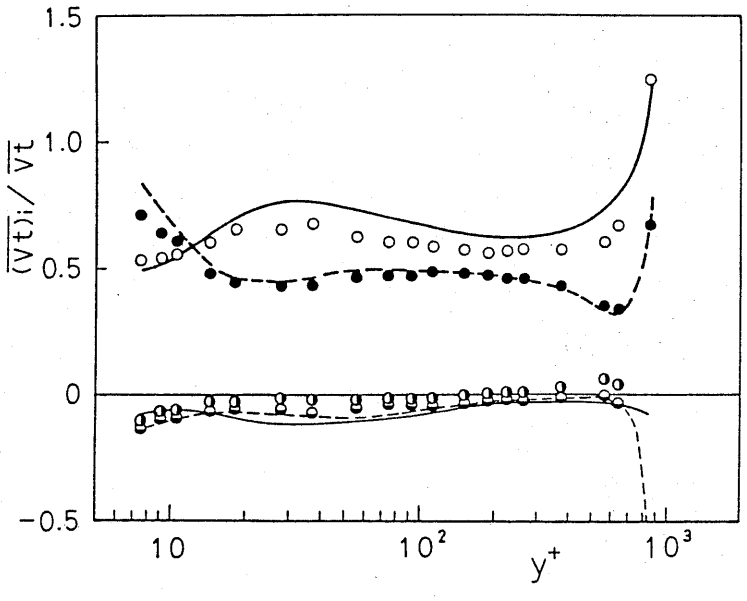

Fig. 6.3. Theoretical predictions of the fractional contributions to turbulent heat flux $\overline{vt}$. Notation as in figure 6.2.

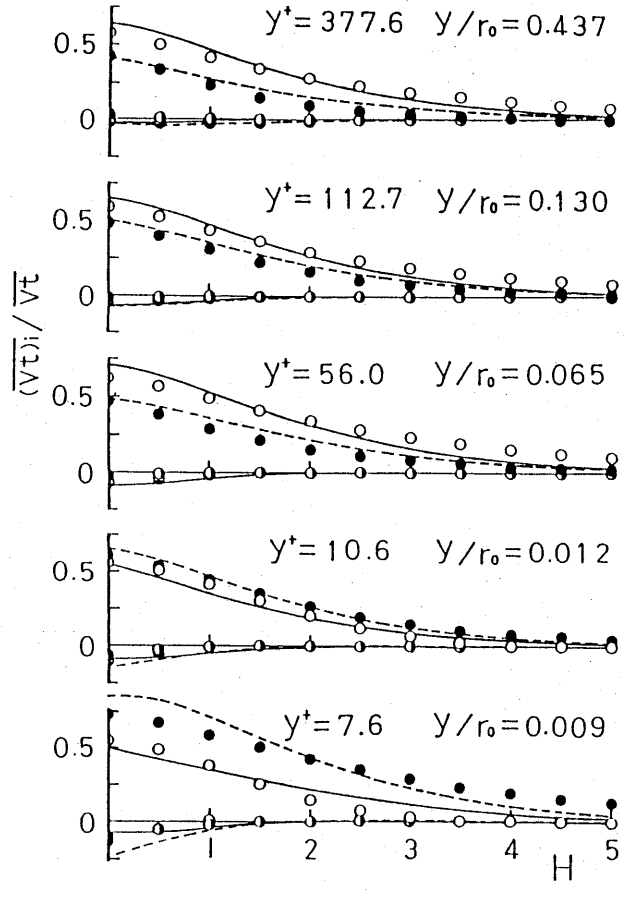

Fig. 6.4. Theoretical predictions of the fractional contributions to $\overline{vt}$ as a function of H. Notation as in figure 6.2.

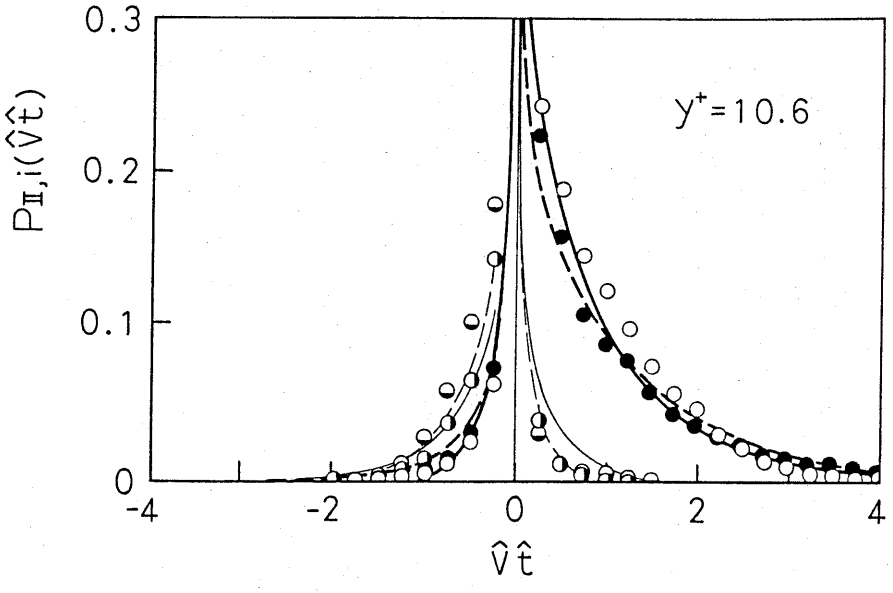

(a)

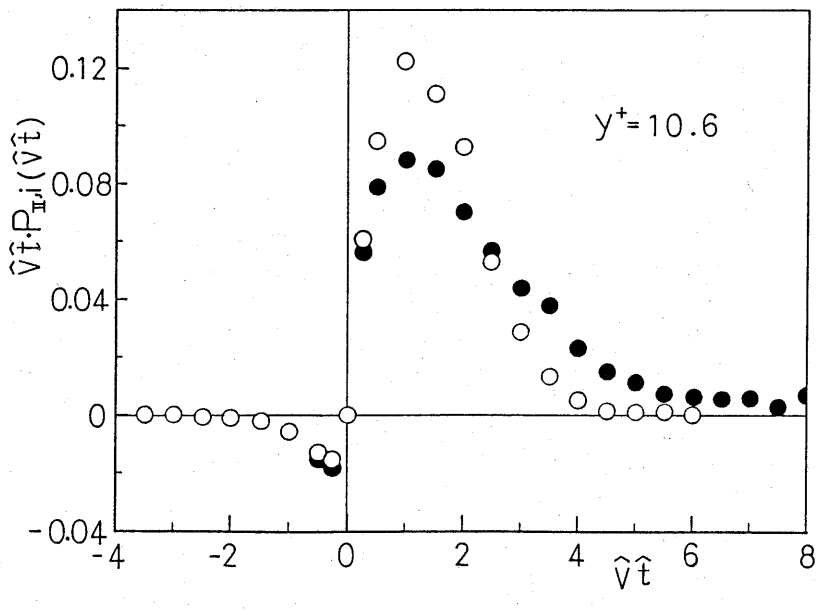

(b)

Fig. 6.5. (a) Conditional probability density distribution of heat flux $\hat{v}\hat{t}$. Experiments: ◑ , i=1; ○ , i=2; ◒ , i=3; ● , i=4. Predictions from Eq.(6-4): ——— , i=1; ——— , i=2; – – – – , i=3; — — — —, i=4. (b) Experimental distributions of $\hat{v}\hat{t}P_{II,i}(\hat{v}\hat{t})$ representing a fractional contribution to the heat flux $\overline{vt}$. ○ , i=2; ● , i=4.

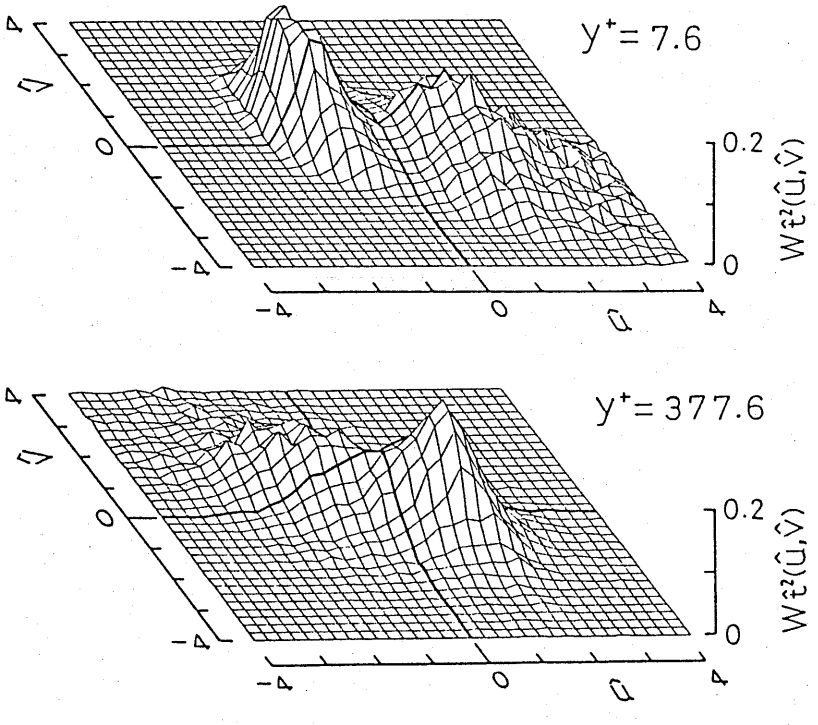

Fig. 6.6. Experimental distributions of the weighted function for temperature variance $\overline{t^2}$.

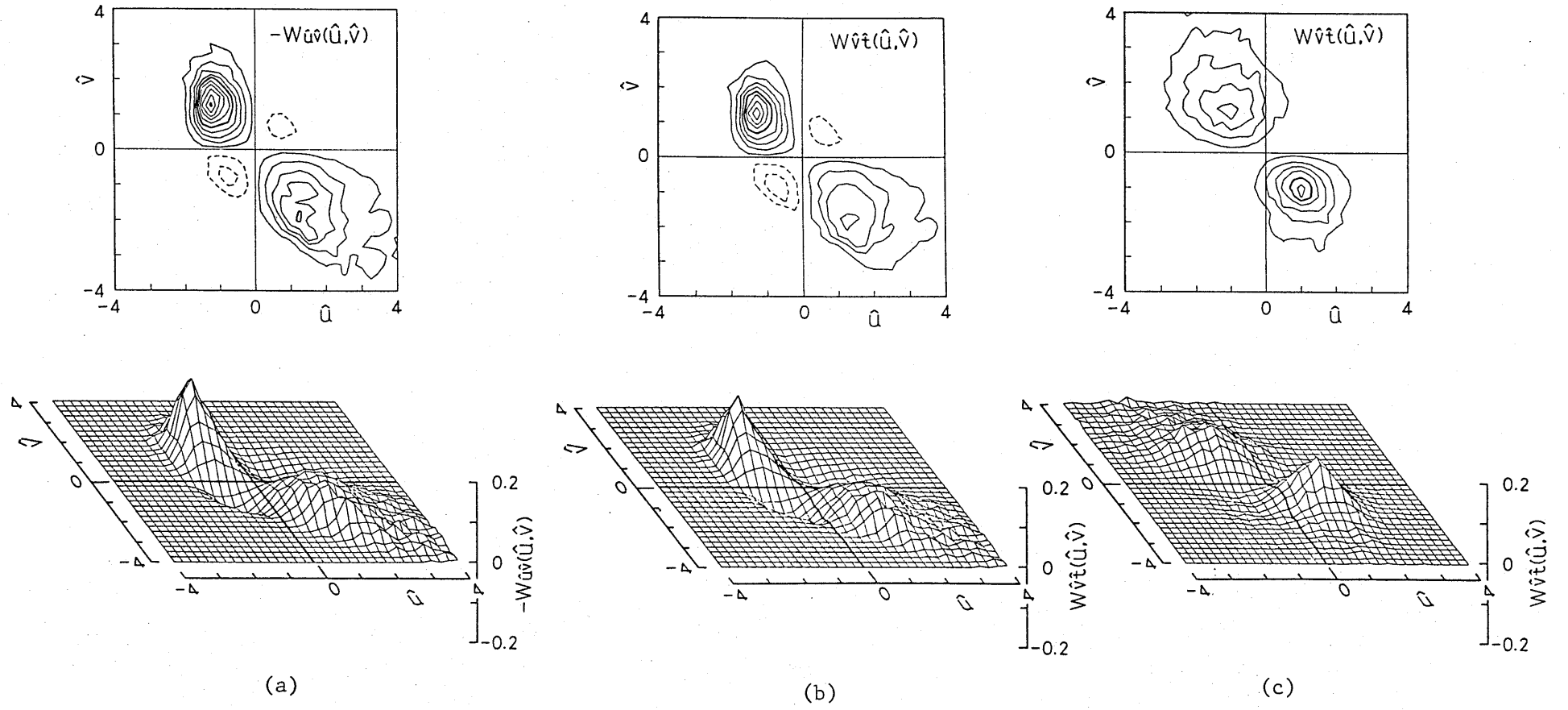

Fig. 6.7. Experimental distributions of the weighted functions for turbulent momentum and heat transfer.

(a) $W\hat{u}\hat{v}$ in the near-wall region (y^+=7.6);

(b) $W\hat{v}\hat{t}$ in the near-wall region (y^+=7.6);

(c) $W\hat{v}\hat{t}$ in the core region (y^+=377.6).

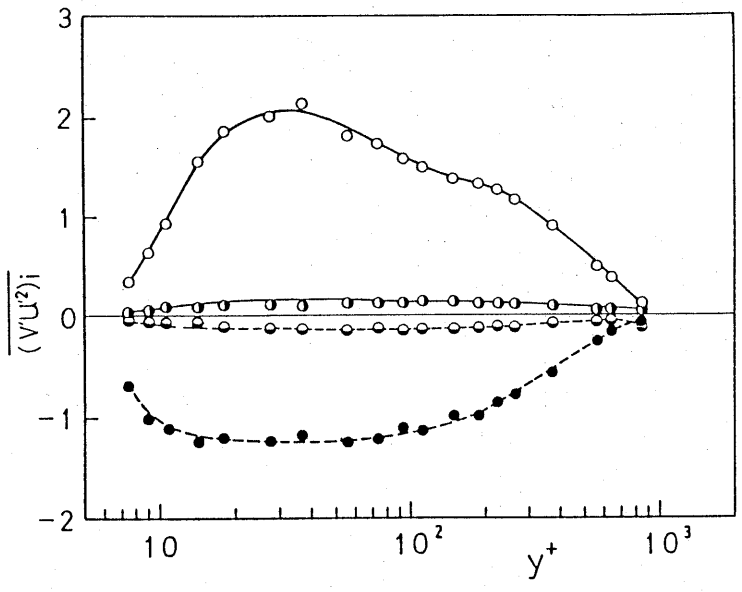

(a)

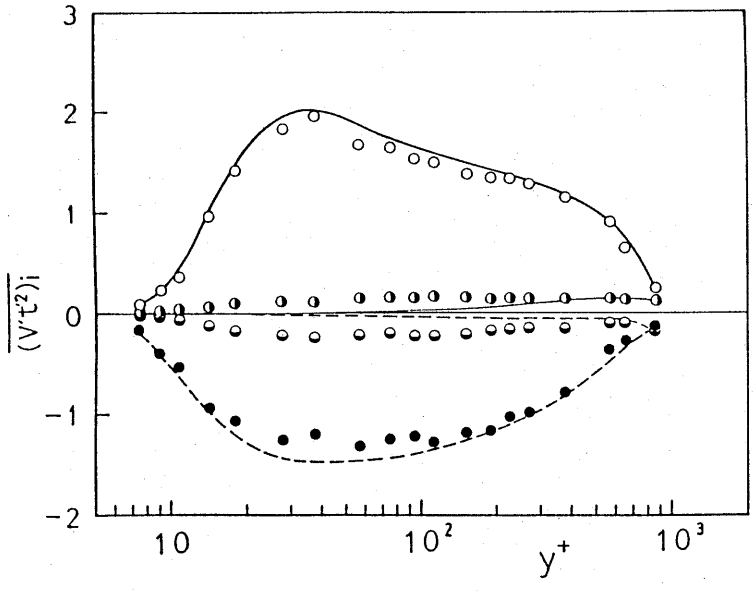

(b)

Fig. 6.8. Contributions of organized motions to third-order moments $\overline{vu^2}$ and $\overline{vt^2}$. Notation as in figure 6.2.
(a) $\overline{(vu^2)_i}$; (b) $\overline{(vt^2)_i}$.

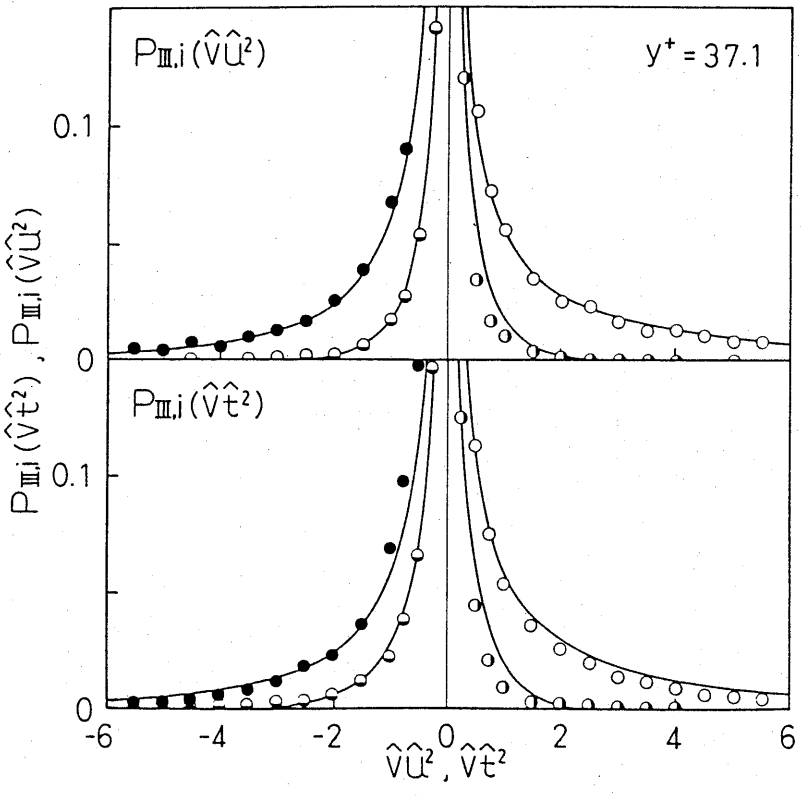

Fig. 6.9. Conditional probability density distributions of the third-order moments $\hat{v}\hat{u}^2$ and $\hat{v}\hat{t}^2$ (y^+=37.1). Experiments: ◑, i=1; ○, i=2; ◒, i=3; ●, i=4. ————, predictions from Eq.(6-6) for $\hat{v}\hat{u}^2$ and Eq.(6-7) for $\hat{v}\hat{t}^2$.

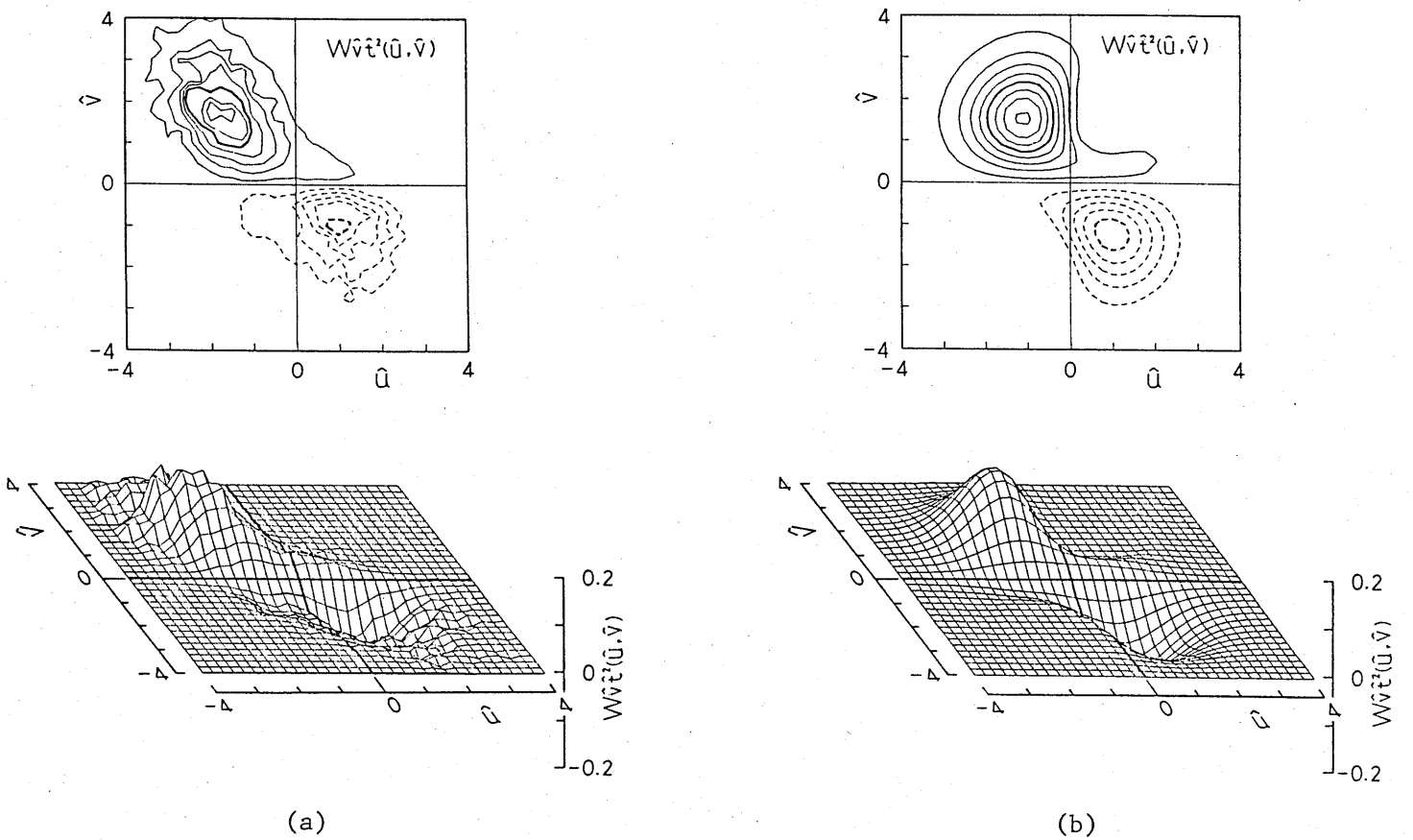

Fig. 6.10. Experimental and theoretical distributions of the weighted function for $\overline{vt^2}$ (y^+=37.1).
(a) Experiment; (b) Prediction.

CHAPTER VII

CONCLUSIONS

The statistical characteristics of momentum and heat transfer in a wall turbulent shear flow have been investigated experimentally and theoretically. And the relationship between the organized motions near the wall and turbulent heat transfer has been analyzed by introducing a new conditional sampling technique which possesses objectivity and reliability for the detection and description of coherent turbulent motions. The following is a summary of the important conclusions that can be made from the present study.

7.1. Statistical Characteristics of Wall turbulence with Heat Transfer

(1) A three-dimensional joint pdf has been developed so as to describe transfer processes of momentum and heat in a two-dimensional turbulence field.

(2) The pdf distributions of u and t fluctuations can be approximated with Gaussian ones in the log-law region, but in the other region, they are skewed to the opposite sides. The probability distribution of v fluctuations differs from a Gaussian distribution over a greater part of the flow field.

(3) The skewness factor can be represented with the time fractions (i.e.,

intermittency factor) occupied by positive and negative events of a turbulence component.

(4) The pdf distributions of Reynolds shear stress uv and turbulent heat flux vt are similar, and change little over the entire cross section except for the pipe-centerline region.

(5) The distributions of turbulent diffusion of uv, vt, t^2, etc. have been measured and compared with predictions from the existing models for triple products. All existing models are found to give quite unsatisfactory predictions for diffusion of uv and vt.

(6) A net value of turbulent diffusion is determined by the fractional asymmetry of the pdf distribution. This asymmetry cannot be reproduced by a Gaussian pdf, but can be represented with the pdf developed in the present study.

7.2. Coherent Motions and Their Role in Turbulent Heat Transfer

(1) The coherent structures in a wall turbulent shear flow are well represented in terms of four basic well-ordered motions.

(2) The inherent intermittency of turbulent heat and momentum transfer can be considered the consequence of highly intermittent coherent motions near the wall.

(3) The ejection- and sweep-type coherent motions play a very dominant role in determining the transport processes of heat and momentum. The degree of their contributions, however, depends on each basic flow-pattern.

(4) The dissipations of both velocity and temperature fluctuations occur mainly during an interactive flow period shifting from ejections to sweeps. This process has universal aspects independent of basic flow-patterns.

(5) The vortex structures of four basic flow-patterns of the coherent structures have been quantitatively established, which correspond very well with the results obtained by various flow-visualization studies.

(6) The transport processes of heat are closely related to the vortex structures of coherent motions. Pattern 4, in particular, is very important, because it induces a great deal of turbulent heat transfer.

7.3. Fine Structures of Coherent Turbulent Heat Transfer

(1) The theoretical formulations for the conditional pdf and the fractional contributions to various moments are derived using the three-dimensional joint pdf. These equations are applicable to the structural analysis of velocity and temperature fluctuations and their high-order moments.

(2) Temperature fluctuations are influenced strongly by the organized motions of ejections and sweeps, but hardly correlate to interaction-type motions.

(3) In the near-wall region $y^+<10$, the sweeps play a dominant role in the production processes of Reynolds shear stress $\overline{uv}$ and turbulent heat flux $\overline{vt}$; the ejections predominate in the remaining region.

(4) In the near-wall region, there is a close analogy between the instantaneous structures of Reynolds shear stress uv and turbulent heat flux vt.

(5) The net values of turbulent diffusion in turbulence energy, temperature variance, turbulent heat fluxes, etc., are determined by an imbalance between the contributions from ejections and sweeps. This fact can be well predicted by the present theory.

REFERENCES

Alfredsson, P. H. & Johansson, A. V. 1984 On the detection of turbulence-generating events. *J. Fluid Mech.* **139**, 325-345.

Antonia, R. A. & Atkinson, J. D. 1973 High-order moments of Reynolds shear stress fluctuations in a turbulent boundary layer. *J. Fluid Mech.* **58**, 581-593.

Antonia, R. A., Rajagopalan, S., Subramanian, C. S. & Chambers, A. J. 1982 Reynolds-number dependence of the structure of a turbulent boundary layer. *J. Fluid Mech.* **121**, 123-140.

Bakewell, H. P. Jr. & Lumley, J. L. 1967 Viscous sublayer and adjacent wall region in turbulent pipe flow. *Phys. Fluids* **10**, 1880-1889.

Blackwelder, R. F. 1977 On the role of phase information in conditional sampling. *Phys. Fluids* **20**, s232-242.

Blackwelder, R. F. & Eckelmann, H. 1979 Streamwise vortices associated with the bursting phenomenon. *J. Fluid Mech.* **94**. 577-594.

Blackwelder, R. F. & Kaplan, R. E. 1976 On the wall structure of the turbulent boundary layer. *J. Fluid Mech.* **76**, 89-112.

Bogard, D. G. & Tiederman, W. G. 1986 Burst detection with single-point velocity measurements. *J. Fluid Mech.* **162**, 389-413.

Bradshaw, P., Cebeci, T. & Whitelaw, J. H. 1981 *Engineering calculation methods for turbulent flow.* Academic Press, New York.

Bremhorst, K. & Bullock, K. J. 1973 Spectral measurements of turbulent heat and momentum transfer in fully developed pipe flow. *Int. J. Heat Mass Transfer* **16**, 2141-2154.

Brodkey, R. S., Wallace, J. M. & Eckelmann, H. 1974 Some properties of truncated turbulence signals in bounded shear flows. *J. Fluid Mech.* **63**, 209-224.

Chen, C. H.-P. & Blackwelder, R. F. 1978 Large-scale motion in a turbulent boundary layer: A study using temperature contamination. *J. Fluid Mech.* **89**, 1-31.

Corino, E. R. & Brodkey, R. S. 1969 A visual investigation of the wall region in turbulent flow. *J. Fluid Mech.* **37**, 1-30.

Cormack, D. E., Leal, L. G. & Seinfeld, J. H. 1978 An evaluation of mean Reynolds stress turbulence models: The triple velocity correlation. *Trans. ASME: J. Fluids Engineering* **100**, 47-54.

Daly, B. J. & Harlow, F. H. 1970 Transport equations in turbulence. *Phys. Fluids* **13**, 2634-2649.

Deardorff, J. W. 1973 Three-dimensional numerical modeling of the planetary boundary layer. *Proc. Workshop on Micrometeorology*, Am. Meteorol. Soc., 271-311.

Durst, F., Jovanovic, J. & Kanevce, Lj. 1987 Probability density distribution in turbulent wall boundary-layer flows. *Turbulent Shear Flows* 5 (eds. L. J. S. Bradbury, F. Durst, B. E. Launder, F. W. Schmidt, J. H. Whitelaw), 197-220, Springer-Verlag, Berlin.

Elghobashi, S. E. & Launder, B. E. 1981 Modelling the dissipation rate of temperature variance in a thermal mixing layer, *Proc. 3rd Int. Symp. on Turbulent Shear Flows*, 15.13-15.17, University of California Davis.

Falco, R. E. 1982 A synthesis and model of turbulence structure in the wall region. *Structure of Turbulence in Heat and Mass Transfer* (edited by Zarić, Z. P.), 43-57, Hemisphere, New York.

Frenkiel, F. N. & Klebanoff, P. S. 1967 Higher-order correlations in a turbulent field. *Phys. Fluids* **10**, 507-520.

Fujita, H. & Kovasznay, L. S. G. 1968 Measurement of Reynolds stress by a single rotated hot wire anemometer. *Review of Scientific Instruments* **39**, 1351-1355.

Grass, A. J. 1971 Structural features of turbulent flow over smooth and rough boundaries. *J. Fluid Mech.* **50**, 233-255.

Hanjalić, K. & Launder, B. E. 1972 A Reynolds stress model of turbulence and its application to thin shear flows. *J. Fluid Mech.* **52**, 609-638.

Head, M. R. & Bandyopadhyay, P. 1981 New aspects of turbulent boundary-layer structure. *J. Fluid Mech.* **107**, 297-338.

Hishida, M. & Nagano, Y. 1978a Simultaneous measurements of velocity and temperature in nonisothermal flows. *Trans. ASME: J. Heat Transfer* **100**, 340-345.

Hishida, M. & Nagano, Y. 1978b Structure of turbulent temperature and velocity fluctuations in the thermal entrance region of a pipe. *Proc. 6th Int. Heat Transfer Conf.* 2, 531-536, Toronto, Hemisphere, Washington D.C..

Hishida, M. & Nagano, Y. 1979 Structure of turbulent velocity and temperature fluctuations in fully developed pipe flow. *Trans. ASME: J. Heat Transfer* **101**, 15-22.

Hishida, M. & Nagano, Y. 1981 Structure of pipe flow turbulence. Part 2. Coherent structures near the wall. *Trans. Japan Soc. Mech. Engrs: Ser. B* **47**, 50-58.

Hishida, M. & Nagano, Y. 1987 Structures of turbulent heat transfer. *Heat Transfer in High Technology and Power Engineering* (eds. W.-J. Yang & Y. Mori), 488-499, Hemisphere, New York.

Hishida, M. & Nagano, Y. 1988a Turbulence measurements with symmetrically bent V-shaped hot-wires. Part 1. Principles of operation. *Trans. ASME: J. Fluids Engineering* **100**.

Hishida, M. & Nagano, Y. 1988b Turbulence measurements with symmetrically bent V-shaped hot-wires. Part 2. Measuring velocity components and turbulent shear stresses. *Trans. ASME: J. Fluids Engineering* **100**.

Hishida, M., Nagano, Y. & Tagawa, M. 1986 Transport processes of heat and momentum in the wall region of turbulent pipe flow. *Proc. 8th Int. Heat Transfer Conf.* 3, 925-930, San Francisco, Hemisphere, Washington D.C..

Hishida, M., Nagano, Y., Tagawa, M. & Miyakawa, H. 1984 Turbulent heat transfer associated with coherent structures in fully developed pipe flow. *Trans. Japan Soc. Mech. Engrs: Ser. B* **50**, 537-542.

Iritani, Y., Kasagi, N. & Hirata, M. 1985 Heat transfer mechanism and associated turbulence structure in the near-wall region of a turbulent boundary layer. *Turbulent Shear Flows* **4** (eds. L. J. S. Bradbury, F. Durst, B. E. Launder, F. W. Schmidt, J. H. Whitelaw), 223-234. Springer-Verlag, Berlin.

Johansson, A. V. & Alfredsson, P. H. 1982 On the structure of turbulent channel flow. *J. Fluid Mech.* **122**, 295-314.

Kampé de Fériet, J. 1966 *David Taylor Model Basin Report* 2013, Naval Ship Research and Development Center, Washington D.C..

Kim, H. T., Kline, S. J. & Reynolds, W. C. 1971 The production of turbulence near a smooth wall in a turbulent boundary layer. *J. Fluid Mech.* **50**, 133-160.

Kim, J. 1985 Turbulence structures associated with the bursting event. *Phys. Fluids* **28**, 52-58.

Kim, J. & Moin, P. 1986 The structure of the vorticity field in turbulent channel flow. Part 2. Study of ensemble-averaged fields. *J. Fluid Mech.* **162**, 339-363.

Kline, S. J., Reynolds, W. C., Schraub, F. A. & Runstadler, P. W. 1967 The structure of turbulent boundary layers. *J. Fluid Mech.* **30**, 741-773.

Kreplin, H.-P. & Eckelmann, H. 1979 Behavior of the three fluctuating velocity components in the wall region of a turbulent channel flow. *Phys. Fluids* **22**, 1233-1239.

Laufer, J. 1954 The structure of turbulence in fully developed pipe flow. *NACA Report* **1174**.

Launder, B. E. 1985 Progress and prospects in phenomenological turbulence models. *Theoretical Approaches to Turbulence* (ed. D. L. Dwoyer, M. Y. Hussaini & R. G. Voigt), 155-186, Springer-Verlag.

Lee, M. K., Eckelman, L. D. & Hanratty, T. J. 1974 Identification of turbulent wall eddies through the phase relation of the components of the fluctuating velocity gradient. *J. Fluid Mech.* **66**, 17-33.

Lu, S. S. & Willmarth, W. W. 1973 Measurements of the structure of the Reynolds stress in a turbulent boundary layer. *J. Fluid Mech.* **60**, 481-511.

Luchik, T. S. & Tiederman, W. G. 1987 Timescale and structure of ejections and bursts in turbulent channel flows. *J. Fluid Mech.* **174**, 529-552.

Lumley, J. L. 1978 Computational modeling of turbulent flows. *Advances in Applied Mechanics* **18**, ed. Yih, C.-S., 123-176, Academic Press.

Monin, A. S. & Yaglom, A. M. 1971 *Statistical fluid mechanics* **1**, MIT Press, Cambridge.

Nagano, Y. & Hishida, M. 1985 Production and dissipation of turbulent velocity and temperature fluctuations in fully developed pipe flow. *Proc. 5th Int. Symp. on Turbulent Shear Flows*, 14.19-14.24, Cornell University.

Nagano, Y., Hishida, M. & Tagawa, M. 1987 Coherent motions and their role in the turbulent transport process of heat. *Trans. Japan Soc. Mech. Engrs: Ser. B* **53**, 2167-2174.

Nagano, Y. & Tagawa, M. 1987a Statistical characteristics of transfer processes in a wall turbulent shear flow. *Proc. 2nd Int. Symp. on Transport Phenomena in Turbulent Flows*, 481-494, Tokyo.

Nagano, Y. & Tagawa, M. 1987b Coherent motions and their role in heat transport processes in a wall turbulent shear flow. *J. Fluid Mech.*, submitted.

Nagano, Y. & Tagawa, M. 1988 Statistical characteristics of wall turbulence with passive scalar. *J. Fluid Mech.*, to be published.

Nagano, Y., Tagawa, M. & Tokoro, A. 1988 Statistical characteristics of heat and momentum transfer in a wall turbulent shear flow (1st report, High-order moments and probability distributions of velocity and temperature fluctuations). *Trans. Japan Soc. Mech. Engrs: Ser. B* **54**, to be published.

Nakagawa, H. & Nezu, I. 1977 Prediction of the contributions to the Reynolds stress from bursting events in open-channel flows. *J. Fluid Mech.* **80**, 99-128.

Nakagawa, H. & Nezu, I. 1981 Structure of space-time correlations of bursting phenomena in an open-channel flow. *J. Fluid Mech.* **104**, 1-43.

Nychas, S. G., Hershey, H. C. & Brodkey, R. S. 1973 A visual study of turbulent shear flow. *J. Fluid Mech.* **61**, 513-540.

Offen, G. R. & Kline, S. J. 1974 Combined dye-streak and hydrogen-bubble visual observations of a turbulent boundary layer. *J. Fluid Mech.* **62**, 223-239.

Offen, G. R. & Kline, S. J. 1975 A proposed model of the bursting process in turbulent boundary layers. *J. Fluid Mech.* **70**, 209-228.

Owen, R. G. 1973 An Analytical Turbulent transport model applied to non-isothermal fully-developed duct flows. *Ph.D. Thesis*, Pennsylvania State University.

Paranthoen, P., Petit, C. & Lecordier, J. C. 1982 The effect of the thermal prong-wire interaction on the response of a cold wire in gaseous flows (Air, Argon and Helium). *J. Fluid Mech.* **124**, 457-473.

Perry, A. E. & Hoffmann, P. H. 1976 An experimental study of turbulent convective heat transfer from a flat plate. *J. Fluid Mech.* **77**, 355-368.

Praturi, A. K. & Brodkey, R. S. 1978 A stereoscopic visual study of coherent structures in turbulent shear flow. *J. Fluid Mech.* **89**, 251-272.

Rao, K. N., Narasimha, R. & Narayanan, M. A. B. 1971 The 'bursting' phenomenon in a turbulent boundary layer. *J. Fluid Mech.* **48**, 339-352.

Sabot, J. & Comte-Bellot, G. 1976 Intermittency of coherent structures in the core region of fully developed turbulent pipe flow. *J. Fluid Mech.* **74**, 767-796.

Strickland, J. H. & Simpson, R. L. 1975 "Bursting" frequencies obtained from wall shear stress fluctuations in a turbulent boundary layer. *Phys. Fluids* **18**, 306-308.

Subramanian, C. S. & Antonia, R. A. 1981 Effect of Reynolds number on a slightly heated turbulent boundary layer. *Int. J. Heat Mass Transfer* **24**, 1833-1846.

Subramanian, C. S., Rajagopalan, S., Antonia, R. A. & Chambers, A. J. 1982 Comparison of conditional sampling and averaging techniques in a turbulent boundary layer. *J. Fluid Mech.* **123**, 335-362.

Tagawa, M. & Nagano, Y. 1988 Statistical characteristics of heat and momentum transfer in wall turbulent shear flow (2nd report, Fine structures of coherent turbulent transport process). *Trans. Japan Soc. Mech. Engrs: Ser. B* **54**, to be published.

Ueda, H. & Hinze, J. O. 1975 Fine-structure turbulence in the wall region of

a turbulent boundary layer. *J. Fluid Mech.* **67**, 125-143.

Verriopoulos, C. A. 1983 Effects of convex surface curvature on heat transfer in turbulent flow. *Ph.D. Thesis*, Imperial College.

Wallace, J. M., Brodkey, R. S. & Eckelmann, H. 1977 Pattern-recognized structures in bounded turbulent shear flows. *J. Fluid Mech.* **83**, 673-693.

Wallace, J. M., Eckelmann, H. & Brodkey, R. S. 1972 The wall region in turbulent shear flow. *J. Fluid Mech.* **54**, 39-48.

Willmarth, W. W. & Lu, S. S. 1972 Structure of the Reynolds stress near the wall. *J. Fluid Mech.* **55**, 65-92.

Wyngaard, J. C. 1975 Modeling the planetary boundary layer: Extension to the stable case. *Boundary-Layer Meteorology* **9**, 441-460.

Wyngaard, J. C. & Cotė, O. R. 1974 The evolution of a convective planetary boundary layer: A higher-order-closure model study. *Boundary-Layer Meteorology* **7**, 289-308.

Zarič, Z. 1979 Statistical evidence on the phenomena in wall layers of turbulent flows. *Turbulent Forced Convection in Channels and Bundles* **1**, ed. Kakaç, S. & Spalding, D. B., 377-401, Hemisphere, Washington, D.C..